Kyoto University

Structural optimization of actuators and mechanisms considering electrostatic-structural coupling effects and geometric nonlinearity

by
Takayo Kotani

A dissertation submitted in partial fulfillment
of the requirements for the degree of Doctor of Engineering

in the
Graduate School of Engineering
Department of Mechanical Engineering and Science

2014

京都大学　博士学位論文

静電-構造連成効果および幾何学的非線形性を考慮したアクチュエータと機構の構造最適化

小谷　高代

工学研究科機械理工学専攻

2014 年

Abstract

This thesis proposes structural optimization methods considering electrostatic and structural coupling effects and geometric nonlinearity aiming at designing high performance actuators and mechanisms. Based on the proposed methods, the design optimization methods for electrostatic actuators, mechanical resonators, and compliant mechanisms are constructed.

First, a level set-based structural optimization for electrostatic actuators is presented. Designing electrostatic actuators requires consideration for the electrostatic-structural coupling effects. A rigorous evaluation of electrostatic force is particularly important since electrostatic forces, surface forces, occur on the structural boundaries that change during optimizations. In this thesis, a mesh adaptation scheme for electrostatic actuator design problems is built so that the finite element mesh nodes closest to the structural boundaries snap to the structural boundaries to enable the accurate calculation of electrostatic forces. Several numerical examples are provided to demonstrate the effectiveness of the proposed method. The method is also applied to the driving-force-profile defining problem. In this problem, a multi-objective functional is formulated in order to obtain an optimal configuration that achieves prescribed driving forces at multiple electrode positions.

Next, a level set-based topology optimization for mechanical resonators is presented. Conventional topology optimizations, such as homogenization methods and density methods, encounters grayscales, which have intermediate material properties between solid and void, in the design optimization problems of flexible structures. The proposed level set-based topology optimization can avoid such problem and provides clear structural boundaries. Kinetic energy is used as the objective functional and is maximized to achieve the desired performance and obtain structural flexibility. A desired stiffness is assigned by the placement of a spring. Three-dimensional numerical examples are provided and the effectiveness of the proposed method is verified.

Last, a level set-based topology optimization for compliant mechanisms is presented. Compliant mechanisms are structures that utilize their flexibility to achieve designed functions and they undergo large deformations in certain areas because functions similar to those of joints and springs in rigid-link structures are enabled by deformations alone. Here, a Moving Particle Semi-Implicit (MPS) Method, a particle method, is used to consider geometric nonlinearity. Numerical examples are presented to demonstrate the effectiveness of the proposed method.

Acknowledgements

First, I would like to sincerely thank my supervisiors, Professor Shinji Nishiwaki, Professor Kazuhiro Izui, and Professor Takayuki Yamada, for their guidance and tremendous support during my doctoral work. I am deeply grateful for their provision of resources and a stimulating environment for this research.

I also would like to express my gratitude to Professor Atsushi Matsubara in the Department of Micro Engineering at Kyoto University, and to Professor Osamu Tabata, in the same department at Kyoto University, for their invaluable advice.

I would like to thank Yushin Precision Equipment Co., Ltd. for their support that enabled me to carry out new research in an academic field, and for their patience during the period required to complete my doctoral work.

My research would have been impossible without the kind coaching and advice I received from Professor Shintaro Yamasaki, at the Department of Mechanical Engineering at Osaka University. I am also grateful for the assistance I received from Mr. Ohkado at Toyota Central R&D Labs., Inc. In addition, Mr. Manabe, a colleague of mine during his graduate studies at Kyoto University, provided crucial help and advice concerning the use of a particle method for the geometrically nonlinear analysis in my research.

I would also like to thank my colleagues in the Manufacturing Systems Engineering Laboratory at Kyoto University for their support and encouragement during my studies. I also appreciate the work done by Mr. John E. Goodman, who edited my papers in English over the years.

Finally, I am most grateful to my father for providing me the opportunity and environment to study mechanical engineering, and to my mother for her support and encouragement during my doctoral studies. I am also thankful to my sister Miki, who encouraged me and shared both the delight of progress and the frustration of difficulties encountered during my years of study. I would also like to thank my aunt

Mari for her great support. Last, but not least, I would like to express my special gratitude to my husband, Kota, and our baby daughter, Akiyo, for their cooperation and good cheer during my doctoral studies.

Kyoto, 2014

Takayo Kotani

To my father, Susumu, and mother, Mayumi

To my sister, Miki

To my husband, Kota and daughter, Akiyo

Contents

Chapter 1

Introduction

1.1 Motivation

During the past several decades, structural optimizations have been widely used in a number of design problems, such as stiffness maximization problems [1, 2], eigenfrequency problems [3], thermal problems [4–6], fluid problems [7–9], and so on. Structural optimization methods are the methods that provide optimum design candidates for given problems based on mathematical and physical grounds and can achieve desired performances of the devices at higher levels than those of the devices designed by trial and error methods, and therefore are expected to be used in design problems at a wider range of real-world design problems. There are, however, design problems in which structural optimizations yet have numerical problems in their optimization processes. Design problems of electrostatic actuators are one of the important design problems that require further development of optimization methods. Electrostatic actuator design problems requires considerations of electrostatic-structural coupling effects and rigorous evaluation of electrostatic forces, surface forces, that occur on the structural boundaries that move during the optimization. Electrostatic actuators are essential and indispensable devices in a wide range of applications and there is a need for the development of structural optimization methods that can con-

sider electrostatic-structural coupling effects. Another design problem that has long been expected to have usable structural optimization method is the design problem of mechanisms that utilize its own flexibility. Mechanical resonators and compliant mechanisms are the good examples. Conventional topology optimization methods, such as homogenization methods and density methods, encounter a numerical problem called grayscales, which have fictitious intermediate material properties between solid and void, when expressing flexible structures. A new structural optimization method for flexible structures need to be able to provide clear structural boundaries so that engineers can understand the structural designs. Furthermore, it requires nonlinear analysis of deformations since flexible structures often undergo large deformations. My motivation is to develop structural optimizations that consider electrostatic-structural coupling effects and nonlinear analysis of deformations to design high-performance actuators and mechanisms. In this thesis, the structural optimizations that consider electrostatic-structural coupling effects and geometric nonlinearity to enable the design optimization of electrostatic actuators and mechanisms that utilize their own flexibility are developed, and based on the proposed optimization methods, the design optimization methods of electrostatic actuators, mechanical resonators, and compliant mechanisms are constructed.

1.2 Background

A number of researches have been taken place to deal with the electrostatic-structure coupling effects and structural flexibilities. Prior research pertaining to the structural optimization considering electrostatic-structural coupling effects and structural flexibilities and the main features of electrostatic actuators, mechanical resonators, and compliant mechanisms are discussed below.

Electrostatic actuators are a major class of micro-electro-mechanical devices and utilize electrostatic forces as driving forces. The principle of their operation has been

known for centuries but widespread use of such devices is a recent phenomenon because the voltage requirements are unrealistically high for relatively large devices. At the Micro-electro-mechanical systems (MEMS) scale, however, the voltage requirements are reasonably small and the simplicity of electrostatic actuator structures allows them to be manufactured using well-established microfabrication technologies developed in semiconductor industries.

There are different types of electrostatic actuators, including comb-drive [10–13], cantilever [14, 15], and parallel plate [16, 17], used in many different micro-devices such as switches, sensors, and electronic filters. The shapes of the constituent parts of electrostatic actuators are simple and are typically obtained by trial and error design methods, but the results do not necessarily provide high performances.

Several previous studies have explored the use of structural optimization methods for electrostatic actuator design problems. Shape optimization of comb-drive electrostatic actuators was carried out by Ye et al [11, 12], in which a polynomial function-based shape optimization was used and optimal structures that successfully minimized the objective functionals were obtained. However, in their research, shapes deformations during the optimization could only occur within the range defined by the polynomial function, so significant changes in shape were impossible.

Topology optimization [1], on the other hand, allows large structural changes during the optimization process. Topology optimization of electrostatic actuators has been studied by Raulli et al. [18], Alwan et al. [19, 20], and Yoon et al. [21], who collectively dealt with cantilever and inverter electrostatic actuator types. In their methods, which adopted the density method [22–24], high-performance structures were obtained by incorporating a rigorous analysis of the strong coupling between the electrostatic and elastic deformation fields. However, because the material interpolation in the above optimizations used the density method, numerical problems were encountered, such as non-clear boundaries, grayscales. Prior research [25–29] has attempted to eliminate grayscales and obtain optimal structures that are useful in an

engineering sense, but no study has yet solved all of these problems at a fundamental level.

One approach to solve these problems is the use of level set-based structural optimization methods [30–32], proposed as a structural optimization method that allows large structural changes and provides optimal configurations that are free from grayscales. Level set methods express structural boundaries using an iso-surface of the level set function. During the optimization procedure, changes in the structural boundaries are expressed by changes in the iso-surface of the level set function. This method fundamentally disallows grayscales. Wang et al. [31] and Allaire et al. [32] independently proposed structural optimization methods in which the Hamilton-Jacobi equation is used for updating the level set function, to move the structural boundaries. Yamada et al. [33,34] proposed a different type of method in which a reaction-diffusion equation is used for updating the level set function, a scheme that can allow topological changes in the target structures. These methods have been applied to many different problems, such as stiffness maximization problems [31,32] and thermal conduction maximization problems [35, 36]. A level set-based topology optimization method may be especially useful for solving electrostatic actuator optimization design problems because its clear boundary expressions are crucial to obtaining accurate driving forces, i.e., the electrostatic forces that occur on the structural boundaries.

To accurately calculate driving forces in level set-based optimization methods, a new approach is required because the structural boundaries, on which the driving forces occur, move during the calculation and therefore seldom precisely match the positions of the finite element mesh (FEM) nodes. This mismatch prevents accurate calculation of the electrostatic forces on the boundaries.

Several methods have been proposed to make the positions of the finite element mesh nodes congruent with the moving structural boundaries. One of the most popular methods is the Arbitrary Lagrangian Eulerian (ALE) method [37, 38] that is frequently used in fluid dynamics. The ALE method precisely describes the mov-

ing boundaries and interfaces using an arbitrary movement of a reference frame. The computation, however, is not very robust with this method when the boundary movement is complex. Another important method that tracks changing boundaries is the Extended Finite Element Method (X-FEM) [39–41], widely used for tracking cracks in structures. The X-FEM does not require that new or moving internal boundaries be meshed, but an additional function, called the enrichment function, is required to model new or moving internal boundaries during calculation. The X-FEM, however, is developed for tracking cracks and is out of our scope of tracking gradually-moving structural boundaries during optimization.

To track the movement of structural boundaries, Yamasaki et al. [42] proposed a scheme in which the finite element mesh nodes close to the structural boundaries are moved to positions precisely on the structural boundaries. This method does not require any additional functions, and can accurately track structural boundaries that undergo large changes. A level set-based optimization method incorporating this mesh adaptation scheme may be a practically usable optimization method for electrostatic actuators and will be discussed in detail in Chapter 2 and 3.

When designing large-scale mechanical structures, resonance phenomena must usually be suppressed, since they may cause instability. Popular design techniques for avoiding resonance phenomena are eigenfrequency maximization [3, 43] and dynamic mean compliance minimization [44, 45]. On the other hand, proactive utilization of structural instabilities in small-size devices can create useful dynamic functions. Mechanical resonators are one popular type of device that has flexible structure and whose performance is based on utilization of structural instability. Mechanical resonators can be used as sensors to measure physical quantities such as acceleration [46] or yaw angle [47] by vibrating the structures at certain frequencies. In particular, mechanical resonators are of vital importance now, for example in optical instruments such as digital cameras, where they act as sensors in systems that reduce image blurring due to undesirable physical movement.

When optimizing resonators, the periodic loading that provides vibration at certain frequencies needs to be considered. There is significant literature concerning the optimization of mechanical structures under vibration. Ma et al. [44] and Min et al. [45] explored frequency response problems for vibrating structures. Their topology optimization methods employed the homogenization method and minimized the mean dynamic compliance to increase the stiffness of elastic structures. Jog [48] also proposed a topology optimization method for mechanical structures to minimize vibration under periodic loading, using the Solid Isotropic Material with Penalization (SIMP) method. The above research aimed at stabilizing the vibration of target structures.

Nishiwaki et al. [49] and Tcherniak [50], on the other hand, developed topology optimization methods for flexible mechanical structures under periodic loading. The optimal configurations in this research amplified displacements, and resonators that provided higher performance than conventional structures were obtained. Maeda et al. [51] succeeded in developing an optimization method for the design of structures that have desired eigenfrequencies and eigenmodes. However, the optimal designs in all of the above research included grayscale areas because the homogenization method [49,51] or the SIMP method [50] was used in the optimization. These methods typically encounter grayscale problems when dealing with flexible structures because the optimization represents flexible structures using intermediate material densities that have lower stiffness than that of the solid material.

Level set-based topology optimization methods [31, 32] can overcome the above grayscale issue in problems that deal with flexible structures. Using a level set-based structural optimization method, Shu et al. [52] proposed a design method for reducing the vibration of mechanical structures subjected to periodic loading by minimizing the frequency response at certain areas of the structure at a given excitation frequency. Since their method uses the Hamilton-Jacobi equation for updating the level set function, it is a shape optimization method that allows the disappearance and integration

of holes, and the cleaving of a material domain, but does not allow the creation of holes. On the other hand, Yamada et al. [53] proposed a level set-based topology optimization method for mechanical structures under periodic loading that allows topological changes in addition to shape changes, by using the topological derivative to update the level set function. Displacement was minimized at a certain output point in this method. Both of these level set-based structural optimization methods were successful in reducing the frequency response of structures, and provided structural configurations with clear boundaries that were valid from a manufacturing point of view. However, no research has been presented so far in the level set-based structural optimization research field where the aim is to amplify the displacements of mechanical structures. For the optimal design of resonators, an optimization method for mechanical structures that aims to amplify displacements and can provide clear structural boundaries must be developed and will be discussed in detail in Chapter 4.

A number of devices including mechanical resonators and compliant mechanisms undergo large deformations during operation. To analyze deformations that include large deformations [54–60], nonlinear analysis is preferable. In nonlinear optimization problems, however, the tangent stiffness matrices may not always be positive in low density elements when the governing equations are discretized using the FEM, and convergence in such problems is often poor. The problem of negative tangent stiffness matrices is most likely caused by grayscales or large deformations of the element mesh structure. Bruns et al. [61] circumvented this problem by eliminating node connections between low-density elements. Yoon et al. [62, 63] circumvented this problem by expressing solid and void elements using a rigid link structure for solid elements and a non-rigid link structure for void elements. The convergence performance was improved in both of these methods but the mesh distortion problem cannot be fundamentally solved in their method.

Particle methods, mesh-free methods [64–70], express continuum structures us-

ing particles and inherently avoid element-distortion problems. Smoothed Particle Hydrodynamics (SPH) method [67, 71–74] and Moving Particle Semi-implicit (MPS) methods [68, 75–77] are the major particle methods. SPH method represent spacial distribution of variables by taking the superpositions of variables multiplied by kernel functions at each particle. This method is originally developed for compressible flow problems, and applied to a number of fluid problems [78, 79]. In elastic problems, however, SPH often encounter numerical instability when tensile force applied. This problem is called tensile instability [80,81], in which particles many gather in a certain local area, creating other particle-free areas. On the other hand, MPS method uses particle interaction models to discretize the governing equations and tensile instability problem does not occur. A topology optimization method using MPS method for its nonlinear analysis may be an effective method for optimizing the design of devices that undergo large deformations and will be discussed in Chapter 5.

1.3 Thesis structure

This thesis summarizes my doctoral research during the past few years. It deals with optimization methods considering electrostatic-structural coupling effects and geometric nonlinearity, and proposes the design optimization methods for electrostatic actuators, mechanical resonators, and compliant mechanisms. The outline of each chapter is as follows.

In Chapter 2, an optimization method for electrostatic actuators is developed. The analysis of the electrostatic and structural coupled fields is discussed. A method for accurately calculating the driving forces that occur on the structural boundaries that change during the optimization is presented, and the basis of the optimization method for electrostatic actuators is explained.

Chapter 3 discusses an optimization method for electrostatic actuators considering driving force profiles, to accommodate real-world requirements encountered in

electrostatic actuator design problems. A multi-objective functional is formulated to obtain optimal configurations that achieve a prescribed driving force profile.

In Chapter 4, an topology optimization method for mechanical resonators is proposed. The optimum design problem is formulated to obtain an optimal configuration that proactively utilizes the dynamic instability of the structure. A objective functional is formulated based on the concept of kinetic energy maximization.

Chapter 5 discusses a topology optimization method for compliant mechanisms, mechanisms that undergo large deformations, and the use of MPS method that enables geometrically nonlinear analysis is discussed. An optimization method that incorporates the MPS method is presented and numerical examples are provided to verify the effectiveness of the proposed method.

Last, the conclusions of this thesis are provided in Chapter 6.

Chapter 2

Structural optimization of electrostatic actuators

2.1 Introduction

This chapter proposes a novel structural optimization method for the design of electrostatic actuators. The main difficulty when applying structural optimization in electrostatic actuator design problems lies in the calculation of the electrostatic forces. These calculations require clear structural boundaries because the electrostatic driving forces only occur on the structural boundaries, but these boundaries are poorly defined in grayscale areas. Here, a level set-based structural optimization is used for the design optimization of electrostatic actuators because it allows large changes in structural shapes and also provides clear structural boundaries, since the boundaries are expressed as an iso-surface of the level set function. In level set-based structural optimization methods, however, the expressed structural boundaries that move during the optimization seldom match the finite element mesh nodes, and this causes inaccuracies when the electrostatic forces are calculated. Therefore, to enable accurate analysis of the electrostatic forces, some kind of interpolation method or boundary expression method is required. A mesh adaptation scheme is developed here so that

the finite element mesh nodes closest to the structural boundaries snap to the boundaries after each update of the level set function.

The following describes the shape representation of the level set method and the formulations of the considered electrostatic actuator design problems. The electrostatic and elastic deformation fields are coupled. The sensitivity is derived using the adjoint variable method, and Maxwell's stress tensor is used when calculating the actuation forces. The proposed mesh adaptation scheme is explained and verified through numerical examples in which the results of electrostatic force calculations using this scheme are compared with those obtained by analysis, and those obtained by a method using a conventional ersatz material approach. Two numerical examples are presented to demonstrate the effectiveness of the proposed method.

2.2 Formulations

2.2.1 Structural optimization based on the level set method

Structural optimization based on the level set method is now explained. A domain filled with material, called the material domain Ω, is defined in a fixed design domain, D. The level set function $\phi(\boldsymbol{x})$ is defined as a signed distance function representing the least distance from a point $\boldsymbol{x}$ to the structural boundary, with the material domain Ω and the structural boundary, $\partial\Omega$, expressed by the level set function. That is, the shape of the structure is expressed by the level set function, which is positive in the material domain, negative in the void domain, and zero on the structural boundaries, as follows.

$$\begin{cases} \phi(\boldsymbol{x}) > 0 & \text{for} \quad \forall \boldsymbol{x} \in \Omega \setminus \partial\Omega \\ \phi(\boldsymbol{x}) = 0 & \text{for} \quad \forall \boldsymbol{x} \in \partial\Omega \\ \phi(\boldsymbol{x}) < 0 & \text{for} \quad \forall \boldsymbol{x} \in D \setminus \Omega\,, \end{cases} \tag{2.1}$$

where $\boldsymbol{x}$ is a point in the fixed design domain.

During the optimization, changes in the shape of the material domain are expressed by changes in the value of the level set function. A fictitious time, t, is introduced and a Hamilton-Jacobi equation represents the advection of the iso-surface of the level set function, expressed as the derivative of the level set function $\phi(\boldsymbol{x}(t), t)$ with respect to time t, as follows [31, 32]:

$$\frac{\partial \phi\left(\boldsymbol{x}, t\right)}{\partial t} + \frac{\mathrm{d}\boldsymbol{x}}{\mathrm{d}t} \cdot \nabla \phi\left(\boldsymbol{x}, t\right) = 0 \qquad \text{in } D, \tag{2.2}$$

where $\frac{\mathrm{d}\boldsymbol{x}}{\mathrm{d}t}$ is the advection of the iso-surface of the level set function defined at $\boldsymbol{x}$ in fixed design domain D. With the velocities of structural boundary movement in the normal direction denoted by $V_N\left(\boldsymbol{x}, t\right)$ and the normal direction vector denoted by $\boldsymbol{n}$, the following relation is obtained:

$$\frac{\mathrm{d}\boldsymbol{x}}{\mathrm{d}t} = V_N\left(\boldsymbol{x}, t\right) \boldsymbol{n}\,. \tag{2.3}$$

$\boldsymbol{n}$ is now defined as follows.

$$\boldsymbol{n} = \frac{\nabla \phi}{\mid \nabla \phi \mid} \tag{2.4}$$

Using equations (2.3) and (2.4), the Hamilton-Jacobi equation (2.2) is now rewritten as

$$\frac{\partial \phi\left(\boldsymbol{x}, t\right)}{\partial t} + V_N\left(\boldsymbol{x}, t\right) \boldsymbol{n} \cdot \nabla \phi\left(\boldsymbol{x}, t\right) = \frac{\partial \phi\left(\boldsymbol{x}, t\right)}{\partial t} + V_N\left(\boldsymbol{x}, t\right) \mid \nabla \phi\left(\boldsymbol{x}, t\right) \mid = 0 \quad \text{in } D. \tag{2.5}$$

In a level set-based structural optimization method, the derivative of the design variable of the objective functional represents the advection velocity of the zero iso-surface of the level set function $V_N\left(\boldsymbol{x}, t\right) \mid_{\phi=0}$.

The level set function is initialized so that it has a signed distance function characteristic and the function is updated using Eq.(2.5). However, the signed distance characteristic is lost after the update, so re-initialization [82, 83] of the level set function is usually required after several updates. On the other hand, Yamasaki et al. [42, 84]

proposed a method in which a geometric re-initialization of the level set function is performed after each update so that the signed distance function characteristic is strictly maintained. When the signed distance function characteristic is maintained, the updating of the level set function is facilitated because $\mid \nabla\phi(\boldsymbol{x},t) \mid = 1$, and Eq.(2.5) can then be simplified as shown in Eq.(2.6) below.

$$\frac{\partial\phi(\boldsymbol{x},t)}{\partial t} + V_N(\boldsymbol{x},t) = 0 \qquad \text{in } D. \tag{2.6}$$

In this research, the updating of the level set function is carried out in this manner. Note that the smoothness of a solution is not necessarily guaranteed when the solution is obtained using the Hamilton-Jacobi equation, so some kind of regularization is required during the optimization. The regularization method used in the presented method is explained in Section 2.3.2.

2.2.2 Equilibrium equations

When an electrostatic field is applied to the dielectric void domain, an electrostatic actuator operates in response to electrostatic forces acting on the actuator structure, which is a conductor. Since the structure deforms in response to electrostatic forces, the electrostatic and elastic fields need to be analyzed in order to evaluate the actuator performances.

Here, the material domain, Ω, and two boundaries, Γ_1 and Γ_2, at which voltages are applied, are defined in design domain D (Fig.2.1). Boundary Γ_1 is a fixed boundary and its electric potential is set to zero. Boundary Γ_2 is set at an appropriate location not connected to the material domain and its electric potential is set as V_{in}. Boundary Γ_3 is the boundary of the material domain. The electric potential V in the void domain and the dielectric tensor $\boldsymbol{D}_{\mathrm{e}}$ are set, and the equilibrium equation for

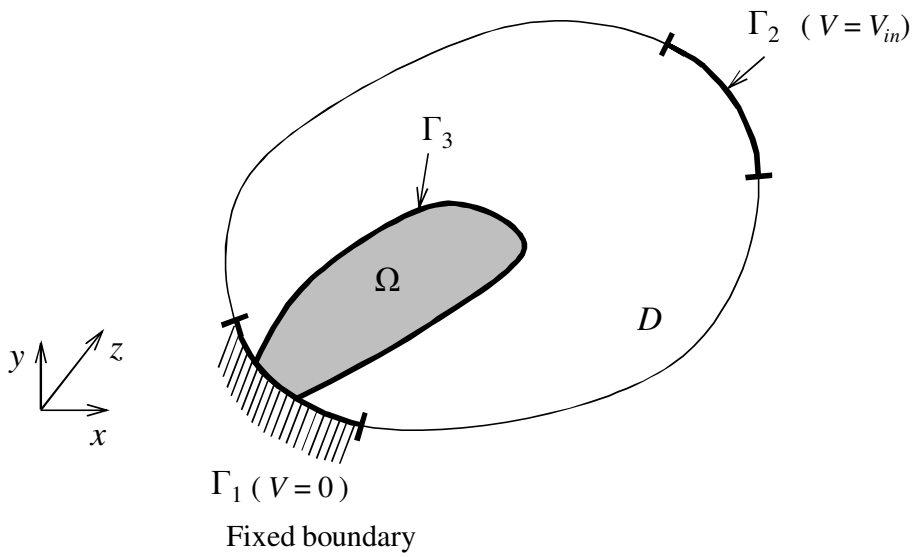

Figure 2.1: Design domain and boundary conditions of the electrostatic actuator design problem

the electrostatic field in the void domain is the following:

$$\int_{D\setminus\Omega} \nabla\hat{V} \cdot (\boldsymbol{D}_{\mathrm{e}} \nabla V)\, \mathrm{d}\Omega = 0\,, \tag{2.7}$$

where $\hat{V}$ is a test function and ' $\cdot$ ' represents the inner product of the vectors.

A rigorous evaluation of the elastic deformation caused by electrostatic forces requires nonlinear analyses that consider large deformations. However, in this chapter, linear analyses are used to determine deformations because only small deformations of the actuator are considered, and the objective functional pertains to a quantitative performance such as maximization of the deformation in a certain direction.

A traction, $\boldsymbol{t}$, arises from the electrostatic forces and acts on boundary Γ_3, causing the structure to deform elastically. It is assumed that the body force is sufficiently small so that it can be ignored. The equilibrium equation for the elastic deformation

field in the material domain is

$$\int_{\Omega} \boldsymbol{\epsilon}\left(\hat{\boldsymbol{u}}\right) : \boldsymbol{D}_{\mathrm{s}} : \boldsymbol{\epsilon}\left(\boldsymbol{u}\right) \mathrm{d}\Omega = \int_{\Gamma_3} \hat{\boldsymbol{u}} \cdot \boldsymbol{t} \mathrm{d}\Gamma, \tag{2.8}$$

where $\boldsymbol{D}_{\mathrm{s}}$ is the elastic tensor, $\boldsymbol{u}$ the deformation vector, and $\boldsymbol{\epsilon}$ the strain tensor. The symbol ' : ' represents the inner product of second-rank tensors. Traction $\boldsymbol{t}$ per unit area in Eq.(2.8) is defined in the following equation, considering only the terms related to the electrostatic field represented in the Maxwell's stress tensor.

$$\boldsymbol{t} = \begin{pmatrix} t_x \\ t_y \\ t_z \end{pmatrix} = -\epsilon_0 \begin{pmatrix} E_x^2 - \dfrac{\|\boldsymbol{E}\|^2}{2} & E_x E_y & E_x E_z \\ E_y E_x & E_y^2 - \dfrac{\|\boldsymbol{E}\|^2}{2} & E_y E_z \\ E_z E_x & E_z E_y & E_z^2 - \dfrac{\|\boldsymbol{E}\|^2}{2} \end{pmatrix} \cdot \begin{pmatrix} n_x \\ n_y \\ n_z \end{pmatrix}, \tag{2.9}$$

where ϵ_0 is the electric permittivity of the vacuum, $\boldsymbol{E}$ is the electric field vector, E_x, E_y, and E_z are the respective x, y, and z components of the electric field vector, and n_x, n_y, and n_z are the respective x, y, and z components of the normal vector on the material boundaries. The electric field vector $\boldsymbol{E}$ is given by taking the gradient of the electric potential V, as follows.

$$\boldsymbol{E} = -\nabla V \tag{2.10}$$

The equilibrium equations (2.7) and (2.8) are rewritten as an equilibrium equation defined in fixed design domain D, using the Heaviside function $H\left(\phi\right)$ as below [85].

$$\int_{D} \nabla \hat{V} \cdot \left(\boldsymbol{D}_{\mathrm{e}} \nabla V\right) \left(1 - H\left(\phi\right)\right) \mathrm{d}\Omega = 0 \tag{2.11}$$

$$\int_{D} \boldsymbol{\epsilon}\left(\hat{\boldsymbol{u}}\right) : \boldsymbol{D}_{\mathrm{s}} : \boldsymbol{\epsilon}\left(\boldsymbol{u}\right) H\left(\phi\right) \mathrm{d}\Omega = \int_{\Gamma_3} \hat{\boldsymbol{u}} \cdot \boldsymbol{t} \ \mathrm{d}\Gamma \tag{2.12}$$

The physics problem expressed in the above two equations is the so-called strong coupling problem between the electrostatic field and the elastic deformation field. The

elastic deformation field changes when the electrostatic field changes and the electrostatic field changes in response to changes in the elastic deformation field. To solve this problem, the electrostatic field represented as Eq.(2.11) and the elastic deformation field represented as Eq.(2.12) are sequentially solved in an iterated manner. After each iterative calculation, a convergence test is carried out and the electrostatic and elastic deformation fields at the equilibrium state are thereby obtained.

2.2.3 Formulations of optimization problem

When considering electrostatic actuators, the function whereby a certain boundary deforms a certain amount in a certain direction is one of the most basic functions, although various other functions are also required. When designing electrostatic actuators, setting an appropriate displacement of the electrodes is important because a pull-in effect, in which two electrodes that contact each other then remain stuck together, may occur if the distance between the two electrodes becomes too small. A structural optimization problem to find structures that satisfy the above performance requirements is discussed below.

The aim is to design an actuator whose displacement at output port Γ_{out} in material domain Ω is as close as possible to a designated displacement, $\boldsymbol{u}^*$, with the displacement vector defined as $\boldsymbol{u}$, the potential of boundary Γ_1 set as zero, and the potential of boundary Γ_2 as V_{in}.

$$\inf_{\Omega} \qquad F = \int_{\Gamma_{\text{out}}} \left\| \boldsymbol{u} - \boldsymbol{u}^* \right\|^2 \mathrm{d}\Gamma \tag{2.13}$$

$$\text{subject to} \quad \int_D \nabla \hat{V} \cdot \left(\boldsymbol{D}_{\text{e}} \nabla V \right) \left(1 - H\left(\phi \right) \right) \mathrm{d}\Omega = 0 \tag{2.14}$$

$$\int_D \boldsymbol{\epsilon}\left(\hat{\boldsymbol{u}} \right) : \boldsymbol{D}_{\text{s}} : \boldsymbol{\epsilon}\left(\boldsymbol{u} \right) H\left(\phi \right) \mathrm{d}\Omega = \int_{\Gamma_3} \hat{\boldsymbol{u}} \cdot \boldsymbol{t} \ \mathrm{d}\Gamma. \tag{2.15}$$

Note that the designated displacement $\boldsymbol{u}^*$ that is used in the objective functional must be set to a very small value, because linear analyses are used for the elastic de-

formation field; large deformations are not considered. If the designated displacement is set to a relatively large value, the displacement at output boundary Γ_{out} must be verified to be sufficiently small.

2.3 Numerical implementation

The flowchart of the optimization algorithm for the proposed method is shown in Fig.2.2. The initial value of the level set function is given at the first step. The mesh adaptation procedure is then carried out to create a finite element mesh in which the nodes close to the structural boundary move to positions on the actual boundaries. The details of this mesh adaptation scheme are explained in Section 2.3.1. After the mesh adaptation, the equilibrium equations for the electrostatic and elastic deformations are solved using the FEM. First, the electrostatic field is solved and the electrostatic forces on the boundaries of the material domain are analyzed. Next, the elastic deformation field is solved using the electrostatic forces as the traction forces. As described above, the electrostatic and the elastic deformation fields are strongly coupled and the two fields are iteratively and sequentially solved. The convergence of the electrostatic and the elastic deformation fields is judged by determining if the difference between the displacements in the present and previous iterations is below a certain threshold. If convergence has not occurred, the process returns to the third step, in which the electrostatic field is solved, and this process is repeated until the coupled equations converge. After the convergence of the equilibrium equations, the objective functional is calculated, and if the objective functional is converged, the algorithmic process terminates. If the objective functional is not converged, the sensitivity of the objective functional is found by solving the adjoint problem for the electrostatic and elastic deformation fields. The level set function is then updated using this sensitivity via the following equation, which is the spatially discretized form

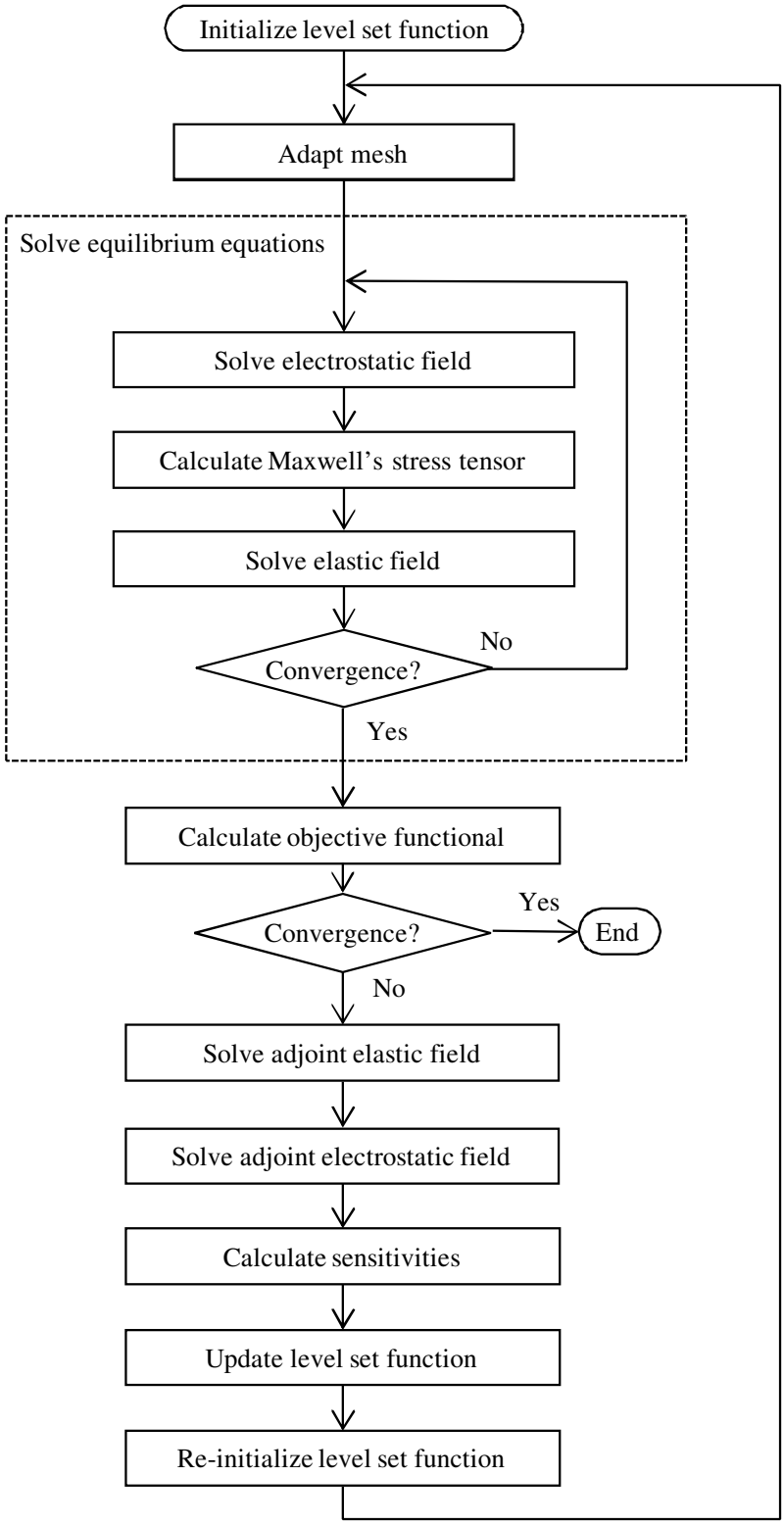

Figure 2.2: Flowchart of the optimization procedure for the electrostatic actuator design problem

of Eq.(2.6).

$$\boldsymbol{\Phi}^{t+\Delta t} = \boldsymbol{\Phi}^{t} - \Delta t \ \boldsymbol{V}_N^t \tag{2.16}$$

$\boldsymbol{\Phi}^t$ is a vector that represents the level set function values at each node at time t, $\boldsymbol{V}_N^t$ is a vector that represents the normal direction velocity values at each node at time t, and Δt is the time increment. The level set function is reinitialized after it is updated. A geometric reinitialization method [84] is applied for the reinitialization as explained in Section 2.2.1. After the reinitialization, the procedure returns to the mesh adaptation step to recreate the mesh and ensure that nodes close to the boundaries are precisely aligned along the boundaries. Note that the desired performances may be achieved by a number of design candidates. In this research, a local optimum that achieves the desired performances is searched for by setting an appropriate initial structure and then moving the structural boundaries. Therefore, the optimal structure obtained by the proposed method that achieves the desired performances resembles the initial structure.

2.3.1 Mesh adaptation scheme

The forces driving an electrostatic actuator are the electrostatic forces that occur on the structural boundaries. To obtain an appropriate design, these electrostatic forces must be precisely calculated during the optimization process. Such calculations, however, are not straightforward in level set-based shape optimization methods because the FEM nodes seldom lie on the structural boundaries. To accurately calculate the forces on the structural boundaries, the position of the finite elements nodes and the structural boundaries need to be congruent.

In this study, the mesh adaptation scheme originally proposed by Yamasaki et al. [42] is further developed, extending it to electrostatic actuator optimization problems. The nodes in the void domain that are close to the structural boundaries are moved so that they lie precisely on the structural boundaries. When only the nodes

close to the boundaries are moved, certain element shapes become distorted, which lowers mesh quality and therefore degrades the accuracy of the analysis. To mitigate this problem, a Laplacian smoothing method is used.

The formulation of the mesh adaptation scheme is as follows. The movement vectors of the nodes, i.e., the displacements from original node positions to new positions, are represented as $\boldsymbol{d}_x$, $\boldsymbol{d}_y$, and $\boldsymbol{d}_z$. The mesh adaptation is executed by updating the node coordinates according to these movement vectors, as in Eq.(2.17).

$$\begin{cases} \boldsymbol{X} = \boldsymbol{X}_0 + \boldsymbol{d}_x \\ \boldsymbol{Y} = \boldsymbol{Y}_0 + \boldsymbol{d}_y \\ \boldsymbol{Z} = \boldsymbol{Z}_0 + \boldsymbol{d}_z \,, \end{cases} \tag{2.17}$$

where $\boldsymbol{X}$, $\boldsymbol{Y}$, and $\boldsymbol{Z}$ are the coordinates of all nodes after the mesh adaptation, and $\boldsymbol{X}_0$, $\boldsymbol{Y}_0$, and $\boldsymbol{Z}_0$ are the coordinates of all nodes before the mesh adaptation. The derivation of the movement vectors $\boldsymbol{d}_x$, $\boldsymbol{d}_y$, and $\boldsymbol{d}_z$ for each node is explained below.

Figure 2.3(a) shows the mesh structure before the mesh adaptation. Two-dimensional triangular elements are used in all the illustrations of Fig.2.3 and for the explanation of the mesh adaptation scheme, although this is a general scheme that is also valid for three-dimensional mesh structures. The gray areas represent the material domain Ω and the white areas represent the void domain. First, the elements that consist of both material and void are selected, and measurement points, indicated by the black dots in Fig.2.3(b), are populated at even intervals on the structural boundaries $\partial\Omega$ within each element. Nodes that exist in the void domain portion of the selected elements are denoted N_i, as shown in Fig.2.3(c). As shown in Fig.2.3(d), the N_i nodes are moved to the closest measurement point on the structural boundary. The components of the movement vectors d_{x_i}, d_{y_i}, and d_{z_i} are calculated.

Next, the components of movement vectors for other nodes are calculated using the Laplacian smoothing method [86, 87]. The movement vectors $\boldsymbol{d}_x$, $\boldsymbol{d}_y$, and $\boldsymbol{d}_z$ are

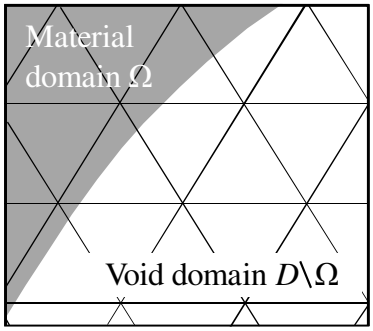

(a) Initial mesh

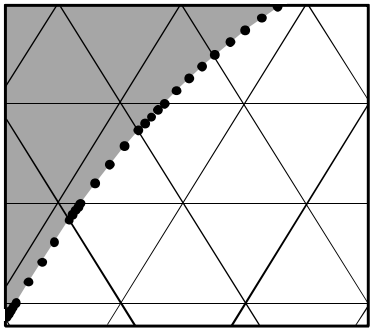

(b) Measurement points

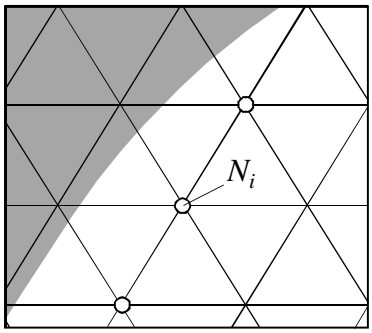

(c) Nodes N_i

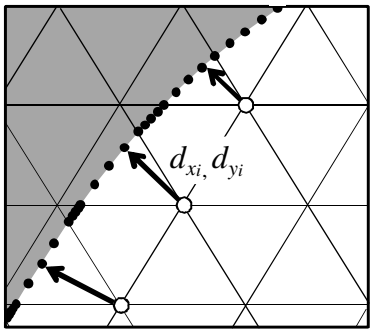

(d) Movement vectors d_{xi}, d_{yi}

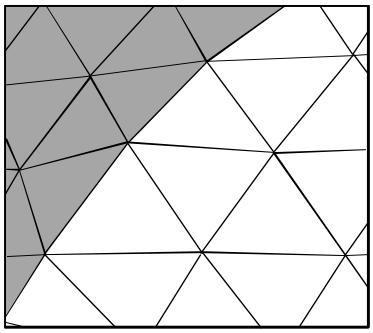

(e) Adapted mesh

Figure 2.3: Mesh adaptation scheme

obtained by solving the following equations, using the FEM.

$$\boldsymbol{K}\ \boldsymbol{d}_x = 0 \qquad \text{with} \quad d_{x_i} = \overline{d_{x_i}} \tag{2.18}$$

$$\boldsymbol{K}\ \boldsymbol{d}_y = 0 \qquad \text{with} \quad d_{y_i} = \overline{d_{y_i}} \tag{2.19}$$

$$\boldsymbol{K}\ \boldsymbol{d}_z = 0 \qquad \text{with} \quad d_{z_i} = \overline{d_{z_i}} \tag{2.20}$$

$$\boldsymbol{K} := \bigcup_{e=1}^{n_e} \int_{A_e} \nabla^{\mathrm{T}} \boldsymbol{N}\, \nabla \boldsymbol{N}\ \mathrm{d}\Omega\,, \tag{2.21}$$

where $\overline{d_{x_i}}$, $\overline{d_{y_i}}$, and $\overline{d_{z_i}}$ are the components of the movement vectors of the nodes that have been moved to the structural boundaries, calculated according to the procedure explained above. The total number of elements in design domain D is represented as n_e, $\int_{A_e} * \,\mathrm{d}\Omega$ is the domain integral of the e-th element, and $\boldsymbol{N}$ is the shape function. Using the above procedure, the movement vectors $\boldsymbol{d}_x$, $\boldsymbol{d}_y$, and $\boldsymbol{d}_z$ for all the nodes are calculated, and mesh adaptation is completed as shown in Fig.2.3(e).

When the curvature of a structural boundary is very large, the boundary arcs as a circle with a central focus on a node, and this node then has multiple closest points at different locations on the boundary. In the proposed method, to avoid this kind of situation, the structural boundaries are smoothed using a sensitivity filter, as discussed in Section 2.3.2. On the other hand, there are cases when multiple nodes share the same closest point on a boundary. In such cases, these nodes are excluded from the set of nodes that are forcibly displaced.

The mesh quality is examined using the following formula.

$$q = \frac{4\sqrt{3}g}{h_1^2 + h_2^2 + h_3^2}\,, \tag{2.22}$$

where q is the mesh quality index, g is the area, and h_1, h_2, and h_3 are the side lengths of the triangular elements [88, 89]. The value of q ranges between 0 and 1 and an equilateral triangle has a q value of 1. The quality of solutions is unaffected when q is larger than 0.3. The value of q is computed for all elements at every iteration. In this

manner, the mesh adaptation scheme enables accurate calculation of the electrostatic forces. Note that the calculation cost of this scheme increases for three-dimensional problems, although it is not especially high in two-dimension problems.

To calculate the electrostatic forces at the nodes on the structural boundaries, only the nodes that are on the boundaries need to be selected. Any element with a side that contacts a structural boundary has two nodes for which the values of the level set function are zero. These $\phi = 0$ nodes are selected and the Maxwell's stress tensors at these selected nodes are then calculated. Maxwell's stress tensors for nodes not on the structural boundaries are set equal to zero.

2.3.2 Sensitivity analysis

As discussed above, the updating of the level set function using Eq.(2.6) requires the design sensitivity V_N. The design sensitivity is obtained by the adjoint variable method in this research.

For the constraint problem, Eq.(2.13)$\sim$(2.15), the Lagrangian is formulated by replacing the test functions $\hat{V}$ and $\hat{\boldsymbol{u}}$ with the adjoint variables $\tilde{V}$ and $\tilde{\boldsymbol{u}}$.

$$\begin{aligned}\bar{F} = &\int_{\Gamma_{\text{out}}} \left\|\boldsymbol{u} - \boldsymbol{u}^*\right\|^2 \mathrm{d}\Gamma + \int_D \nabla\tilde{V} \cdot \left(\boldsymbol{D}_{\text{e}} \nabla V\right) \left(1 - H\left(\phi\right)\right) \mathrm{d}\Omega \\ &+ \left[\int_D \boldsymbol{\epsilon}\left(\tilde{\boldsymbol{u}}\right) : \boldsymbol{D}_{\text{s}} : \boldsymbol{\epsilon}\left(\boldsymbol{u}\right) H\left(\phi\right) \mathrm{d}\Omega - \int_{\Gamma_3} \tilde{\boldsymbol{u}} \cdot \boldsymbol{T}\, \mathrm{d}\Gamma\right] \end{aligned} \tag{2.23}$$

Next, the sensitivity of Lagrangian $\bar{F}$ is obtained using the Fréchet derivative of

Lagrangian $\bar{F}$ with respect to the design variable ϕ, as shown below.

$$\begin{aligned}
&\left\langle \frac{\mathrm{d}\bar{F}}{\mathrm{d}\phi}, \delta\phi \right\rangle \\
&= \left\langle \frac{\partial \left[\int_D \nabla\tilde{V} \cdot \left(\boldsymbol{D}_\mathrm{e} \nabla V \right) \left(1 - H\left(\phi \right) \right) \mathrm{d}\Omega \right]}{\partial \phi} + \frac{\partial \left[\int_D \boldsymbol{\epsilon}\left(\tilde{\boldsymbol{u}} \right) : \boldsymbol{D}_\mathrm{s} : \boldsymbol{\epsilon}\left(\boldsymbol{u} \right) H\left(\phi \right) \mathrm{d}\Omega \right]}{\partial \phi}, \delta\phi \right\rangle \\
&+ \left\langle \frac{\partial \left[\int_D \nabla\tilde{V} \cdot \left(\boldsymbol{D}_\mathrm{e} \nabla V \right) \left(1 - H\left(\phi \right) \right) \mathrm{d}\Omega \right]}{\partial V} - \frac{\partial \left[\int_{\Gamma_3} \tilde{\boldsymbol{u}} \cdot \boldsymbol{T} \, \mathrm{d}\Gamma \right]}{\partial V}, \delta V \right\rangle \left\langle \frac{\partial V}{\partial \phi}, \delta\phi \right\rangle \\
&+ \left\langle \frac{\partial \left[\int_D \boldsymbol{\epsilon}\left(\tilde{\boldsymbol{u}} \right) : \boldsymbol{D}_\mathrm{s} : \boldsymbol{\epsilon}\left(\boldsymbol{u} \right) H\left(\phi \right) \mathrm{d}\Omega \right]}{\partial \boldsymbol{u}} + \frac{\partial \left[\int_{\Gamma_\mathrm{out}} \left\| \boldsymbol{u} - \boldsymbol{u}^* \right\|^2 \mathrm{d}\Gamma \right]}{\partial \boldsymbol{u}}, \delta\boldsymbol{u} \right\rangle \left\langle \frac{\partial \boldsymbol{u}}{\partial \phi}, \delta\phi \right\rangle
\end{aligned} \tag{2.24}$$

Setting adjoint fields that satisfy Eq.(2.25) and (2.26), and eliminating the second and third terms in the right side of Eq.(2.24), the sensitivity is obtained as shown in Eq.(2.27).

$$\int_D \nabla\tilde{V} \cdot \left(\boldsymbol{D}_\mathrm{e} \delta\left(\nabla V \right) \right) \left(1 - H\left(\phi \right) \right) \mathrm{d}\Omega = \int_{\Gamma_3} \tilde{\boldsymbol{u}} \cdot \delta\boldsymbol{T} \, \mathrm{d}\Gamma \tag{2.25}$$

$$\int_D \boldsymbol{\epsilon}\left(\tilde{\boldsymbol{u}} \right) : \boldsymbol{D}_\mathrm{s} : \boldsymbol{\epsilon}\left(\delta\boldsymbol{u} \right) H\left(\phi \right) \mathrm{d}\Omega = - \int_{\Gamma_\mathrm{out}} 2 \left(\boldsymbol{u} - \boldsymbol{u}^* \right) \delta\boldsymbol{u} \mathrm{d}\Gamma \tag{2.26}$$

$$\left\langle \frac{\mathrm{d}\bar{F}}{\mathrm{d}\phi}, \delta\phi \right\rangle = \left\langle \frac{\partial \left\{ \int_D \left[\nabla\tilde{V} \cdot \left(\boldsymbol{D}_\mathrm{e} \nabla V \right) \left(1 - H\left(\phi \right) \right) + \boldsymbol{\epsilon}\left(\tilde{\boldsymbol{u}} \right) : \boldsymbol{D}_\mathrm{s} : \boldsymbol{\epsilon}\left(\boldsymbol{u} \right) H\left(\phi \right) \right] \mathrm{d}\Omega \right\}}{\mathrm{d}\phi}, \delta\phi \right\rangle \tag{2.27}$$

Now, the right side of Eq.(2.25) is converted to a domain integral in D and moved to the left side of the equation. A Dirac delta function, $\delta\left(\boldsymbol{x} \right)$, is used to convert the boundary integral to the domain integral. The Dirac delta function is defined using the Heaviside function $H\left(\phi \right)$ and the normal vector of the Heaviside function, $\boldsymbol{n}_H$,

as follows [85].

$$\begin{aligned}\delta(\boldsymbol{x}) &= \nabla H(\phi)\cdot\boldsymbol{n}_H \\ &= \frac{\mathrm{d}H(\phi)}{\mathrm{d}\phi}\nabla\phi\cdot\frac{\nabla\phi}{|\nabla\phi|} \\ &= \frac{\mathrm{d}H(\phi)}{\mathrm{d}\phi}|\nabla\phi| \end{aligned} \tag{2.28}$$

Eq.(2.25) is now rewritten as follows, using Eq.(2.28).

$$\int_D \left[\nabla\tilde{V}\cdot(\boldsymbol{D}_{\mathrm{e}}\delta(\nabla V))(1-H(\phi)) - \tilde{\boldsymbol{u}}\cdot\delta\boldsymbol{T}\,\frac{\mathrm{d}H(\phi)}{\mathrm{d}\phi}|\nabla\phi|\right]\mathrm{d}\Omega = 0 \tag{2.29}$$

The following function, $H_{\mathrm{a}}(\phi)$, is used for the Heaviside function $H(\phi)$ of $\frac{\mathrm{d}H(\phi)}{\mathrm{d}\phi}$ in Eq.(2.27) and (2.29), since the Heaviside function is a step function.

$$H_{\mathrm{a}}(\phi) = \begin{cases} 0 & (\phi < -w) \\ \dfrac{1}{2} + \dfrac{15}{16}\left(\dfrac{\phi}{w}\right) - \dfrac{5}{8}\left(\dfrac{\phi}{w}\right)^3 + \dfrac{3}{16}\left(\dfrac{\phi}{w}\right)^5 & (-w \leqslant \phi \leqslant w), \\ 1 & (w < \phi) \end{cases} \tag{2.30}$$

where w is the transition width of the boundaries.

The sensitivity $\left\langle \frac{\mathrm{d}\bar{F}}{\mathrm{d}\phi}, \delta\phi \right\rangle$ obtained by Eq.(2.27) may not be sufficiently smooth, as explained in Section 2.2.1, so a Helmholtz type of filter [42] is used for the regularization in this research. That is, the regularization is carried out using the following equation, with the regularized sensitivity defined as $\left\langle \frac{\mathrm{d}\bar{F}}{\mathrm{d}\phi}, \delta\phi \right\rangle^*$.

$$\left\langle \frac{\mathrm{d}\bar{F}}{\mathrm{d}\phi}, \delta\phi \right\rangle^* + R^2\,\nabla^2 \left\langle \frac{\mathrm{d}\bar{F}}{\mathrm{d}\phi}, \delta\phi \right\rangle^* = \left\langle \frac{\mathrm{d}\bar{F}}{\mathrm{d}\phi}, \delta\phi \right\rangle, \tag{2.31}$$

where R is a parameter that affects the smoothness of the solution. $\left\langle \frac{\mathrm{d}\bar{F}}{\mathrm{d}\phi}, \delta\phi \right\rangle^* = \left\langle \frac{\mathrm{d}\bar{F}}{\mathrm{d}\phi}, \delta\phi \right\rangle$ when $R = 0$ and Eq.(2.31) becomes equivalent to Poisson's equation as $R \to \infty$.

This regularized sensitivity $\left\langle \frac{\mathrm{d}\bar{F}}{\mathrm{d}\phi}, \phi \right\rangle^*$ is used for the value of V_N in Eq.(2.6) to update the level set function. To have V_N assume the velocity values of structural boundary movement in the normal direction, V_N values at nodes that are not on the structural boundaries are replaced with the V_N values of the closest nodes that lie on the structural boundaries.

2.4 Numerical examples

First, the operation of the proposed mesh adaptation scheme for calculating the electrostatic force is verified. The effectiveness of the proposed optimization method for the design of electrostatic actuators is then examined in two numerical examples in which a plane stress condition is assumed.

2.4.1 Verification of mesh adaptation scheme suitability

In this section, the suitability of the mesh adaptation scheme proposed in Section 2.3.1 is verified. The electrostatic force for an infinite parallel plate type of electrode can be solved analytically, but it cannot be solved through the FEM. Therefore, a sufficiently large parallel plate type of electrode is used, with electrodes that are 1μm thick, 42μm wide, and spaced 8μm apart. A voltage of 25V is applied between the two electrodes. An evaluation region 20μm wide and 8μm high is set at the center of electrodes (Fig.2.4). The analysis domain has a depth of 1m. The material properties used in this problem are the permittivity of the void and material domains. The vacuum permittivity of the void domain is $8.85 \times 10^{-12}\mathrm{Fm}^{-1}$, and that of material domain is defined as being 10^3 times larger, which is a sufficient degree of difference. The absolute value of the electrostatic forces occurring on the electrode surfaces within the evaluation region is solved using an adapted mesh structure realized by the proposed method. For comparison, these forces are also solved analytically and by

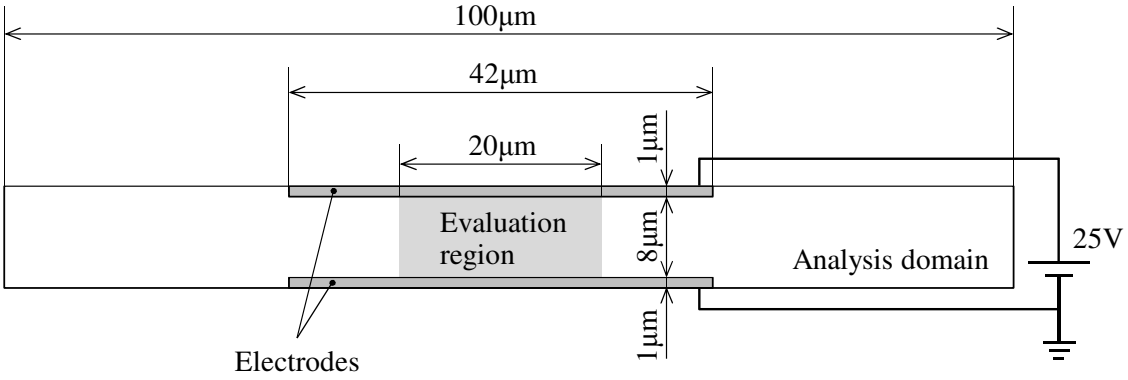

Figure 2.4: Parallel plate model

using a non-adapted mesh structure obtained by an ersatz material approach [32,34], a conventional approach that avoids re-meshing when using a level set method. In this approach, the left side of Eq.(2.12) is approximated as follows.

$$\int_{\Gamma_3} \hat{\boldsymbol{u}} \cdot \boldsymbol{t} \, \mathrm{d}\Gamma \simeq \int_D \hat{\boldsymbol{u}} \cdot \boldsymbol{t} \frac{\mathrm{d}H_a(\phi)}{\mathrm{d}\phi} \|\nabla\phi\| \, \mathrm{d}\Omega \tag{2.32}$$

The electrostatic forces in Cases 1, 2, and 3 are respectively solved analytically, by using the adapted mesh obtained via the proposed mesh adaptation scheme, and by using the non-adapted mesh obtained via the ersatz material approach (Table 2.1). The analytical (Case 1) and adapted mesh (Case 2) solutions are nearly equal, but

Table 2.1: Comparison of electrostatic forces for parallel plate type electrode [N]

Case 1	Case 2	Case 3
8.65×10^{-4}	8.72×10^{-4}	4.74×10^{-6}

the electrostatic force provided by the non-adapted mesh structure (Case 3) was much less than that of the other solutions. The electrostatic force is undervalued in Case 3 due to underevaluation of the electric field vector $\boldsymbol{E}$, because the material properties

have intermediate values between those of the material and void domains around the structural boundaries on which the electrostatic forces occur. Based on the above results, it is confirmed that the electrostatic force is appropriately obtained using the proposed mesh adaptation scheme. Furthermore, the ersatz material approach, in which the mesh is not adapted to the boundaries, does not provide accurate analysis of the electrostatic forces, and thus is not ideal for solving electrostatic actuator optimization problems.

2.4.2 Electrostatic actuator design 1

The model for the first electrostatic actuator design (Example 1) is shown in Fig.2.5. The size of the fixed design domain D is $100\mu\text{m} \times 50\mu\text{m}$ and a solid beam structure

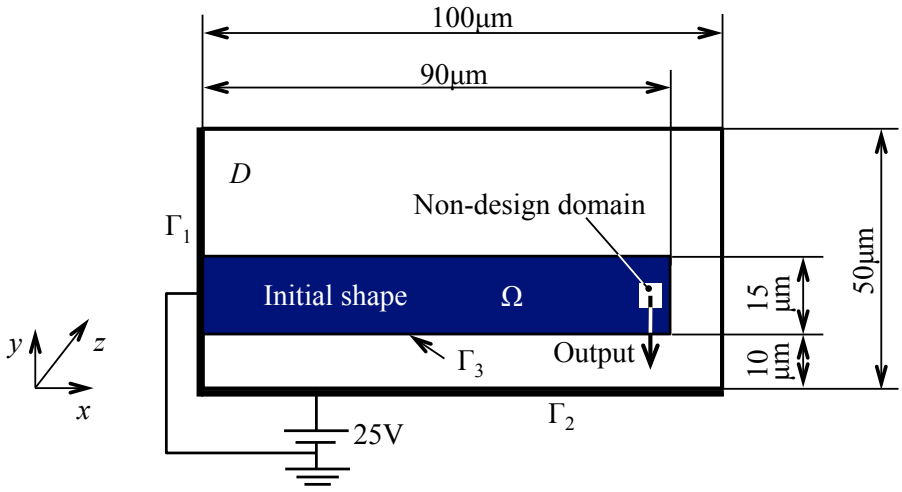

Figure 2.5: Design domain, boundary conditions, and initial configurations of Example 1

whose size is $90\mu\text{m} \times 15\mu\text{m}$ is set as the initial electrode structure. The depth in the z direction is $10\mu\text{m}$. A small square non-design domain is defined near the tip of the electrode Ω as the output port, and the displacement of the boundary Γ_{out} of this non-design domain is evaluated as the displacement of the electrode. A voltage of 0V is applied at boundary Γ_1, 100V is applied at boundary Γ_2, and the aim is to find an

optimal structure that deforms a set distance of 2μm in the $-y$ direction. Domain Ω has Young's modulus set as 153GPa and a Poisson's ratio of 0.23, assuming that the electrode material is silicon. The electric permittivity of the void domain $D \setminus \Omega$ is set equal to the vacuum permittivity of 8.85×10^{-12}F/m. The optimal configuration obtained by the optimization is shown in Figs.2.6(a) and (b), and the history of objective functional values is shown in Fig.2.7(a).

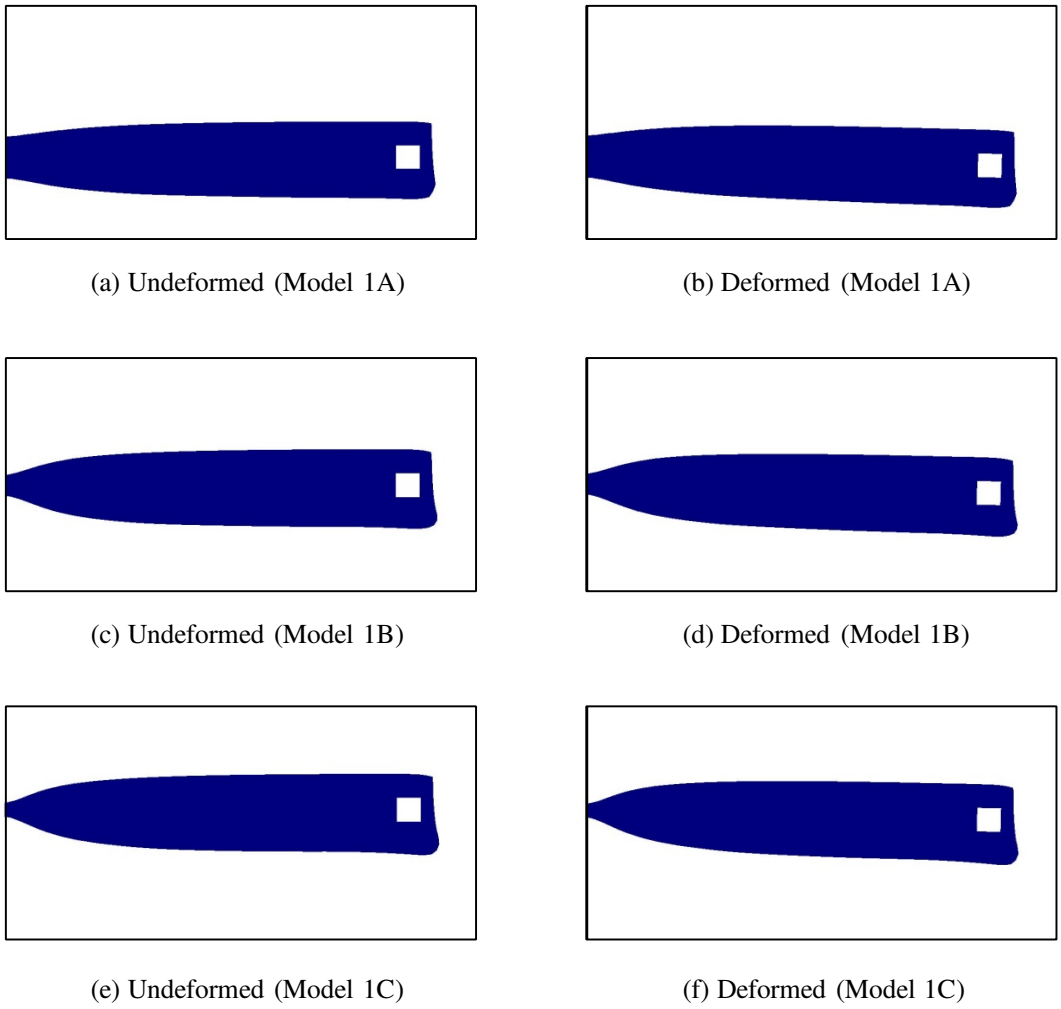

(a) Undeformed (Model 1A)

(b) Deformed (Model 1A)

(c) Undeformed (Model 1B)

(d) Deformed (Model 1B)

(e) Undeformed (Model 1C)

(f) Deformed (Model 1C)

Figure 2.6: Optimal configurations and deformed shapes of Example 1

Figure 2.6(a) shows the shape of the electrode Ω after the optimization and

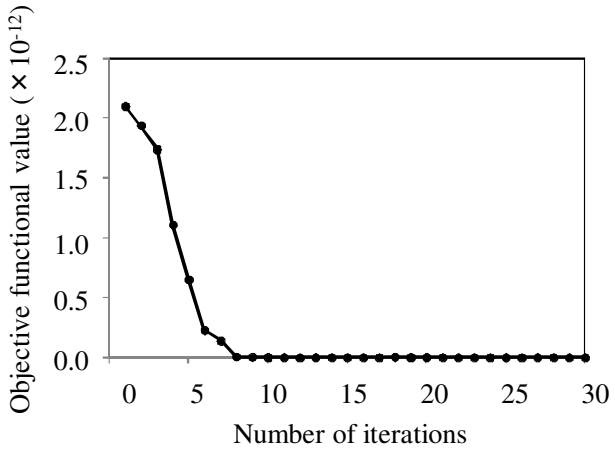

(a) Model 1A

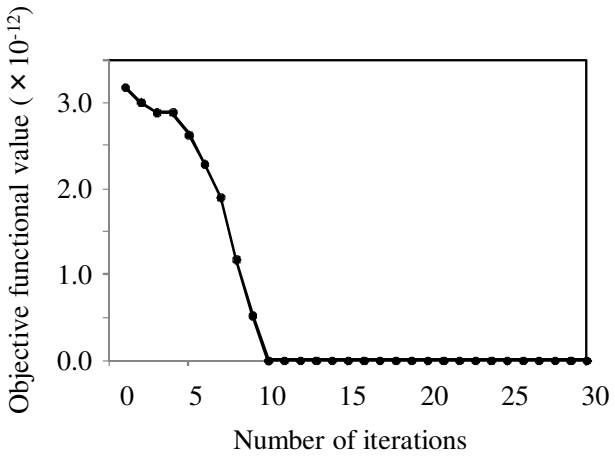

(b) Model 1B

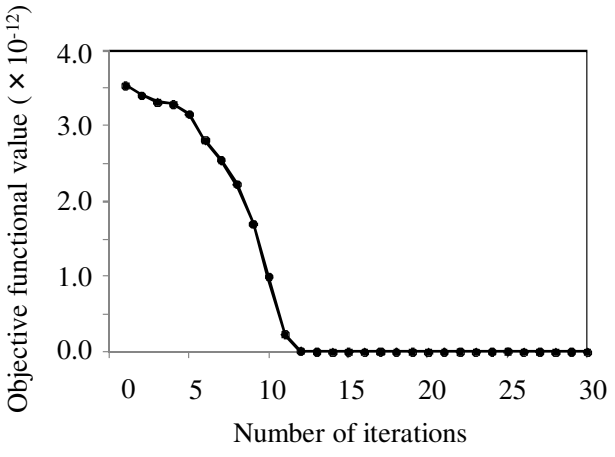

(c) Model 1C

Figure 2.7: History of objective functional of Example 1

Fig.2.6(b) shows the shape of the electrode Ω after deformation, when a voltage of 25V is applied to the electrode shown in Fig.2.6(a). The shape of the optimal configuration for Model 1A tapers toward the root of the electrode, which facilitates bending in the $-y$ direction. The bottom edge at the electrode tip is lengthened and rounded, which increases the electrostatic force that occurs on the electrode surface $\partial\Omega$ at that location. The optimal configuration achieves the performance objective of a 2μm displacement in the $-y$ direction when a voltage of 25V is applied, as shown in Fig.2.6(b). The objective functional decreases monotonically and converges after approximately 8 iterations.

Next, two additional optimizations are performed using the original model but with the initial position of the upper electrode moved 5μm or 10μm in $+y$ direction (Model 1B and Model 1C, respectively). The optimal configurations of Model 1B and Model 1C are shown in Figs.2.6(c)–(f). The area of attachment at the extreme left is shown to decrease as the initial electrode shape is placed farther from the lower fixed electrode. In addition, the slightly bulbous lower corner of the tip of the upper electrode increases in size as the initial electrode shape is placed farther from the lower fixed electrode. These changes in the shape of the electrode Ω make the electrode easier to bend and more responsive to the application of electrostatic forces when the position of the electrode is higher, since the electrostatic forces between the electrodes is considerably reduced, being inversely proportional to the square of the separation distance. Furthermore, the changes in the shape of the electrode increase its surface area and this proportionally increases the electrostatic force operating between the electrodes. The displacements for both Model 1B and Model 1C are 2μm in the $-y$ direction when a voltage of 25V is applied to the electrodes, indicating that both optimal configurations achieve the movement objective. The histories of the objective functionals are shown in Figs.2.7(b) and (c). The objective functionals of Models 1B and 1C decrease monotonically and converge after approximately 13 and 11 iterations, respectively. The obtained configurations that achieved the desired

performances may, however, not be globally optimal.

2.4.3 Electrostatic actuator design 2

The details for the second electrostatic actuator design (Example 2) are shown in Fig.2.8. The lower left and lower right boundaries, Γ_1, of the design domain D are

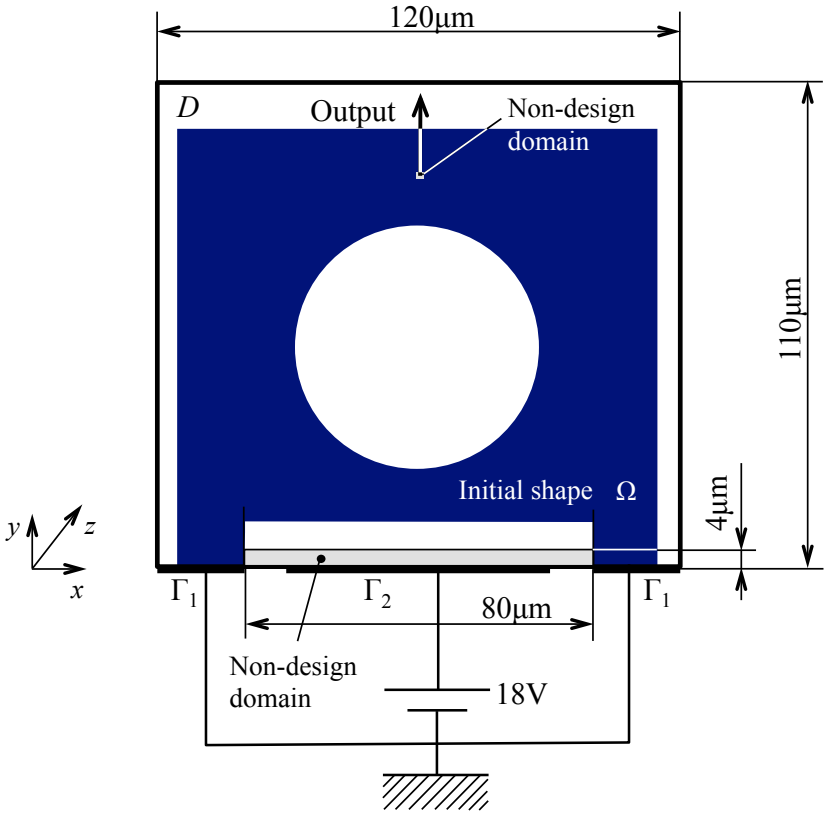

Figure 2.8: Design domain, boundary conditions, and initial configurations of Example 2

fixed and the applied voltage is set to zero. A voltage of 18V is applied at boundary Γ_2 that is centered between the fixed boundaries. A small, square non-design domain, which is an output area, is defined in the upper area of the design domain D and the objective is to obtain a displacement of its boundary, Γ_{out}, of 1μm in the $+y$ direction. The material domain Ω has a Young's modulus of 153GPa, Poisson's ratio is 0.23, and the electric permittivity is the vacuum permittivity, 8.85×10^{-12}F/m, assuming

that the material is silicon, the same as for Example 1. The depth of the model in the z direction is 1μm. A second non-design domain is defined above boundary Γ_2, whose size is $80\mu\text{m} \times 4\mu\text{m}$, to prevent the two electrodes from contacting each other during the optimization process. The optimal configurations are shown in Fig.2.9. For clarity, the deformation of the electrode when a voltage of 18V is applied is shown magnified by a factor of $3\times$ in Fig.2.9(b). The optimal structure has a diamond-shaped hole at the center and thin shapes appear at the left, right, top, and bottom faces of the structure. The obtained shape achieves the desired deformation in the $+y$ direction of 1μm at the output area. The history of objective functional is shown

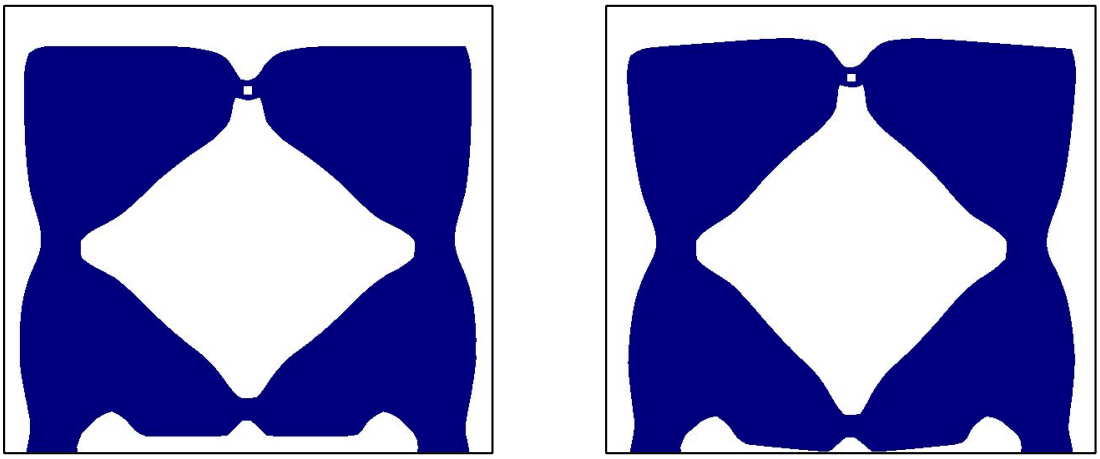

(a) Undeformed (b) Deformed ($\times 3$)

Figure 2.9: Optimal configurations and deformed shapes of Example 2

in Fig.2.10. The objective functional converged after approximately 19 iterations and an optimal configuration that achieves the desired performance was obtained.

The two examples explained above demonstrate that the proposed method is useful for the design of electrostatic actuators, since the objective functionals converged and the obtained structures achieved the movement objectives.

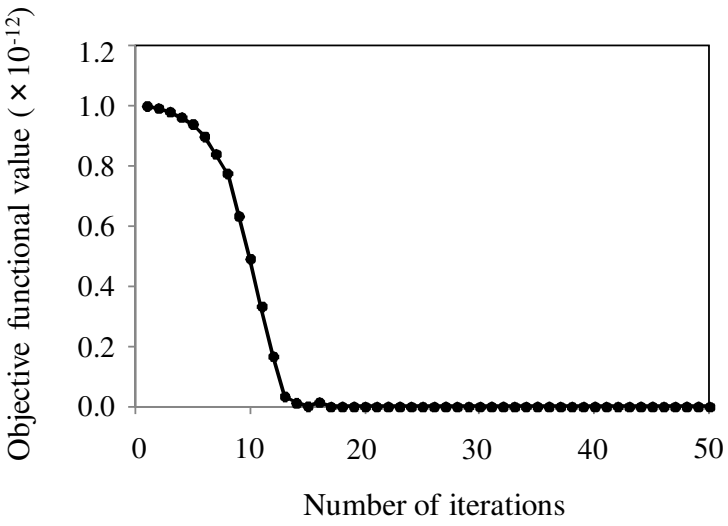

Figure 2.10: History of objective functional of Example 2

2.5 Conclusions

A structural optimization design method for electrostatic actuators using a level set-based optimization method was developed. This research obtained the following results.

(1) The basic design requirements for electrostatic actuators that utilize elastic deformation caused by electrostatic forces were clarified, and an optimization problem was formulated by defining an objective functional that facilitates the derivation of the adjoint equation. The design sensitivity was derived based on this formulation and the adjoint variable method.

(2) A mesh adaptation scheme based on the level set method and Laplacian smoothing was developed so that the mesh precisely adapts to shape changes, which enables accurate calculation of the Maxwell's stress tensors on the structural boundaries.

(3) Based on the formulations of the optimization problem and the mesh adaptation

scheme, an optimization algorithm was constructed that uses the FEM for both the coupled analysis of the electrostatic and elastic deformation, and updating of the level set function.

(4) The effectiveness of the proposed method was verified using two models and four numerical examples. It was confirmed that the proposed method successfully obtains optimal electrostatic actuator configurations that have clear boundaries and that satisfy the design requirements.

Chapter 3

Structural optimization of electrostatic actuators considering driving force profiles

3.1 Introduction

In design problems for electrostatic actuators, the driving force profile is one of the primary engineering importance. In this chapter, an optimization method is developed that can handle real-world design problems in which a defined driving force profile must be obtained. Comb-drive electrostatic actuators, one of the most popular types of electrostatic actuators, due to their relatively large range of displacement, are used as numerical models.

Driving force profiles are determined by the shapes of the two electrodes. Using trial and error methods to obtain appropriate electrode shapes for comb-drive electrostatic actuators that provide a specific driving force profile is especially difficult because simultaneous consideration of multiple governing equations must be applied to the electrodes at various relative positions. Here, a multi-objective structural optimization method can play an important role in finding optimal electrode shapes for

such electrostatic actuators.

Based on the mesh adaptation scheme mentioned in Chapter 2, a level set-based shape optimization method for comb-drive electrostatic actuators is developed. This method allows large structural changes and maintains clear boundaries during the optimization. A multi-objective functional is formulated in order to obtain an optimal configuration that achieves a prescribed driving force profile. The sensitivity is obtained using the adjoint variable method. The electrostatic forces that occur on the structural boundaries are calculated using Maxwell's stress tensors, following the procedure described in Chapter 2. In the numerical examples, four comb-drive electrostatic actuator design examples are optimized and optimal configurations that achieve prescribed driving force profiles are presented.

3.2 Formulations

A comb-drive electrostatic actuator consists of two comb-shaped electrodes, as shown in Fig.3.1. One electrode is grounded; the other electrode has an electrical voltage applied. The grounded electrode moves toward the other electrode when a voltage is applied and the distance between the two electrodes is reduced. This movement is the basis for the use of comb-drive electrostatic devices as actuators.

One advantage of comb-drive electrostatic actuators is that their displacement range can be relatively large, given an appropriate design and length of the teeth of the two electrodes. The primary concern of engineers when designing comb-drive actuators is to define the driving force as a function of displacement, for example, to obtain a device that has a linear driving force profile. In the following, the optimization problem for comb-drive electrostatic actuators is formulated to achieve pre-defined driving force profiles.

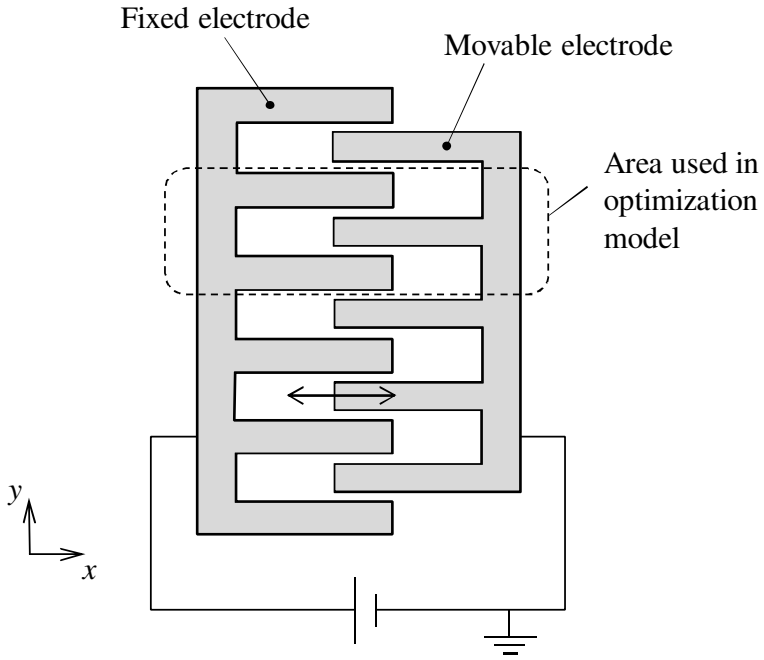

Figure 3.1: Comb-drive electrostatic actuator model

3.2.1 Governing equations

To optimize the design of comb-drive electrostatic actuators, the electrostatic field must be solved. Here, we note that the elastic field is not solved in this design problem, different from Chapter 2, since the driving force occur in the x-direction shown in Fig.3.1 and the deformations of the electrodes in this direction are very small.

A design domain, D, is set as shown in Fig.3.2. The fixed electrode, a material domain, is denoted Ω_D, and the movable electrode, also a material domain, is denoted Ω_M. Subscript D is used when denoting the fixed electrode Ω_D because the shape of the fixed electrode is the design target in the optimization problem that is discussed below. Both electrodes are made from a conductive material. The void domain, which is air, is denoted $D \setminus (\Omega_D \cup \Omega_M)$.

Comb-drive electrostatic actuators used in real-world applications have multiple pairs of teeth in order to create larger driving forces, as depicted in Fig.3.1. In this

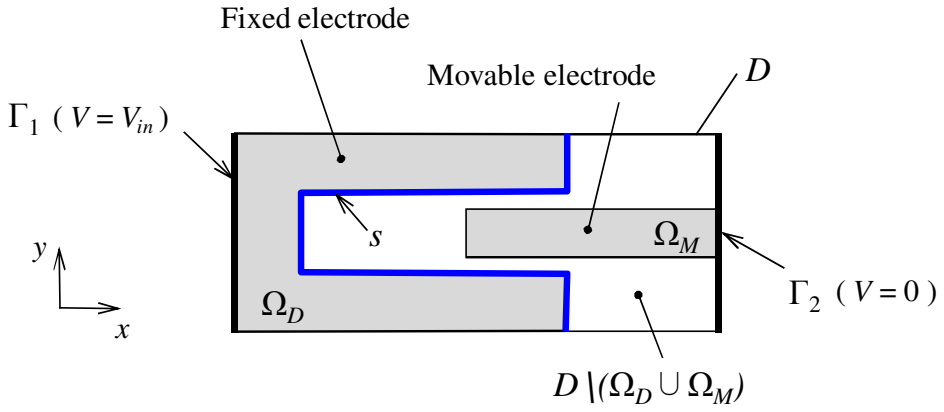

Figure 3.2: Design domain and boundary conditions of driving-force-profile-defined electrostatic actuator design problem

study, to simplify the optimization model, the design is confined to one set of teeth, as shown in Fig.3.2. The driving force of a design consisting of numerous sets of teeth can be obtained simply by multiplying the driving force of a single set by the number of sets.

It is assumed that there is no external electric charge or magnetic field. Extracting the relevant terms from Maxwell's equations, the governing equation is defined in the void domain as follows, using the vacuum permittivity, ϵ_0, and the electric potential, V.

$$\nabla \cdot (\epsilon_0 \nabla V) = 0 \qquad \text{in} \quad D \setminus (\Omega_D \cup \Omega_M) \tag{3.1}$$

This governing equation is extended to the entire fixed design domain, D, by introducing a sufficiently large fictitious permittivity to the material domain. That is, the governing equation is approximately solved in domain D, which is analogous to the ersatz material approach [32,34]. Hence, the governing equation is redefined as below.

$$\boldsymbol{\nabla} \cdot (\epsilon(\phi)\, \boldsymbol{\nabla} V) = 0 \qquad \text{in} \quad D, \tag{3.2}$$

where $\epsilon(\phi)$ is the extended permittivity, defined in the entire design domain D.

The Γ_1 boundary that is in contact with the fixed electrode is charged at electric potential V_{in} and the Γ_2 boundary in contact with the movable electrode is grounded, as shown in Fig.3.2. The boundary conditions are the following.

$$\begin{cases} V = \overline{V} & \text{on} \quad \Gamma_V \\ q = -(\epsilon(\phi)\nabla V) \cdot \boldsymbol{n}_D = 0 & \text{on} \quad \Gamma_q \end{cases} \tag{3.3}$$

where $\overline{V}$ is the prescribed electric potential V on boundary $\Gamma_V = \Gamma_1 \cup \Gamma_2$, $\Gamma_q = \partial D \backslash \Gamma_V$ has a Neumann boundary condition imposed, and $\boldsymbol{n}_D$ is the normal unit vector on boundary ∂D. The governing equation (3.2) is now rewritten in the weak form using the principle of virtual work.

$$\int_D \boldsymbol{\nabla} \hat{V} \cdot (\epsilon(\phi)\, \boldsymbol{\nabla} V)\, \mathrm{d}\Omega = 0, \tag{3.4}$$

where $\hat{V}$ is the test function.

Equation (3.4) is now rewritten using the electric field vector $\boldsymbol{E} = -\boldsymbol{\nabla} V$, as follows.

$$\int_D \hat{\boldsymbol{E}} \cdot (\epsilon(\phi)\boldsymbol{E})\, \mathrm{d}\Omega = 0 \tag{3.5}$$

3.2.2 Formulations for shape optimization

The aim is to develop an optimization method for comb-drive electrostatic actuators so that the optimal structure realizes a prescribed driving force profile. The shape of the fixed electrode is optimized in this chapter.

A target driving force, $\boldsymbol{T}^{j*}$, is defined at discrete positions of the movable electrode, defined as $j = 1, \cdots, m$, as shown in Fig.3.3, with m arbitrarily defined. The actual driving force at position j is calculated by taking the boundary integral of electrostatic force $\boldsymbol{t}^j$ on the boundary of the fixed electrode, denoted s. Electrostatic force $\boldsymbol{t}^j$ is calculated using Maxwell's stress tensors, following the procedure described

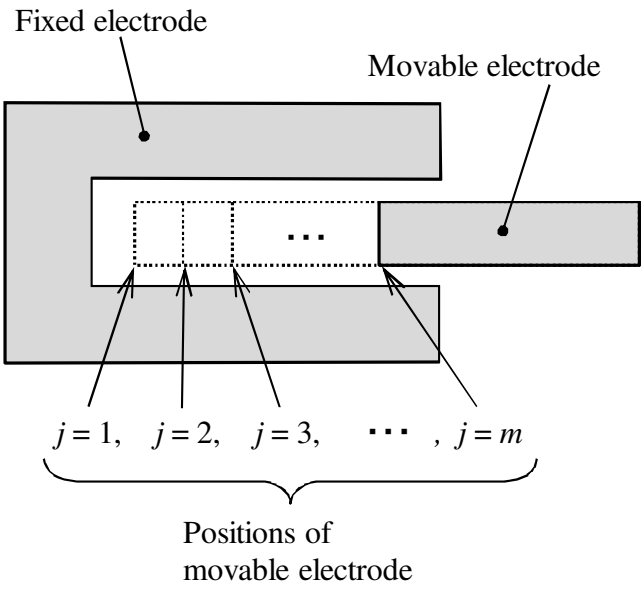

Figure 3.3: Movable electrode positions in comb-drive electrostatic actuator

in Section 2.2.2.

To achieve the target driving force at position j, the objective functional F^j is defined as the square of the differences between the target driving force $\boldsymbol{T}^{j*}$ and the actual driving force $\boldsymbol{T}^j$, as shown below, and this objective functional is to be minimized.

$$\inf_{\phi} \quad F^j = \{\boldsymbol{T}(\boldsymbol{\nabla} V^j, \phi) - \boldsymbol{T}^{j*}\}^2 \tag{3.6}$$

$$= \left(\int_s \boldsymbol{t}(\boldsymbol{\nabla} V^j) \cdot \boldsymbol{n}_s(\phi) \, \mathrm{d}\Gamma - \boldsymbol{T}^{j*} \right)^2, \tag{3.7}$$

where s is the boundary of an electrode in a comb drive electrostatic actuator and $\boldsymbol{n}_s$ is a unit normal vector on boundary s. Note that the definition of the objective functional that satisfies the design requirement is not unique.

To obtain a configuration that achieves a prescribed driving force profile, the optimization problem is formulated as a multi-objective optimization problem. A

multi-objective functional, F, is formulated using F^j, whose aim is to simultaneously minimize the differences between target driving forces and actual driving forces at j multiple positions. To obtain good convergence performance during the optimization process, the logarithm of the summation of the exponential of F^j is used for this objective functional. The optimization problem is now formulated as follows.

$$\inf_{\phi(\boldsymbol{x})} \qquad F[\,\boldsymbol{\nabla} V, \phi] = \ln\left\{\sum_{j=1}^{m} \exp\Big(w^j\, F^j\Big)\right\} \tag{3.8}$$

$$\text{subject to} \quad \boldsymbol{\nabla}\cdot(\epsilon(\phi)\,\boldsymbol{\nabla} V^j) = 0 \qquad \text{in} \quad D \tag{3.9}$$

$$V^j = \overline{V} \qquad \text{on} \quad \Gamma_V \tag{3.10}$$

$$q^j = -(\epsilon(\phi)\,\boldsymbol{\nabla} V^j)\cdot \boldsymbol{n}_D = 0 \qquad \text{on} \quad \Gamma_q \tag{3.11}$$

where w^j is a weighting function. This objective functional increases the influence of the sensitivity of the j-th position that has the largest difference between the target driving force and the actual driving force. The range of w^j must be appropriately defined, since values of w^j that are too large may cause memory overflow. The derivation of the sensitivity is explained in Section 3.3.1.

Note that a volume constraint is relatively unimportant in electrostatic actuator optimization problems, because these are MEMS scale devices and there is generally little need to reduce their volume. A volume constraint is therefore not employed. Additionally, to avoid situations where the two electrodes may stick together, a thin non-design domain that surrounds the fixed electrode is defined. By appropriately defining design and non-design domains, boundary limits are provided implicitly. This is one advantage of the proposed method, which uses an Eulerian coordinate system, compared to general shape optimization methods that use a Lagrangian coordinate system, hence cannot define non-design domains.

3.3 Numerical implementations

The flow of the optimization is shown in Fig.3.4. First, the initial value of the level

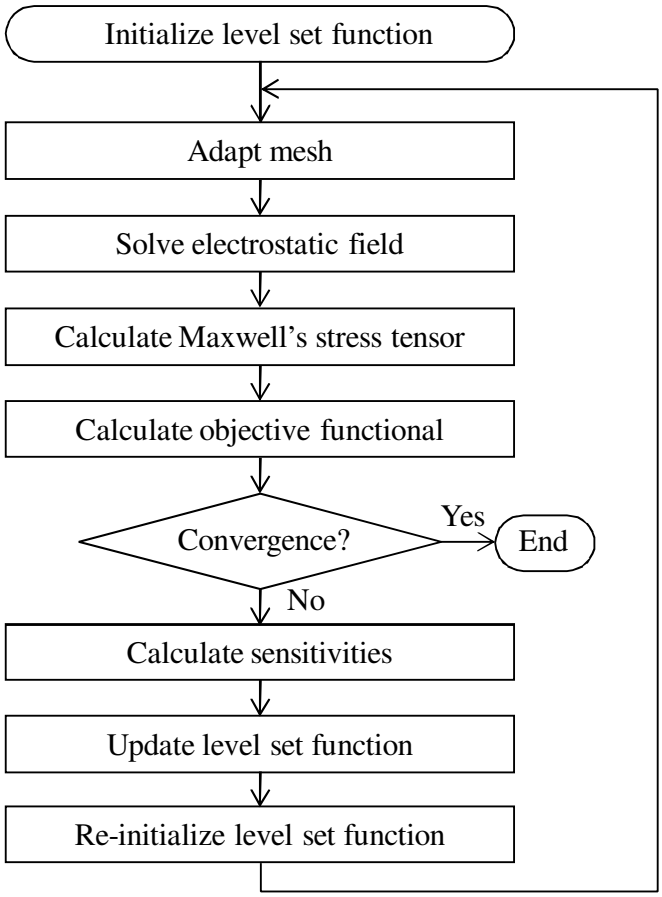

Figure 3.4: Flowchart of optimization procedure for the driving-force-profile-defined electrostatic actuator design problem

set function is set. The mesh adaptation is then carried out following the same procedure described in Section 2.3.1. In the third step, the electrostatic field is solved via the FEM. In the fourth step, the electrostatic forces acting on the nodes on the structural boundaries are determined by calculating Maxwell's stress tensors. The objective functional is then calculated and if it is converged, the optimization ends. If the optimization is not converged, the sensitivities are calculated and the level set

function is updated according to the sensitivities using Eq.(2.16). At the end of the optimization procedure, the level set function is re-initialized using the geometry-based re-initialization scheme discussed in Section 2.2.1, and the procedure returns to the second step. The value of the objective functional is thereby minimized and an optimal configuration is derived.

3.3.1 Sensitivity analysis

In this section, the design sensitivities are derived using the adjoint variable method. First, the boundary integral representing the driving force is replaced by the following domain integral by using level set function ϕ:

$$\boldsymbol{T}(\boldsymbol{\nabla} V^j, \phi) = \int_D \boldsymbol{t}(\boldsymbol{\nabla} V^j) \bar{\boldsymbol{\delta}}(\phi) \, \mathrm{d}D, \tag{3.12}$$

where $\bar{\boldsymbol{\delta}}(\phi)$ is defined using an approximated Heaviside function $H_a(\phi)$, as follows:

$$\bar{\boldsymbol{\delta}}(\phi) := \frac{\boldsymbol{\nabla}\phi}{|\boldsymbol{\nabla}\phi|} \frac{\mathrm{d}H_a(\phi)}{\mathrm{d}\,\phi}. \tag{3.13}$$

The Heaviside function is approximated as shown in (2.30).

Next, the Lagrangian $\overline{F}$ is defined as follows:

$$\begin{aligned} \overline{F} = \ln \left[\sum_{j=1}^{m} \exp \left\{ w^j \left(\int_D \boldsymbol{t}(\boldsymbol{\nabla} V^j) \bar{\boldsymbol{\delta}}(\phi) \, \mathrm{d}D - \boldsymbol{T}^{j*} \right)^2 \right\} \right] \\ + \sum_{j=1}^{m} \left[\int_D \hat{V}^j \, \boldsymbol{\nabla} \cdot (\epsilon(\phi) \, \boldsymbol{\nabla} V^j) \, \mathrm{d}D \right], \end{aligned} \tag{3.14}$$

where $\hat{V}^j$ represents the Lagrange multipliers. Furthermore, the adjoint system is

defined as follows:

$$\begin{cases} \boldsymbol{\nabla}\hat{V}^j = -2\dfrac{\epsilon_0}{\epsilon(\phi)}\left[\left\{\left(\boldsymbol{\nabla}V^j\right)\otimes\bar{\boldsymbol{\delta}}(\phi)\right\}^T\boldsymbol{a}_T^j\right] \\ \qquad\qquad +\dfrac{\epsilon_0}{\epsilon(\phi)}\left[\boldsymbol{a}_T^j\cdot\left\{\boldsymbol{I}\bar{\boldsymbol{\delta}}(\phi)\right\}\left(\boldsymbol{\nabla}V^j\right)\right] \qquad \text{in} \quad D \\ \hat{V}^j = 0 \qquad\qquad \text{on} \quad \Gamma_V \end{cases}$$

where coefficient vector $\boldsymbol{a}_T^j$ is defined in the following equation.

$$\boldsymbol{a}_T^j := \frac{2w^j(\boldsymbol{T}^j-\boldsymbol{T}^{j*})\exp\left\{w^j\ \left(\boldsymbol{T}^j-\boldsymbol{T}^{j*}\right)^2\right\}}{\sum_{j=1}^{m}\exp\left\{w^j\ \left(\boldsymbol{T}^j-\boldsymbol{T}^{j*}\right)^2\right\}} \tag{3.15}$$

Thus, the following design sensitivity is obtained as follows:

$$\begin{aligned}\delta\overline{F} = \sum_{j=1}^{m}\int_D\Bigg\{&\left(\frac{2w^jW^j(\boldsymbol{T}^j-\boldsymbol{T}^{j*})}{\sum W^j}\right)\cdot\left(\boldsymbol{t}(\boldsymbol{\nabla}V^j)\frac{\partial\bar{\boldsymbol{\delta}}(\phi)}{\partial\phi}\right) \\ &-\left(\boldsymbol{\nabla}\hat{V}^j\right)\cdot\left(\frac{\partial\epsilon(\phi)}{\partial\phi}\boldsymbol{\nabla}V^j\right)\Bigg\}\delta\phi\ \mathrm{d}D.\end{aligned} \tag{3.16}$$

Details concerning the derivation of the sensitivity are provided in the Appendix. Note that the first and second terms respectively represent the effects of geometrical changes and the effects of changes in Maxwell's stress tensor. Therefore, the first term can be neglected when changes in the shape are insignificant. Also note that the adjoint problem does not have to be solved, although the optimization problem is not a self-adjoint problem. That is, the design sensitivity is represented by the gradient of the Lagrange multiplier $\boldsymbol{\nabla}\hat{V}$, and the adjoint system is constructed using the gradient of the Lagrange multiplier $\boldsymbol{\nabla}\hat{V}$, since the objective functional is defined by using the domain integral of a function of a gradient of the state variable V.

3.4 Numerical examples

The suitability of the proposed optimization method is verified using a comb-drive electrostatic actuator model. The model considers a single set of teeth, as shown in Fig.3.5, although the fixed and movable electrodes in actual devices have numerous sets of teeth deployed in a line.

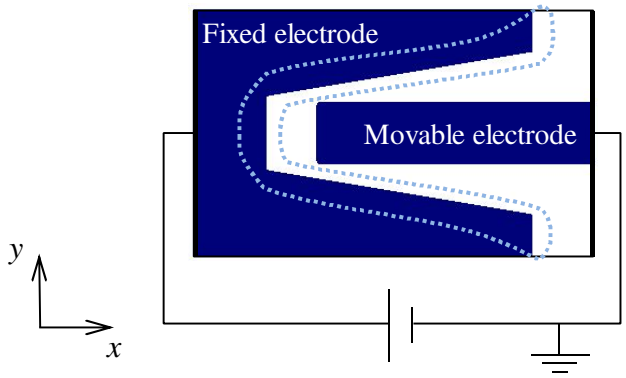

Figure 3.5: Comb-drive electrostatic actuator model used in the numerical examples

Only the shape of the fixed electrode is optimized in the following examples, because it was determined that this approach is reasonable from the standpoint of calculation cost and the manufacturability of the obtained comb-drive designs, and structures that achieve prescribed driving forces were obtained. The driving force is calculated by taking the boundary integral of the electrostatic forces on the surface of the fixed electrode along the length shown enclosed by the dotted line in Fig.3.5.

The size of the design domain is set as $650 \times 400\mu$m, with a thickness of 10μm. The initial configuration of the electrodes is shown in Fig.3.6. An external voltage, $V_{in} = 100$V, is applied to the fixed electrode and the movable electrode is grounded. Concerning the weighting function w^j in Eq.(3.8), a value of 1 is assigned to all w^j $(j = 1, \cdots, m)$ so that identical weighting is applied to F^j.

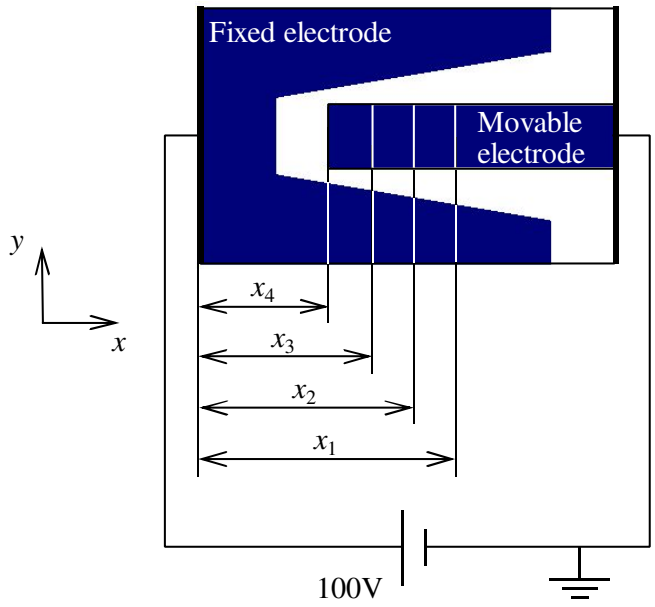

Figure 3.6: Initial configuration and electrode positions in driving-force-profile-defined electrostatic actuator design problem

3.4.1 Electrostatic actuator designs with linear driving force profile

A driving force profile with a linear response rate is often a desirable performance goal for electrostatic actuators. In the first and second examples that follow, actuator designs that provide a linear relationship between driving force and electrode position are to be obtained. The x positions of the movable electrode in the first example are $x_1 = 400\mu$m, $x_2 = 333\mu$m, $x_3 = 267\mu$m, and $x_4 = 200\mu$m, with respect to leftmost edge of the fixed electrode, as shown in Fig.3.6.

Plots of the target driving force, initial driving force, and driving force for the optimal configuration are shown in Fig.3.7(a). It is confirmed that the driving force profile of the optimal configuration is accurately aligned with the target driving force profile. The optimal configuration is shown in Fig.3.8(a), and clear boundaries were obtained. The dotted lines in Fig.3.8(a) illustrate the four different x positions of the

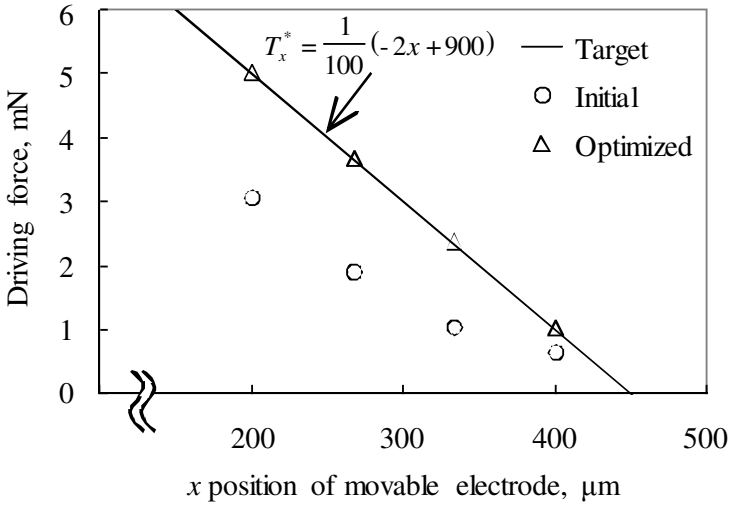

(a) Example 1

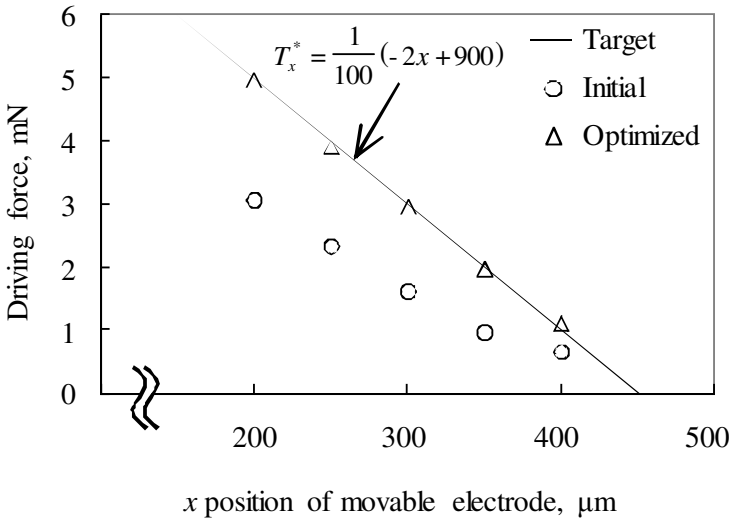

(b) Example 2

Figure 3.7: Driving force profiles of Examples 1 and 2

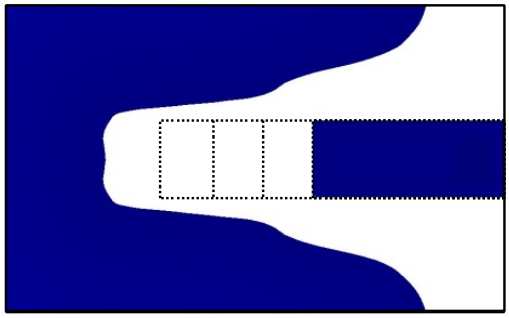

(a) Example 1

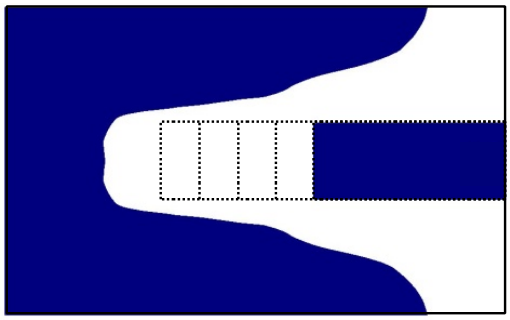

(b) Example 2

Figure 3.8: Optimal configurations of Examples 1 and 2

movable electrode. Figure 3.9(a) shows the optimization history.

The second example also targets a linear driving force profile but uses five different movable-electrode positions in the model. The electrode positions in this example are $x_1 = 400\mu$m, $x_2 = 350\mu$m, $x_3 = 300\mu$m, $x_4 = 250\mu$m, $x_5 = 200\mu$m, relative to the leftmost edge of the fixed electrode. The driving force profiles and optimal configuration are shown in Fig.3.7(b) and Fig.3.8(b), respectively. The driving forces obtained by the optimal configuration are congruent with the target driving force profile. Figure 3.9(b) shows the optimization history.

3.4.2 Electrostatic actuator designs with sharp initial rise driving force profile

Most actuators used in engineering applications have a driving force profile that provides a weak initial rise. Since driving force profiles that include a sharp initial rise are advantageous in industrial applications, the proposed optimization method is applied to the design of an actuator with this type of force profile.

In the third example, a target driving force profile that includes a sharp initial rise is set. As shown in Fig.3.10(a), the rate of increase in driving force is greatest when the electrodes are furthest apart, and this rate decreases as the electrodes approach. The model in this example uses three positions for the movable electrode: $x_1 = 390\mu$m, $x_2 = 300\mu$m, and $x_3 = 200\mu$m. The driving force profile of the optimal configuration is shown in Fig.3.10(a). It is confirmed that the optimal configuration obtains a driving force profile that matches the target driving force profile. The optimal configuration is shown in Fig.3.11(a), and Fig.3.12(a) shows the optimization history.

The fourth example also targets a sharp initial rise driving force profile but uses a model with four different x positions of the movable electrode: $x_1 = 390\mu$m, $x_2 = 333\mu$m, $x_3 = 267\mu$m, and $x_4 = 200\mu$m. It is confirmed that the driving force profile provided by the optimal configuration again matches the target driving force

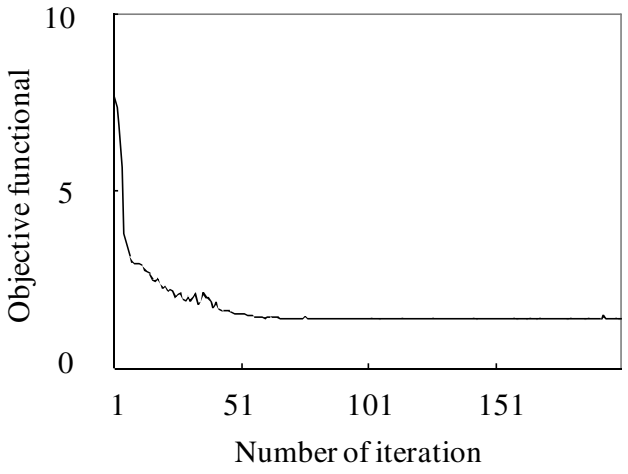

(a) Example 1

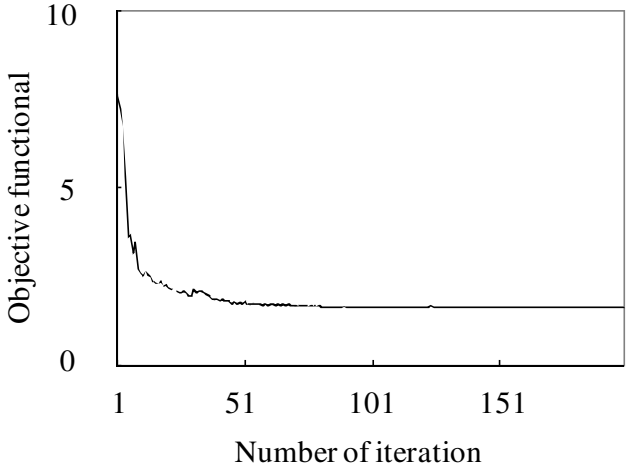

(b) Example 2

Figure 3.9: History of objective functional of Examples 1 and 2

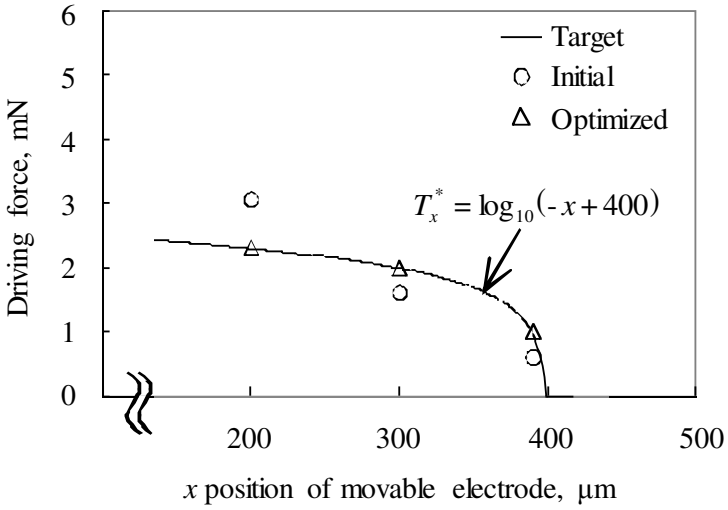

(a) Example 3

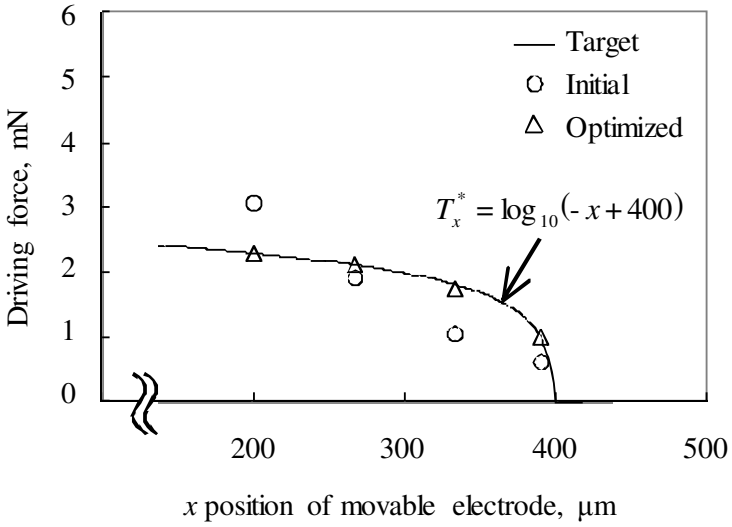

(b) Example 4

Figure 3.10: Driving force profiles of Examples 3 and 4

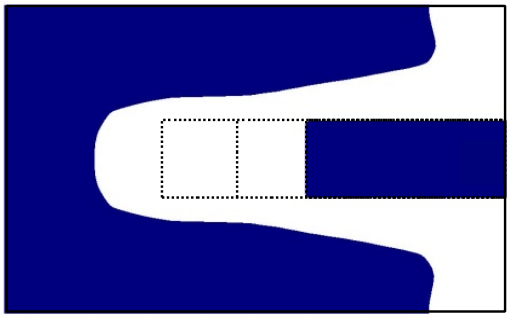

(a) Example 3

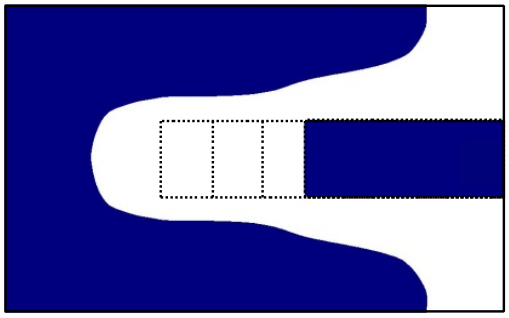

(b) Example 4

Figure 3.11: Optimal configurations of Examples 3 and 4

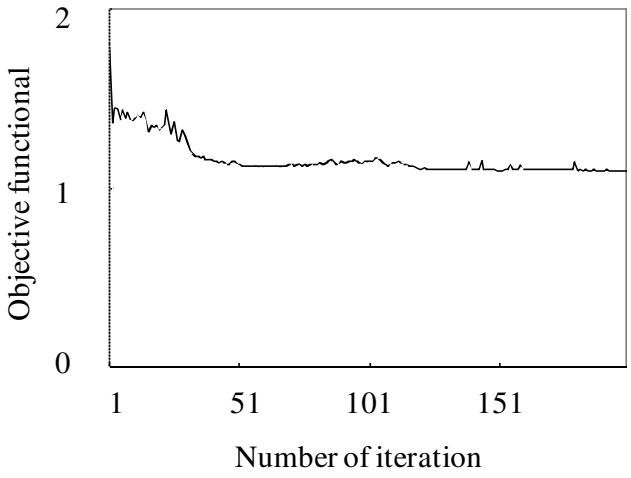

(a) Example 3

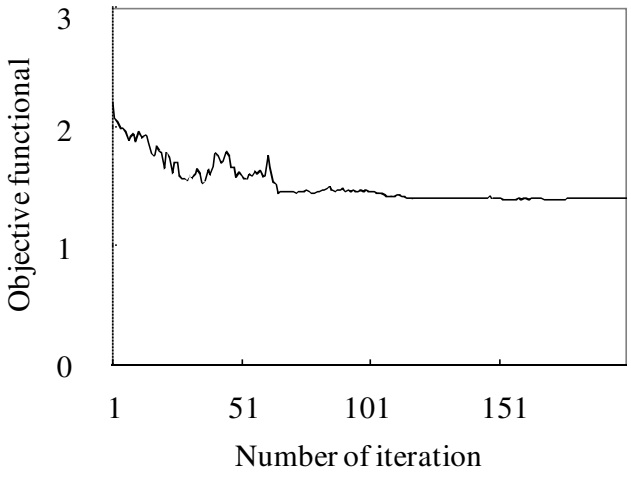

(b) Example 4

Figure 3.12: History of objective functional of Examples 3 and 4

profile, as shown in Fig.3.10(b). The optimal configuration is shown in Fig.3.11(b), and Fig.3.12(b) shows the optimization history.

3.5 Conclusion

A level set-based shape optimization method for comb-drive electrostatic actuators was proposed. The proposed method enables actuator designs that achieve prescribed driving force profiles, which is highly beneficial in an engineering sense. This research obtained the following results:

(1) Design requirements for comb-drive electrostatic actuators were clarified and an optimization problem using a multi-objective functional was formulated for the design of an electrostatic comb-drive type of actuator that achieves a prescribed driving force profile.

(2) The sensitivities were derived using the adjoint variable method and the objective functional did not require solving the adjoint fields during the optimization.

(3) Based on the formulation of the optimization problem and the developed mesh adaptation scheme, an optimization algorithm for solving the electrostatic field and calculating the sensitivities was constructed.

(4) The suitability of the proposed method was demonstrated in four numerical examples. Each optimal configuration achieved the target driving force profile, and all had clear structural boundaries. It was confirmed that the proposed method enables the design of electrostatic actuators that incorporate desirable driving force profiles and obtains optimal configurations that are free from grayscale areas.

Chapter 4

Structural optimization of mechanical resonators

4.1 Introduction

Mechanical resonators are designed to be flexible to achieve a specified motion as a sensor. In this chapter, an optimization method for mechanical resonators is developed using a level set-based topology optimization method. The topology optimization problem is formulated to obtain an optimal configuration that is valid in an engineering sense and that proactively utilizes the dynamic instability of the structure. First, the level set-based topology optimization method is explained, the design requirements for mechanical resonators are clarified, the objective functional that satisfies the design requirements is defined, and the topology optimization problem is formulated based on the objective functional. Next, a topology optimization algorithm is developed using the FEM for the analysis of the structural and adjoint problems and for updating the level set function. Finally, three-dimensional numerical examples are provided and the effectiveness of the proposed method is verified.

4.2 Formulations

4.2.1 Topology optimization based on a level set method

The area occupied by material is termed the material domain, Ω, and the structural optimization of Ω is considered. An objective functional, F, is defined as the summation of an area integral in the material domain and a boundary integral at boundary Γ. The structural optimization problem is formulated as

$$\inf_{\Omega} \qquad F = \int_{\Omega} f_1(\boldsymbol{x}) \, \mathrm{d}\Omega + \int_{\Gamma} f_2(\boldsymbol{x}) \, \mathrm{d}\Gamma, \tag{4.1}$$

where $f_1(\boldsymbol{x})$ and $f_2(\boldsymbol{x})$ are the distribution functions inside material domains and at boundaries, respectively, that define the objective functional. In topology optimization, a fixed design domain D that allows the existence of material domain Ω is introduced, and the shape of the material domain inside the fixed design domain is expressed using the following characteristic function.

$$\chi(\boldsymbol{x}) = \begin{cases} 1 & \text{if} \quad \forall \boldsymbol{x} \in \Omega \\ 0 & \text{if} \quad \forall \boldsymbol{x} \in D \setminus \Omega \end{cases} \tag{4.2}$$

The structural optimization problem (4.1) is formulated as a topology optimization problem using the characteristic function $\chi(\boldsymbol{x})$ and the fixed design domain D as below.

$$\inf_{\chi(\boldsymbol{x})} \qquad F = \int_{D} f_1(\boldsymbol{x})\chi(\boldsymbol{x}) \, \mathrm{d}\Omega + \int_{\Gamma} f_2(\boldsymbol{x}) \, \mathrm{d}\Gamma \tag{4.3}$$

Next, a level set function, $\phi(\boldsymbol{x})$ is introduced. $\phi(\boldsymbol{x})$ is positive inside the material domain Ω, negative in the void domain $D \setminus \Omega$, and zero on boundary Γ between the material and void domains. This level set function, however, does not have the characteristic of a signed distance function, which was maintained for the level set

function used in Chapter 2. The boundary expression that incorporates this level set function ensures that optimal structures are free of grayscales and have boundaries that are expressed as a continuous function [1].

The topology optimization problem (4.3) is now replaced with the following formula that incorporates the level set function $\phi(\boldsymbol{x})$.

$$\inf_{\phi(\boldsymbol{x})} \qquad F = \int_D f_1(\boldsymbol{x})\chi_\phi(\phi)\ \mathrm{d}\Omega + \int_{\Gamma(\phi)} f_2(\boldsymbol{x})\ \mathrm{d}\Gamma, \tag{4.4}$$

where $\chi_\phi(\boldsymbol{x})$ is a characteristic function defined using the level set function, as follows.

$$\chi_\phi(\boldsymbol{x}) = \begin{cases} 1 & \text{if } \ \phi\,(\boldsymbol{x}) \geq 0 \\ 0 & \text{if } \ \phi\,(\boldsymbol{x}) < 0 \end{cases} \tag{4.5}$$

Next, the regularization of the optimization problem is discussed. The characteristic function defined above allows the existence of discontinuities with infinitesimal intervals everywhere in the fixed design domain because it is a function for which only integrability is guaranteed. As a result, topology optimization problems are usually ill-posed problems [90], and the design space therefore must be relaxed in some way. In the homogenization design method, it is assumed that there is a certain microstructure inside the fixed design domain and the shape parameter of this microstructure is used as the design variable in the optimization. The material density distribution of the macrostructure is then obtained using the homogenization method.

In the density method, on the other hand, the optimization is performed using a characteristic function whose definition is made less strict by using a material density function that allows intermediate values. Neither of these methods obtains optimal structures that have clear boundaries; the optimal configurations contain grayscales that represent regions of intermediate density between those of the material and void domains. Obtaining optimal structures that are useful in an engineering sense is therefore difficult with these methods. Furthermore, in structural design problems

that proactively use structural instabilities to obtain desired performance, grayscales cannot be removed when using the above methods because such intermediate density areas are most often included in the optimal structures in order to amplify vibrations.

On the other hand, when using a level set method to represent structural shapes, neither of the design-space regularization methods mentioned above can be applied, since the design variables are different. To circumvent this problem, a method has been proposed that introduces a new term regularization term to the objective functional [33]. In this method, a regularization term, R, that represents the gradient of the level set function, is added to objective functional F, and a new objective functional, F_R, is then formulated, as follows.

$$\inf_{\phi(\boldsymbol{x})} \quad F_R = F + R \tag{4.6}$$

$$R := \frac{1}{2}\tau \int_D -\text{sign}(\phi(\boldsymbol{x}))\phi_{,ii} \, \mathrm{d}\Omega \tag{4.7}$$

$$\text{subject to} \quad -1 \leq \phi(\boldsymbol{x}) \leq 1, \tag{4.8}$$

where $\tau > 0$ is a regularization coefficient. The double subscript i complies with summation conventions and represents a partial differential by the coordinate component. A constraint is introduced and applied to the upper and lower limits of the level set function. Thus, R only has non-zero values near the structural boundaries and regularization in this neighborhood is maintained at a certain level.

As a result, the geometric complexity of the optimal structure can be adjusted by changing the value of the regularization coefficient, τ. Optimal structures in which structurally complex portions are suppressed can be obtained when τ is relatively large, and optimal structures that include relatively complex partial structures can be obtained when τ is relatively small. Note that the level set function can accept such a constraint because it represents the boundaries of material domains via the zero iso-surface and it has an arbitrary property, namely that the profile of the level set function is underspecified for any specific structure.

4.2.2 Topology optimization method

The necessary optimality conditions (KKT, Karush-Kuhn-Tucker conditions) of the solution of the optimization problem formulated in (4.6) are as follows.

$$F'_R = 0\,, \tag{4.9}$$

where F'_R is the limit of the ratio of the variation of objective functional F_R to the volume of a spherical void when a spherical void of radius ϵ appears. The definition of F'_R, the topological derivative [91, 92], is shown below.

$$F_R + \delta F_R = F_R + V_\epsilon F'_R + o\left(V_\epsilon\right) \quad as \quad \epsilon \to 0\,, \tag{4.10}$$

where V_ϵ is the volume of infinitesimal spherical voids that are removed. Directly finding a level set function that satisfies the KKT conditions is very difficult, so the optimization problem is replaced by a problem of solving a time evolution equation. An appropriate initial structure is given and a fictitious time, t, is introduced, assuming that changes in the level set function are proportional to the gradient of the objective functional. The time evolution equation, including a proportional constant, K, is expressed as

$$\frac{\partial \phi(\boldsymbol{x}, t)}{\partial t} = -K F'_R\,. \tag{4.11}$$

The boundary conditions applied to the level set function are $\phi(\boldsymbol{x}, t) = 1$ on boundary ∂D_{mat} for the material domain, $\phi(\boldsymbol{x}, t) = -1$ on boundary ∂D_{void} for the void domain, and $\frac{\partial \phi(\boldsymbol{x}, t)}{\partial n} = 0$ on boundary ∂D_n, which permits a material or void domain outside the fixed design domain, for example, on a boundary where a displacement constraint is applied. The system of time evolution equations applied to the level set function

is as follows.

$$\begin{cases} \frac{\partial \phi(\boldsymbol{x},t)}{\partial t} = -K(F' - \tau\phi_{,ii}) & \text{in } D \\ \phi(\boldsymbol{x},t) = 1 & \text{on } \partial D_{mat} \\ \phi(\boldsymbol{x},t) = -1 & \text{on } \partial D_{void} \\ \frac{\partial \phi(\boldsymbol{x},t)}{\partial n} = 0 & \text{on } \partial D_n \end{cases} \tag{4.12}$$

Equation (4.12) is discretized using the difference method in the time direction, and using the FEM for space and the level set function values, so that solution candidates for the optimization are obtained by updating the level set function.

4.2.3 Formulation of optimization problem

First, the design requirements for mechanical resonators are clarified and an objective functional is formulated to obtain an optimal structure that satisfies the design requirements. A mechanical resonator can detect displacement in a certain direction by measuring displacements at a detection point as geometrical deformations of its structure occur in response to inertia forces caused by acceleration in a certain direction (Fig.4.1). The most important performance metric for mechanical resonators is

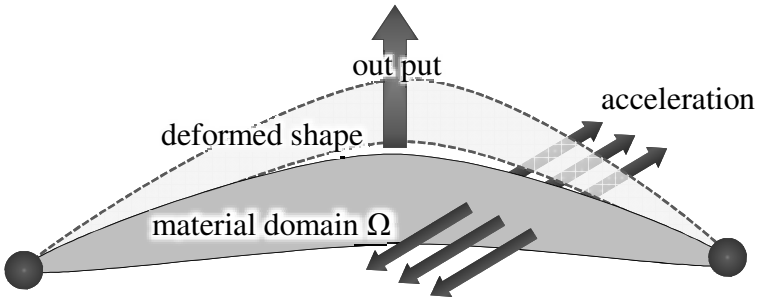

Figure 4.1: Concept of mechanical resonator

displacement in a certain direction at the detection location when a certain accelera-

tion is applied to the device, and this displacement must be maximized to maximize detection sensitivity. An additional requirement is to ensure sufficient structural stiffness so that the resonator maintains its shape when reaction forces act upon it, e.g., from the detection device in which the resonator is mounted.

A model is used to formulate an objective functional used to find an optimal structure that satisfies both of the above requirements (Fig.4.2). It is assumed that

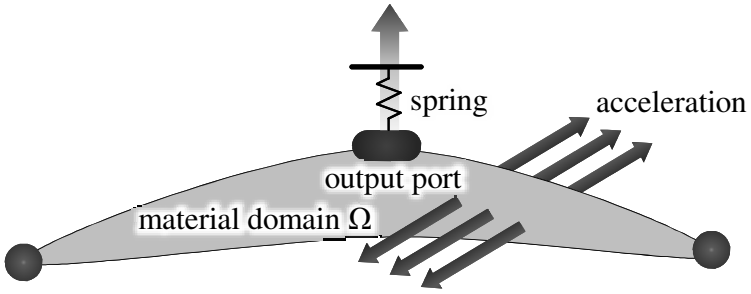

Figure 4.2: Model of mechanical resonator

a harmonic acceleration with angular frequency ω is applied to the material domain Ω, which is filled with a homogeneous isotropic linearly elastic solid, and that the material domain Ω vibrates harmonically in response to inertial forces and a steady state is achieved. The acceleration detection function of a mechanical resonator can be regarded as a function that transforms an externally applied acceleration to kinetic energy in the detection direction at the detection location. Therefore, the kinetic energy in the detection direction at the detection location should be maximized in order to maximize the performance of the resonator.

To formulate the stiffness, a method [27,93] in which a desired stiffness is assigned by the placement of a spring is used. The reaction force of this spring at the detection location occurs in the direction opposite that of the external motion, and stiffness against the reaction force of the spring is thereby obtained. The magnitude of this stiffness can be changed by changing the strength of the spring. The structural

optimization problem is now formulated as below, based on the formulation of the objective functional.

$$\inf_{\Omega} \quad F = -\frac{1}{2}\int_{\Omega_{out}} \rho\omega^2 (e_i u_i(\boldsymbol{x},\omega))^2 \, \mathrm{d}\Omega \tag{4.13}$$

$$\text{s.t.} \quad C_{ijkl}u_{k,lj}(\boldsymbol{x},\omega) + \rho\omega^2 u_i(\boldsymbol{x},\omega) = -\rho a_i \ \text{ in } \ \Omega \tag{4.14}$$

$$u_i(\boldsymbol{x},\omega) = \overline{u_i} \qquad \text{on } \ \Gamma_{\mathrm{u}} \tag{4.15}$$

$$t_i(\boldsymbol{x},\omega) = \overline{t_i} \qquad \text{on } \ \Gamma_{\mathrm{t}} \tag{4.16}$$

$$t_i(\boldsymbol{x},\omega) = k_{ij}u_j(\boldsymbol{x},\omega) \qquad \text{on } \ \Gamma_{\mathrm{k}}, \tag{4.17}$$

where e_i is the unit vector in the detection direction, u_i is the complex amplitude of displacement, t_i is the complex amplitude of the traction, C_{ijkl} is the constant elasticity tensor, k_{ij} is the constant spring tensor, ρ is the mass density, a_i is the complex amplitude of the acceleration given, and $\overline{u_i}$ and $\overline{t_i}$ are the known functions.

Here, the maximization problem is replaced with a minimization problem by using a new objective functional in which the kinetic energy term in the detection area Ω_{out} is preceded by a minus sign. An infinitesimal strain is assumed in these formulations, but the structural deformation of a mechanical resonator obtained by the optimization might be associated with large deformations. Considerations of large deformations during the design process increases the difficulty of the design problem and the calculation cost. Furthermore, desired performances in optimal structures were achieved in past research, to a qualitative degree, by optimizations considering the flexibility of the structures and assuming infinitesimal deformations [93]. For the above reasons, the optimization discussed in this chapter is executed under an assumption of infinitesimal deformations. An optimization method for dealing with large deformations will be discussed in Chapter 5.

4.3 Numerical implementations

4.3.1 Topology optimization algorithm

The structural optimization algorithm (Fig.4.3) for mechanical resonators is constructed here based on the topology optimization method proposed by Yamada et al [33]. The analysis domain, fixed design domain, and boundary conditions for a

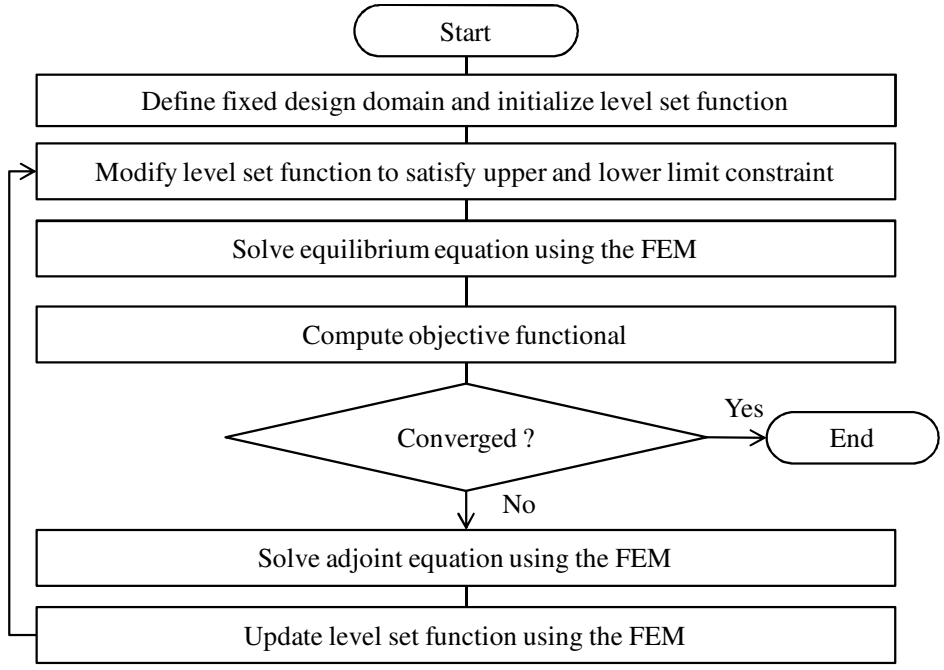

Figure 4.3: Flowchart of optimization procedure for mechanical resonator design problem

mechanical resonator are defined and the level set function that gives an appropriate initial structure is set. The level set function is then modified to satisfy the upper and lower limit constraints. The structure does not change when the level set function is modified unless the sign of the level set function is changed, because the structural boundary is represented by the zero iso-surface. Next, the static elastic field is solved using the FEM and the objective functional is computed. If the objective functional is

converged, the optimization is terminated and an optimal structure is obtained. If the objective functional is not converged, the adjoint field is solved using the FEM. The topological derivative is then calculated and the level set function is updated using a reaction-diffusion equation. The procedure then returns to the second step in which the level set function is modified. Optimal solutions are obtained in this manner. Note that the topological derivative used in this research is strictly derived [91, 92] and that in previous research, the approximation formula ignored the effect of the boundary condition for holes [33].

4.3.2 Sensitivity analysis

The sensitivity is analyzed using the adjoint variable method. The adjoint field v_i is assumed to be the solution of the following boundary value problem.

$$C_{ijkl}v_{k,lj}(\boldsymbol{x},\omega) + \rho\omega^2 v_i(\boldsymbol{x},\omega) = \begin{cases} -\rho\omega^2 u_i e_i & \text{in} \quad \Omega_{out} \\ 0 & \text{in} \quad \Omega \setminus \Omega_{out} \end{cases} \tag{4.18}$$

$$v_i(\boldsymbol{x},\omega) = 0 \qquad \text{on} \quad \Gamma_{\mathrm{u}} \tag{4.19}$$

$$q_i(\boldsymbol{x},\omega) = 0 \qquad \text{on} \quad \Gamma_{\mathrm{t}} \tag{4.20}$$

$$q_i(\boldsymbol{x},\omega) = k_{ij}v_j(\boldsymbol{x},\omega) \qquad \text{on} \quad \Gamma_{\mathrm{k}} \tag{4.21}$$

Here, δF is expressed as follows.

$$\begin{aligned} \delta F =& \frac{4}{3}\pi\epsilon^3 \Bigg\{ \frac{3(1-\nu)}{2(1+\nu)(7-5\nu)} \Bigg[-\frac{(1-14\nu+15\nu^2)E}{(1-2\nu)^2}\delta_{ij}\delta_{kl} \\ & + 5E(\delta_{ik}\delta_{jl}+\delta_{il}\delta_{jk}) \Bigg] v^0_{i,j}u^0_{k,l} - \rho\omega^2 v^0_i u^0_i \Bigg\} + o(\epsilon^3)\,, \end{aligned} \tag{4.22}$$

where E is the Young's modulus, ν is the Poisson's ratio, δ_{ij} is Kronecker delta, and u^0_i, v^0_i, $u^0_{k,l}$, and $v^0_{i,j}$ are respectively the values of u_i, v_i, $u_{k,l}$, and $v_{i,j}$ at the center of the sphere before removing the infinitesimal spheres. From Eq.(4.10), the

topological derivative is defined as follows.

$$F' = \lim_{\epsilon \to 0} \frac{\delta \overline{F}}{\frac{4}{3}\pi\epsilon^3} = v^0_{i,j} A_{ijkl} u^0_{k,l} - \rho\omega^2 v^0_i u^0_i, \tag{4.23}$$

where A_{ijkl} is given as

$$A_{ijkl} = \frac{3(1-\nu)}{2(1+\nu)(7-5\nu)} \Bigg[- \frac{(1-14\nu+15\nu^2)E}{(1-2\nu)^2} \delta_{ij}\delta_{kl} + 5E(\delta_{ik}\delta_{jl} + \delta_{il}\delta_{jk}) \Bigg]. \tag{4.24}$$

The topological derivative F' includes the displacement and the displacement gradient of the static elastic problem, and the displacement and the displacement gradient of the adjoint problem, and is analyzed using the FEM.

4.4 Numerical examples of mechanical resonator designs

The effectiveness of the proposed method is now verified through numerical examples. The analysis domain and the boundary conditions for the mechanical resonator design problems are shown in Fig.4.4. The analysis domain is a rectangular volume $200\mu\text{m} \times 400\mu\text{m} \times 40\mu\text{m}$ and the output port and the outer frame are set as non-design domains. The fixed design domain is represented by the non-colored space in Fig.4.4. The outer circumference of the outer frame is fixed. The angular frequency of the acceleration given from outside is 100 rad/s. The direction of the acceleration is denoted x_1 and the output direction e_i is denoted x_3.

A design problem for a mechanical resonator is considered as the transformation of acceleration in the in-plane direction to movement in the out-of-plane direction. Isoparametric hexahedral primary elements with eight vertices are used for the analysis of the static elastic and adjoint fields and for updating the level set function.

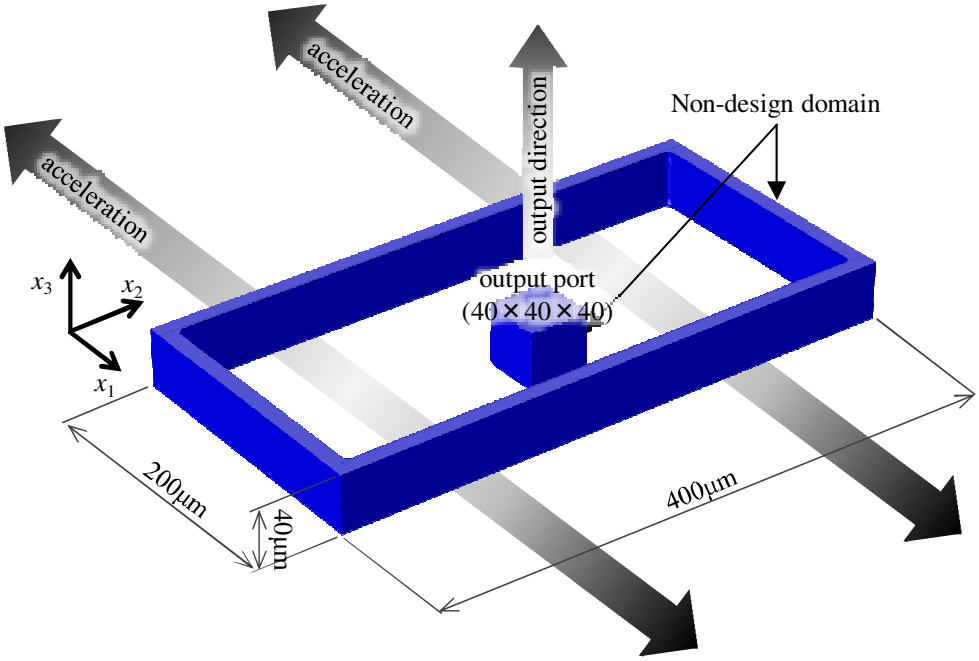

Figure 4.4: Analysis model of mechanical resonator design problem

The element size is set as 5μm. The isotropic linearly elastic solid material of the structure is silicon nitride film, with Young's modulus 320GPa, Poisson's ratio 0.263, and mass density 3270kg/m^3. The material property of the void domain is approximated using the ersatz material approach [32]. The ratio of the Young's modulus of the void domain to that of the material domain, and the ratio of the mass density of void domain to that of the material domain, are both 1×10^{-3}. The reaction-diffusion equation (4.12) is normalized using a characteristic length of 200μm.

The optimized structure is shown in Figs.4.5 and 4.6. The value of the regularization coefficient τ is 5×10^{-3} in Case 1, 1×10^{-4} in Case 2, and 1×10^{-5} in Case 3. All obtained structures have clear boundaries. As demonstrated in Figs.4.5 and 4.6, the structural complexity can be modified by using different values of τ. In particular, the proposed method can provide optimal structures that have a general degree of structural complexity that is specified by design engineers, which is especially useful

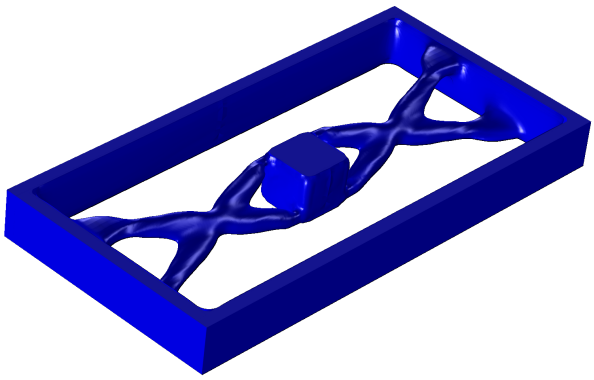

(a) Case 1

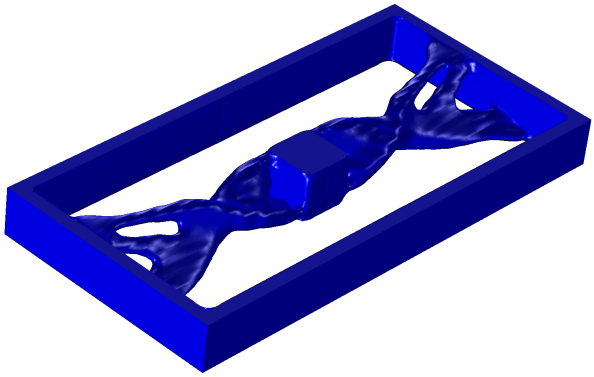

(b) Case 2

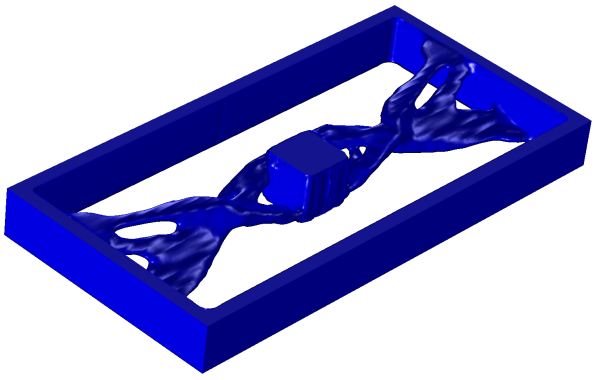

(c) Case 3

Figure 4.5: Bird's-eye views of optimal configurations of mechanical resonator design problem

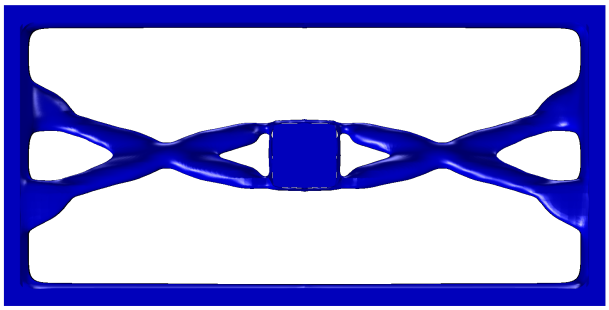

(a) Case 1

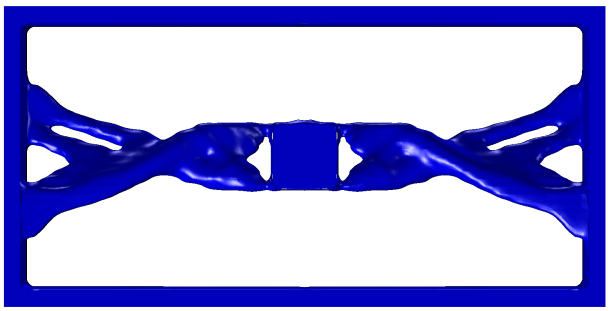

(b) Case 2

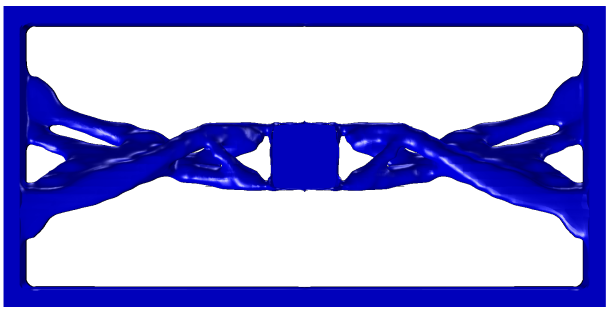

(c) Case 3

Figure 4.6: Bottom views of optimal configurations of mechanical resonator design problem

from the point of view of manufacturability.

The deformation modes are shown in Fig.4.7. The optimal structure mainly deforms torsionally in the detection direction, using the asymmetrical nature of the structure with respect to the x_3 direction. It is concluded that the proposed method is effective since the obtained structures satisfy the required performances. Note that optimizations that use the homogenization method or the density method usually encounter the problem of grayscales [49]. In contrast, the proposed method that uses a level set method can provide structures that satisfy the desired performances and are free of grayscales.

4.5 Conclusion

A topology optimization method based on a level set method was developed for mechanical resonators. The research achieved the following:

(1) Design requirements for mechanical resonators were clarified and an objective functional was derived based on the concept of kinetic energy maximization. The optimization problem was formulated using the derived objective functional and the stiffness of the structure was represented with a spring.

(2) A topology optimization algorithm for mechanical resonator design problems was developed. The FEM was used for analyses of the static elastic and adjoint fields and for updating the level set function, based on the formulation of the optimization problem.

(3) The effectiveness of the proposed method was verified through numerical examples. The proposed method provided optimal mechanical resonator structures that satisfy the required performances and the boundaries were clear and smooth. Furthermore, the structural complexity of the optimal structures of the mechanical resonators was controlled by appropriately setting a regularization

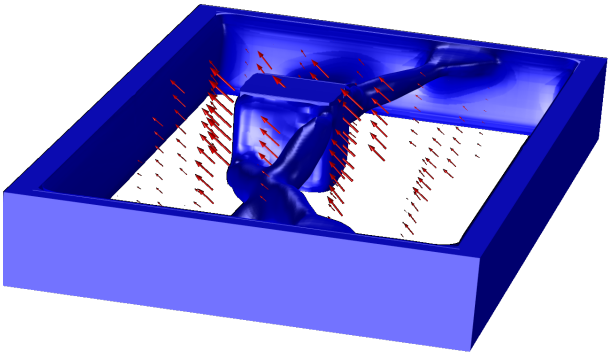

(a) Case 1

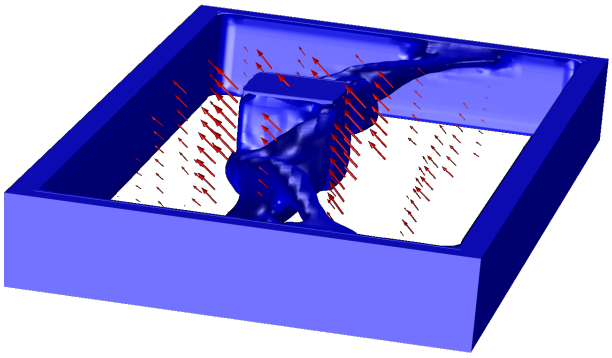

(b) Case 2

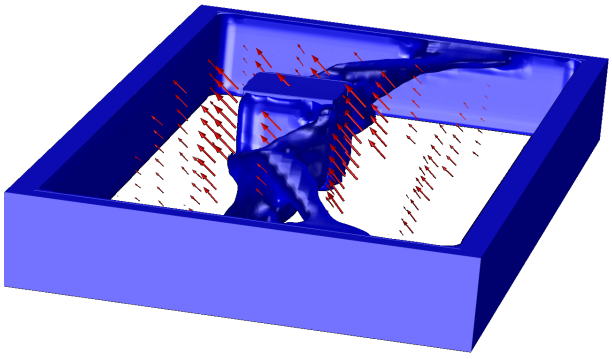

(c) Case 3

Figure 4.7: Deformed configurations of mechanical resonator design problem

coefficient.

Chapter 5

Structural optimization of compliant mechanisms using geometrically nonlinear analysis

5.1 Introduction

In this chapter, a topology optimization method that can consider large deformations is developed. Compliant mechanisms [27, 30–33, 94–99] are used as examples to examine the effectiveness of the proposed optimization method.

Compliant mechanisms are structures that utilize their flexibility to achieve designed functions and they undergo large deformations in certain areas because functions similar to those of joints and springs in rigid-link structures are enabled by deformations alone. Compliant mechanisms have fewer mechanical parts than conventional mechanisms, do not need lubrication, are nearly silent in operation, and can often be miniaturized. Compliant mechanisms are therefore widely used in a variety of products.

Large deformations require nonlinear analysis during design optimization. The FEM usually includes an assumption that displacements are small, and it cannot

easily carry out nonlinear analysis. A Moving Particle Semi-implicit (MPS) method [68, 75, 76], a particle method that discretizes the governing equations, is therefore used for the nonlinear analysis in this study. Such methods can avoid the problem of mesh distortion, often encountered in the FEM analyses when dealing with large deformations, and they allow geometrically nonlinear analyses to be effectively carried out. Another difficulty when dealing with large deformations in topology optimization is the problem of grayscales. Large deformations require flexible structures and the expression of such structures in conventional topology optimization methods usually requires the material to have intermediate material properties that appear as grayscales. In this study, a level set-based topology optimization method is adopted for the optimization so that clear boundaries can be obtained in the optimized configurations. Numerical examples are presented to demonstrate the effectiveness of the proposed method and the results are compared with those obtained from an optimization method that uses the FEM-based analysis. Toward the end of this chapter, the differences between the optimized configurations provided by the proposed method and those of the FEM-based method are discussed, to highlight the importance of considering geometric nonlinearity when optimizing compliant mechanisms that undergo large deformations.

5.2 Formulations

5.2.1 Compliant mechanism problems considering geometric nonlinearity

The formulations for compliant mechanisms considering geometric nonlinearity are now discussed. Compliant mechanisms have the following features: (1) flexibility to achieve designed motions without joints, (2) sufficient stiffness to maintain structural shape, and (3) sufficient stiffness against reactive forces from a workpiece.

An example of a model for a complaint mechanism design problem is shown in Fig.5.1. The displacement is maximized at boundary Γ_{out} where a dummy vector,

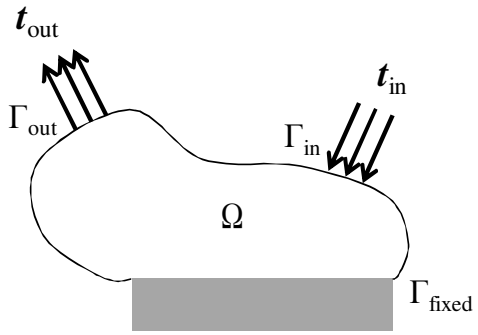

Figure 5.1: Model of compliant mechanism design problem

$\boldsymbol{t}_{\text{out}}$, is set, as surface force $\boldsymbol{t}_{\text{in}}$ is applied at boundary Γ_{in}. Ω represents the material domain. Here, the displacement maximization problem is replaced with a flexibility maximization problem using the mutual mean compliance, l_1, as the objective functional, as follows.

$$l_1\left(\boldsymbol{u}_{\text{in}}\right) = \int_{\Gamma_{\text{out}}} \boldsymbol{t}_{\text{out}} \cdot \boldsymbol{u}_{\text{in}} \mathrm{d}\Gamma \tag{5.1}$$

In this research, consideration of both flexibility and stiffness of a design structure is enabled by an approach proposed by Sigmund [27], the same approach as that used in Chapter 4.

A compliant mechanism must have a sufficient degree of stiffness against deformation in the direction of $\boldsymbol{t}_{\text{out}}$ (Fig.5.1). To model the stiffness of the structure in response to traction force $\boldsymbol{t}_{\text{out}}$, a spring, k_{in}, is set at boundary Γ_{in}, as shown in Fig.5.2(a), Case A. In addition, the compliant mechanism needs sufficient stiffness to maintain structural integrity when a traction force is applied at Γ_{in}, as shown in Fig.5.2(b), Case B. A spring k_{out} is set at Γ_{out} to model this stiffness. The optimiza-

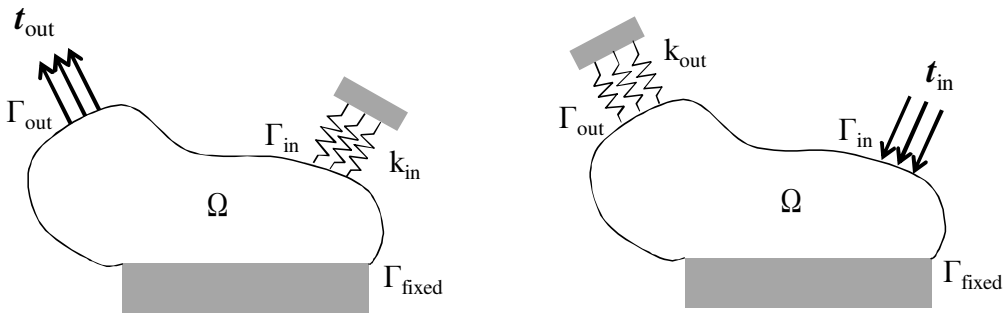

(a) Case A (b) Case B

Figure 5.2: Boundary conditions of compliant mechanism design problem

tion problem is now formulated as follows.

$$\inf_{\Omega} \qquad F = -l_1(\boldsymbol{u}_{\text{in}}) \tag{5.2}$$

$$\text{subject to} \quad I(\boldsymbol{u}_{\text{in}}, \boldsymbol{v}) = l_2(\boldsymbol{v}) - a(\boldsymbol{u}_{\text{in}}, \boldsymbol{v}) = 0 \tag{5.3}$$

$$\text{for} \quad \forall \boldsymbol{v} \in U \quad \boldsymbol{u}_{\text{in}} \in U$$

$$G = \int_{\Omega} \mathrm{d}\Omega - V_{\max} \leq 0, \tag{5.4}$$

where G is the volume constraint. The expressions used in the above formula are defined as follows.

$$l_2(\boldsymbol{v}) = \int_{\Gamma_{\text{in}}} \boldsymbol{t}_{\text{in}} \cdot \boldsymbol{v} \mathrm{d}\Gamma \tag{5.5}$$

$$a(\boldsymbol{u}_{\text{in}}, \boldsymbol{v}) = \int_{\Omega} \boldsymbol{\epsilon}(\boldsymbol{u}_{\text{in}}) : \boldsymbol{E} : \boldsymbol{\epsilon}(\boldsymbol{v}) \, \mathrm{d}\Omega + \int_{\Gamma_{\text{out}}} (k_{\text{out}} \boldsymbol{u}_{\text{in}}) \cdot \boldsymbol{v} \mathrm{d}\Gamma \tag{5.6}$$

Here, $\boldsymbol{\epsilon}$ represents the strain tensors, $\boldsymbol{E}$ is the elastic tensor, $\boldsymbol{u}$ represents the state variables, $\boldsymbol{v}$ is an arbitrary function, and U is the displacement function space, formulated as follows, with D representing the fixed design domain.

$$U = \{\boldsymbol{v} = v_{\text{i}} \boldsymbol{e}_{\text{i}} : \; v_{\text{i}} \in H^1(D) \text{ with } \boldsymbol{v} = 0 \text{ on } \Gamma_{\text{fixed}}\} \tag{5.7}$$

In Eq.(5.3), the residual of $l_2(\boldsymbol{v}) - a(\boldsymbol{u}_{\text{in}}, \boldsymbol{v}) = 0$ is used, since, in nonlinear problems, an iteration method using tangent stiffness matrices is adopted to solve the equilibrium equations.

5.2.2 Level set-based topology optimization and sensitivity analysis

A level set-based topology optimization method can provide clear optimal configurations because the structural boundaries are represented by an iso-surface of the level set function. Using the level set function ϕ and characteristic function χ_ϕ, as described in Section 4.2.1, the objective functional and constraints are redefined in the following formulation.

$$\inf_{\chi_\phi} \quad F(\boldsymbol{u}_{\text{in}}) = -l_1(\boldsymbol{u}_{\text{in}}) \tag{5.8}$$

$$\begin{aligned} \text{subject to} \quad I(\boldsymbol{u}_{\text{in}}, \boldsymbol{v}, \chi_\phi(\phi)) &= \int_{\Gamma_{\text{in}}} \boldsymbol{t}_{\text{in}} \cdot \boldsymbol{v} \mathrm{d}\Gamma - \int_D \boldsymbol{\epsilon}(\boldsymbol{u}_{\text{in}}) : \boldsymbol{E} : \boldsymbol{\epsilon}(\boldsymbol{v}) \chi_\phi(\phi) \mathrm{d}\Omega \\ &\quad - \int_{\Gamma_{\text{out}}} (k_{\text{out}} \boldsymbol{u}_{\text{in}}) \cdot \boldsymbol{v} \mathrm{d}\Gamma \\ &= 0 \end{aligned} \tag{5.9}$$

$$G(\chi_\phi(\phi)) = \int_\Omega \chi_\phi(\phi) \mathrm{d}\Omega - V_{\max} \leq 0 \tag{5.10}$$

Next, as discussed in Section 4.2.1, a regularization term, R, is introduced to the objective functional to regularize the optimization problem. The objective functional is now re-written using this regularization term.

$$F_R(\boldsymbol{u}_{\text{in}}, \phi) = -l_1(\boldsymbol{u}_{\text{in}}) + R(\phi), \tag{5.11}$$

where $R(\phi)$ is formulated as

$$R(\phi) = \int_D \frac{1}{2} \tau \mid \nabla \phi \mid^2 \mathrm{d}\Omega. \tag{5.12}$$

The regularization used here is the so-called Tikhonov regularization method, and by changing the value of parameter τ, the relative weight of the objective functional and the regularization term can be adjusted. Furthermore, the geometric complexity of optimized structures can be adjusted by setting appropriate values for τ. The Lagrangian is formulated using a Lagrange multiplier, as follows.

$$\bar{F_R} = -l_1\left(\boldsymbol{u}_{\text{in}}\right) + I\left(\boldsymbol{u}_{\text{in}}, \boldsymbol{v}, \chi_\phi\left(\phi\right)\right) + \lambda G(\chi_\phi\left(\phi\right)) + R\left(\phi\right) \tag{5.13}$$

The KKT conditions are obtained as below.

$$\left\langle \frac{\mathrm{d}\bar{F_R}}{\mathrm{d}\phi}, \delta\phi \right\rangle = 0, \;\; I\left(\boldsymbol{u}_{\text{in}}, \boldsymbol{v}, \chi_\phi\left(\phi\right)\right) = 0, \;\; \lambda G(\chi_\phi\left(\phi\right)) = 0, \;\; \lambda \geq 0, \;\; G(\chi_\phi\left(\phi\right)) \leq 0, \tag{5.14}$$

where $\left\langle \frac{\mathrm{d}\bar{F_R}}{\mathrm{d}\phi}, \delta\phi \right\rangle$ is the Fréchet derivative of the Lagrangian $\bar{F_R}$.
Now, the sensitivity of Lagrangian $\bar{F_R}$ with respect to the design variable ϕ is obtained as follows.

$$\begin{aligned}
\left\langle \frac{\mathrm{d}\bar{F_R}}{\mathrm{d}\phi}, \delta\phi \right\rangle = &- \left\langle \frac{\partial l_1\left(\boldsymbol{u}_{\text{in}}\right)}{\partial \boldsymbol{u}_{\text{in}}}, \delta\boldsymbol{u}_{\text{in}} \right\rangle \left\langle \frac{\partial \boldsymbol{u}_{\text{in}}}{\partial \phi}, \delta\phi \right\rangle \\
&+ \left\langle \frac{\partial I\left(\boldsymbol{u}_{\text{in}}, \boldsymbol{v}, \chi_\phi\left(\phi\right)\right)}{\partial \boldsymbol{u}_{\text{in}}}, \delta\boldsymbol{u}_{\text{in}} \right\rangle \left\langle \frac{\partial \boldsymbol{u}_{\text{in}}}{\partial \phi}, \delta\phi \right\rangle \\
&+ \left\langle \frac{\partial I\left(\boldsymbol{u}_{\text{in}}, \boldsymbol{v}, \chi_\phi\left(\phi\right)\right)}{\partial \phi}, \delta\phi \right\rangle \\
&+ \lambda \left\langle \frac{\partial G(\chi_\phi\left(\phi\right))}{\partial \phi}, \delta\phi \right\rangle \\
&+ \left\langle \frac{\partial R\left(\phi\right)}{\partial \phi}, \delta\phi \right\rangle
\end{aligned} \tag{5.15}$$

From the above formula, the adjoint problem is defined as

$$\left\langle \frac{\partial l_1\left(\boldsymbol{u}_{\text{in}}\right)}{\partial \boldsymbol{u}_{\text{in}}}, \delta\boldsymbol{u}_{\text{in}} \right\rangle = \left\langle \frac{\partial I\left(\boldsymbol{u}_{\text{in}}, \boldsymbol{v}, \chi_\phi\left(\phi\right)\right)}{\partial \boldsymbol{u}_{\text{in}}}, \delta\boldsymbol{u}_{\text{in}} \right\rangle, \tag{5.16}$$

and the sensitivity is obtained as

$$\left\langle \frac{\mathrm{d}\bar{F}_R}{\mathrm{d}\phi}, \delta\phi \right\rangle = \left\langle \frac{\partial \left[I\left(\boldsymbol{u}_{\mathrm{in}}, \boldsymbol{v}, \chi_\phi\left(\phi\right)\right) + \lambda G(\chi_\phi\left(\phi\right)) + R\left(\phi\right)\right]}{\partial\phi}, \delta\phi \right\rangle. \tag{5.17}$$

5.2.3 Time evolution equation

The level set function ϕ that satisfies the KKT-conditions (5.14) is nearly impossible to obtain directly, so an initial value for the level set function is set and a fictitious time, t, is introduced for updating the level set function to obtain a candidate solution of the optimization. The optimization problem is replaced by a time evolution problem of the level set function, as in Section 4.2.2, as follows.

$$\frac{\partial\phi}{\partial t} = -K\left(\phi\right)\frac{\mathrm{d}\bar{F}_R}{\mathrm{d}\phi} \tag{5.18}$$

The level set function is updated in proportion to the gradient of the regularized Lagrangian, and $K(\phi) > 0$ is a constant of proportionality. Substituting Eq.(5.13) into Eq.(5.18), the following is obtained.

$$\begin{cases} \dfrac{\partial\phi}{\partial t} = -K\left(\phi\right)\dfrac{\mathrm{d}\bar{F}_R}{\mathrm{d}\phi} = -K\left(\phi\right)\left\{\dfrac{\mathrm{d}\left[I\left(\boldsymbol{u}_{\mathrm{in}}, \boldsymbol{v}, \chi_\phi\left(\phi\right)\right) + \lambda G(\chi_\phi\left(\phi\right))\right]}{\mathrm{d}\phi} - \tau\nabla^2\phi\right\} \\ \dfrac{\partial\phi}{\partial n} = 0 \qquad \text{on} \quad \partial D \setminus \partial D_N \\ \phi = 1 \qquad \text{on} \quad \partial D_N \end{cases} \tag{5.19}$$

A Dirichlet boundary condition is imposed at non-design boundaries ∂D_N and a Neumann boundary condition is imposed at the design boundaries. The first term of Eq.(5.19) is in the form of a reaction-diffusion equation. The reaction term $\frac{\mathrm{d}\bar{F}}{\mathrm{d}\phi} = \frac{\mathrm{d}\left[I\left(\boldsymbol{u}_{\mathrm{in}}, \boldsymbol{v}, \chi_\phi(\phi)\right) + \lambda G(\chi_\phi(\phi))\right]}{\mathrm{d}\phi}$ is equivalent to the topological derivative [99–102] defined as

$$\mathrm{d}_t\bar{F} = -\frac{\partial\bar{F}\left(\chi_\phi\right)}{\partial\chi_\phi} = \lim_{\epsilon\to 0}\frac{\bar{F}\left(\Omega_{\epsilon,\boldsymbol{x}}\right) - \bar{F}\left(\Omega\right)}{\mid B_{\epsilon,\boldsymbol{x}} \cap \Omega \mid}, \tag{5.20}$$

where $B_{\epsilon,\boldsymbol{x}}$ is a sphere with radius ϵ and center $\boldsymbol{x}$, and $\Omega_{\epsilon,\boldsymbol{x}}$ is a material domain that includes $B_{\epsilon,\boldsymbol{x}}$. Equation (5.19) is now rewritten as below.

$$\begin{cases} \dfrac{\partial \phi}{\partial t} = -K\left(\phi\right)\left(-\boldsymbol{\epsilon}\left(\boldsymbol{u}_{\mathrm{in}}\right) : \boldsymbol{E}\chi_{\phi} : \boldsymbol{\epsilon}\left(\boldsymbol{v}\right) - \lambda - \tau\nabla^2\phi\right) \\ \dfrac{\partial \phi}{\partial n} = 0 \quad \text{on} \quad \partial D \setminus \partial D_N \\ \phi = 1 \quad \text{on} \quad \partial D_N \end{cases} \tag{5.21}$$

An optimized configuration is obtained by solving Eq.(5.21).

5.3 Numerical implementations

The flowchart of the proposed optimization method is shown in Fig.5.3. First, the level set function $\phi\left(x\right)$ is initialized, the material domain is defined using $\phi\left(x\right)$, and particles are populated. In the second step, the state and adjoint equations are solved using the MPS method. Next, the objective functional is calculated and the procedure terminates if the objective functional is converged. If the objective functional is not converged, the sensitivities are calculated with respect to the objective functional in the fourth step. In the fifth step, the level set function is updated using the sensitivities and the procedure returns to the second step. An optimized configuration is obtained by iterating the above procedure until the objective functional is converged. The details of the MPS method used to solve state and adjoint state equations are explained in the next section.

5.3.1 Moving particle semi-implicit method

The details of the MPS method [68, 75, 76] are briefly explained below. The particle at the center, illustrated in Fig.5.4, interacts with other particles existing within the interaction radius, r_{e}, and a weighting function, w, is defined as shown in Eq.(5.22).

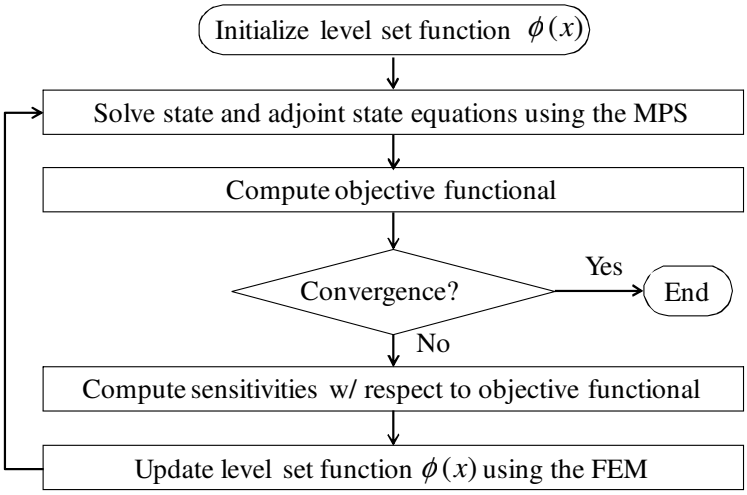

Figure 5.3: Flowchart of optimization procedure for compliant mechanism design problem

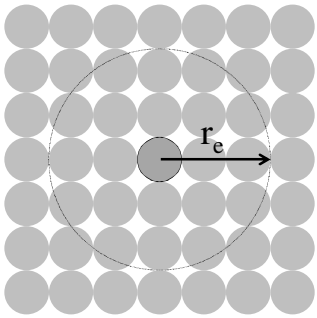

Figure 5.4: Interaction radius in MPS method

$$\mathrm{w}\left(r\right) = \begin{cases} \dfrac{r_\mathrm{e}}{r} - 1 & (0 \leq r < r_\mathrm{e}) \\ 0 & (r_\mathrm{e} \leq r) \end{cases} \tag{5.22}$$

Next, the relative coordinates, $\boldsymbol{r}$, of the two particles, i, j, are defined.

$$\boldsymbol{r}_\mathrm{ij} = \boldsymbol{r}_\mathrm{j} - \boldsymbol{r}_\mathrm{i} \tag{5.23}$$

The initial coordinates, $\boldsymbol{r}_\mathrm{ij}^0$, shown in Fig.5.5(a), are now defined.

$$\boldsymbol{r}_\mathrm{ij}^0 = \boldsymbol{r}_\mathrm{j}^0 - \boldsymbol{r}_\mathrm{i}^0 \tag{5.24}$$

The relative displacement, $\boldsymbol{u}_\mathrm{ij}$, shown in Fig.5.5(b), is defined using Eq.(5.23) and (5.24). $\boldsymbol{R}$ is the rotation matrix and is defined in Eq.(5.26).

$$\boldsymbol{u}_\mathrm{ij} = \boldsymbol{r}_\mathrm{ij} - \boldsymbol{R}\boldsymbol{r}_\mathrm{ij}^0 \tag{5.25}$$

$$\boldsymbol{R} = \begin{bmatrix} \cos\theta_\mathrm{ij} & -\sin\theta_\mathrm{ij} \\ \sin\theta_\mathrm{ij} & \cos\theta_\mathrm{ij} \end{bmatrix} \tag{5.26}$$

Stress $\boldsymbol{\sigma}$ is defined as shown in Eq.(5.27) and (5.28).

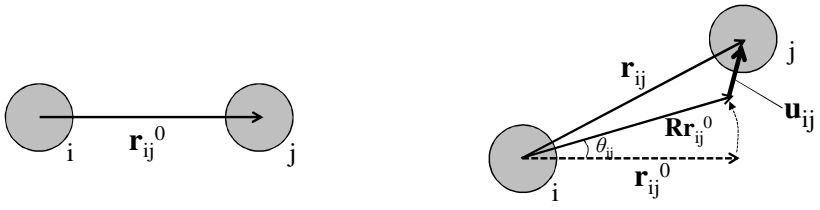

(a) Initial configuration (b) New configuration

Figure 5.5: Relative Coordinates $\boldsymbol{r}_\mathrm{ij}^0$ and $\boldsymbol{r}_\mathrm{ij}$ and relative displacement $\boldsymbol{u}_\mathrm{ij}$ in MPS method

$$\boldsymbol{\sigma}_{\mathrm{ij}}^{\mathrm{n}} = 2\mu\boldsymbol{\epsilon}_{\mathrm{ij}}^{\mathrm{n}} = 2\mu\frac{\boldsymbol{u}_{\mathrm{ij}}^{\mathrm{n}}}{\mid \boldsymbol{r}_{\mathrm{ij}}^{0} \mid} \tag{5.27}$$

$$\boldsymbol{\sigma}_{\mathrm{ij}}^{\mathrm{s}} = 2\mu\boldsymbol{\epsilon}_{\mathrm{ij}}^{\mathrm{s}} = 2\mu\frac{\boldsymbol{u}_{\mathrm{ij}}^{\mathrm{s}}}{\mid \boldsymbol{r}_{\mathrm{ij}}^{0} \mid}, \tag{5.28}$$

where μ is the Lamé constant, and superscripts s and n represent the components in the $\boldsymbol{r}_{\mathrm{ij}}$ direction and normal to it, respectively.

The acceleration of particles consists of the normal stress term (subscript n), shear stress term (subscript s), and pressure term (subscript p).

$$\left(\frac{\partial \boldsymbol{v}_{\mathrm{i}}}{\partial t}\right) = \left(\frac{\partial \boldsymbol{v}_{\mathrm{i}}}{\partial t}\right)_{\mathrm{n}} + \left(\frac{\partial \boldsymbol{v}_{\mathrm{i}}}{\partial t}\right)_{\mathrm{s}} + \left(\frac{\partial \boldsymbol{v}_{\mathrm{i}}}{\partial t}\right)_{\mathrm{p}} \tag{5.29}$$

Each term is derived using the following equations that incorporate the divergence model of the MPS method.

$$\rho_{\mathrm{i}}\left(\frac{\partial \boldsymbol{v}_{\mathrm{i}}}{\partial t}\right)_{\mathrm{n}} = \frac{\mathrm{d}}{\mathrm{n}^{0}}\sum_{\mathrm{j}\neq\mathrm{i}}\frac{2\boldsymbol{\sigma}_{\mathrm{ij}}^{\mathrm{n}}}{\mid \boldsymbol{r}_{\mathrm{ij}}^{0} \mid}\mathrm{w}\left(\mid \boldsymbol{r}_{\mathrm{ij}}^{0} \mid\right) \tag{5.30}$$

$$\rho_{\mathrm{i}}\left(\frac{\partial \boldsymbol{v}_{\mathrm{i}}}{\partial t}\right)_{\mathrm{s}} = \frac{\mathrm{d}}{\mathrm{n}^{0}}\sum_{\mathrm{j}\neq\mathrm{i}}\frac{2\boldsymbol{\sigma}_{\mathrm{ij}}^{\mathrm{s}}}{\mid \boldsymbol{r}_{\mathrm{ij}}^{0} \mid}\mathrm{w}\left(\mid \boldsymbol{r}_{\mathrm{ij}}^{0} \mid\right) \tag{5.31}$$

$$\rho_{\mathrm{i}}\left(\frac{\partial \boldsymbol{v}_{\mathrm{i}}}{\partial t}\right)_{\mathrm{p}} = \frac{\mathrm{d}}{\mathrm{n}^{0}0}\sum_{\mathrm{j}\neq\mathrm{i}}\frac{2\mathrm{p}_{\mathrm{ij}}\boldsymbol{r}_{\mathrm{ij}}}{\mid \boldsymbol{r}_{\mathrm{ij}}^{0} \mid\mid \boldsymbol{r}_{\mathrm{ij}} \mid}\mathrm{w}\left(\mid \boldsymbol{r}_{\mathrm{ij}}^{0} \mid\right), \tag{5.32}$$

where ρ is the density, d is the number of spatial dimensions, n^{0} is the particle number density, and p is the pressure.

5.4 Numerical examples

5.4.1 Compliant mechanism design 1

The effectiveness of the proposed method for the optimization of compliant mechanisms is verified with two numerical examples, using the proposed level set-based topology optimization method that includes the MPS method. The design domain for the first numerical example (Example 1) is a rectangle 1.70m × 0.35m, with two fixed segments located on the bottom boundary (Fig.5.6). The problem considered

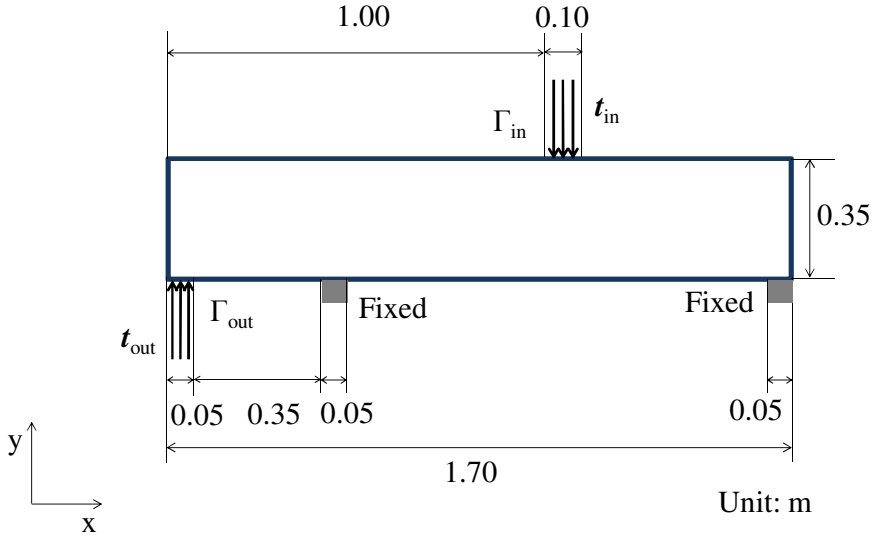

Figure 5.6: Design domain and boundary conditions of Example 1

is to maximize the displacement in the direction of $\boldsymbol{t}_{\text{out}}$ (in the $+y$ direction) when traction $\boldsymbol{t}_{\text{in}}$ is given. To ensure the stiffness of the structure against the action and reaction forces, springs $\boldsymbol{k}_{\text{in}}$ and $\boldsymbol{k}_{\text{out}}$ are set at the positions where $\boldsymbol{t}_{\text{in}}$ and $\boldsymbol{t}_{\text{out}}$ are applied, respectively, following the method explained in Section 5.2.1. A Dirichlet boundary condition is applied to the fixed boundary segments and to the boundaries where tractions occur, and the other boundaries have a Neumann boundary condition imposed. The material is assumed to be a soft silicone rubber with a Young's modu-

Table 5.1: Analysis methods, traction forces, spring constants, and regularization coefficients of Example 1

	Example 1A	Example 1B	Example 1C
Analysis method	MPS method	FEM	MPS method
$\boldsymbol{t}_{\text{in}}$ [N]	1.0×10^4	1.0×10^4	1.0×10^0
$\boldsymbol{t}_{\text{out}}$ [N]	1.0×10^4	1.0×10^4	1.0×10^0
$\boldsymbol{k}_{\text{in}}$ [N]	2.0×10^7	2.0×10^7	2.0×10^7
$\boldsymbol{k}_{\text{out}}$ [N]	2.0×10^7	2.0×10^7	2.0×10^7
τ	1.0×10^{-4}	1.0×10^{-4}	1.0×10^{-4}

lus of 1×10^6Pa and Poisson's ratio equal to 0.33. The design domain is discretized into 4-node isoparametric bilinear square elements 1.0×10^{-2}m in size for the level set function field, and the displacement field is replaced with 170×35 particles, with the particle distance set to 1.0×10^{-2}m, which is the same as the FEM element size. A volume constraint of 40% is used.

A load of 1.0×10^4N is applied at $\boldsymbol{t}_{\text{in}}$ to generate the large deformation (Example 1A). For comparison, the same model is optimized using a topology optimization combined with linear FEM analysis for the analysis of the displacement field (Example 1B). In addition, an optimization problem with a small applied load is provided (Example 1C), since it is believed that nonlinear analysis using the MPS method yields the same solutions as linear analysis when the displacement is very small. The τ parameter, the value of which affects the degree of geometric complexity, is set to 1.0×10^{-4} for all examples. The conditions mentioned above are listed in Table 5.1.

The optimization results are shown in Fig.5.7. The optimal configurations of Example 1A, solved using the MPS method that considers geometric nonlinearity, and Example 1B that used linear FEM analysis, are noticeably different. The optimal configuration of Example 1C, solved using the MPS method under small loading, is almost the same as that of Example 1B. These results are consistent with the assumption of small deformations in the FEM linear analysis.

The deformations that occur for different loading applied at $\boldsymbol{t}_{\text{in}}$ for Examples 1A and 1B are shown in Figs.5.8 and 5.9. In Example 1A, the deformation of the output

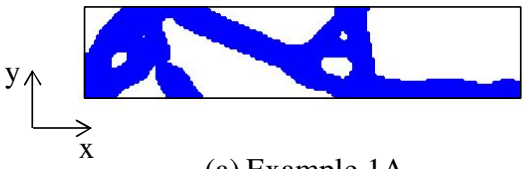

(a) Example 1A

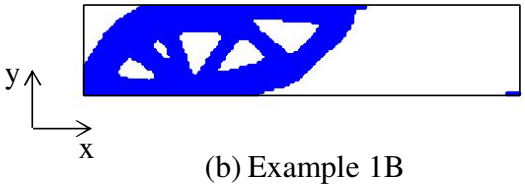

(b) Example 1B

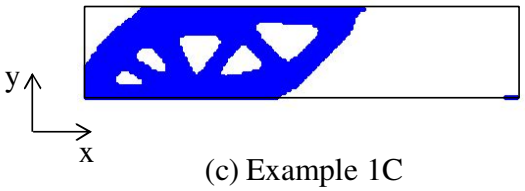

(c) Example 1C

Figure 5.7: Optimal configurations of Example 1

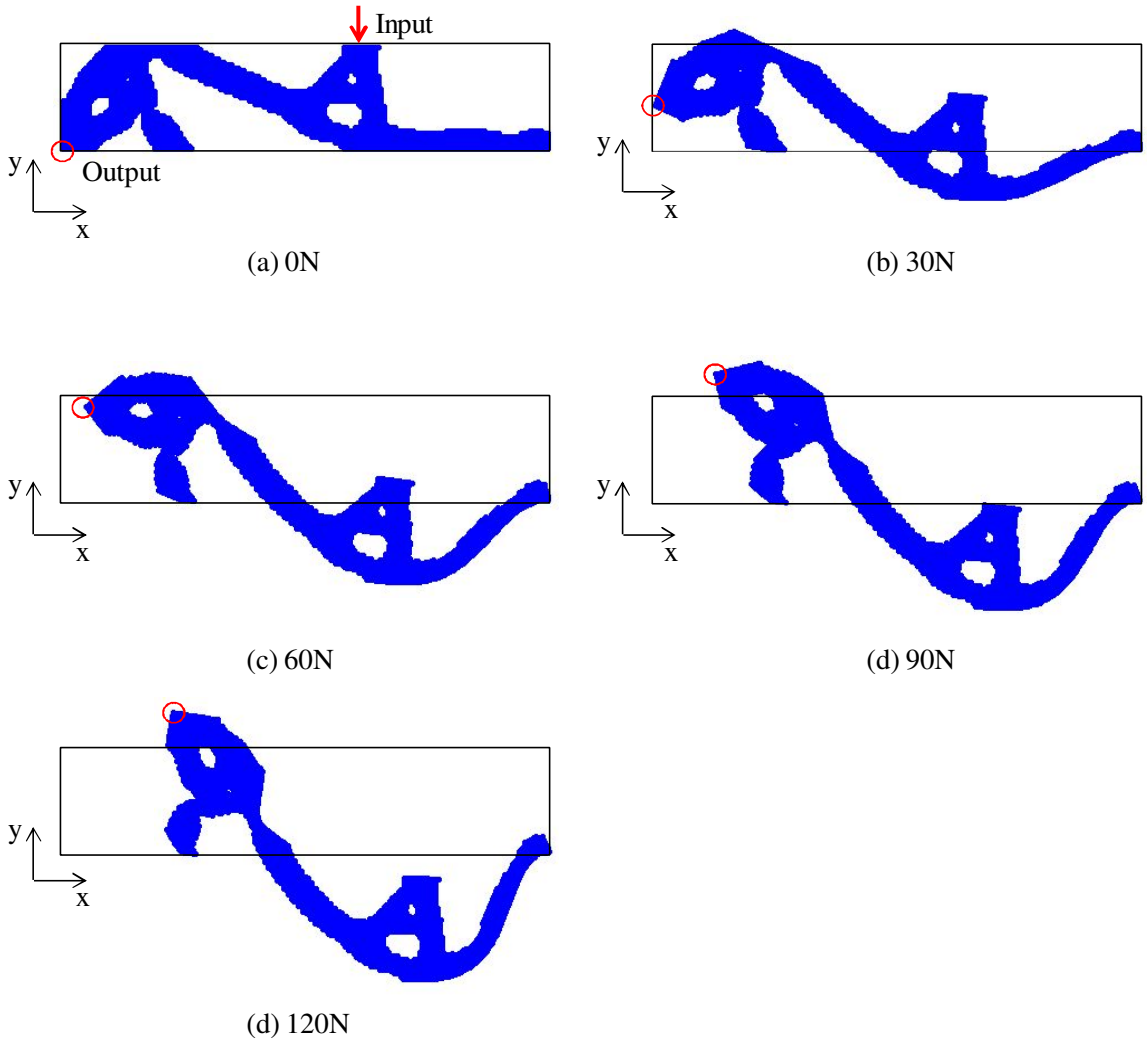

Figure 5.8: Deformations of Example 1A

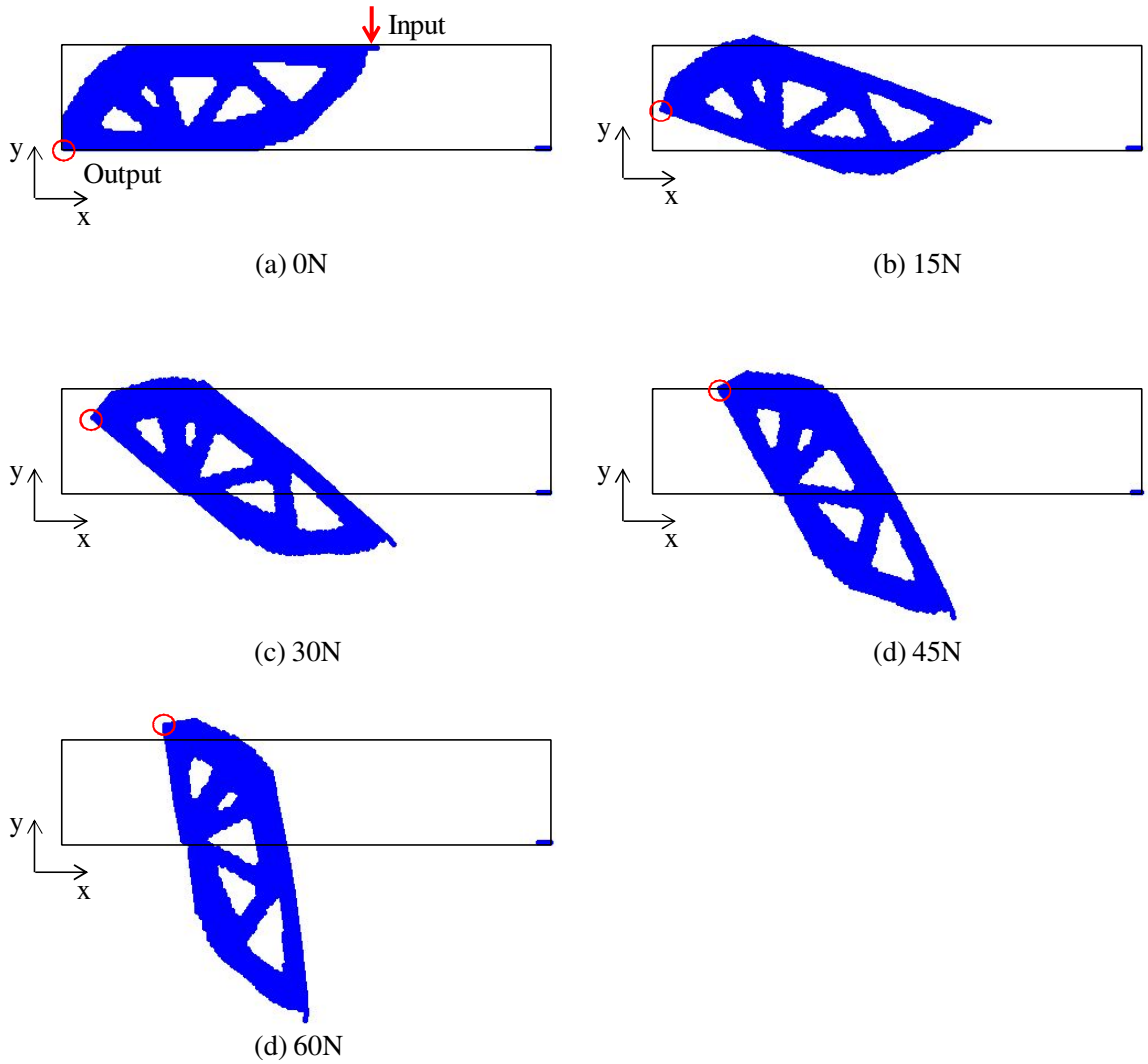

Figure 5.9: Deformations of Example 1B

port in the $+y$ direction is achieved as the main curved portion of the structure undergoes large deformation. On the other hand, in Example 1B, the output port (Γ_{out}) moves in the $+y$ direction as the entire structure rotates around the left fixed point. That is, given the small deformation assumption, the $+y$ direction displacement of the output port is achieved by deformation in a small area around the center of rotation, but this assumption inhibits large deformations of the entire structure, even when loading is increased, causing deformation near the rotation center to increase. Figure 5.10 shows plots of input in the $-y$ direction versus output displacement in the $+y$ direction for Examples 1A and 1B. The displacement achieved by the optimal configuration of Example 1A, obtained using the MPS method, is larger than that of Example 1B, which used the FEM.

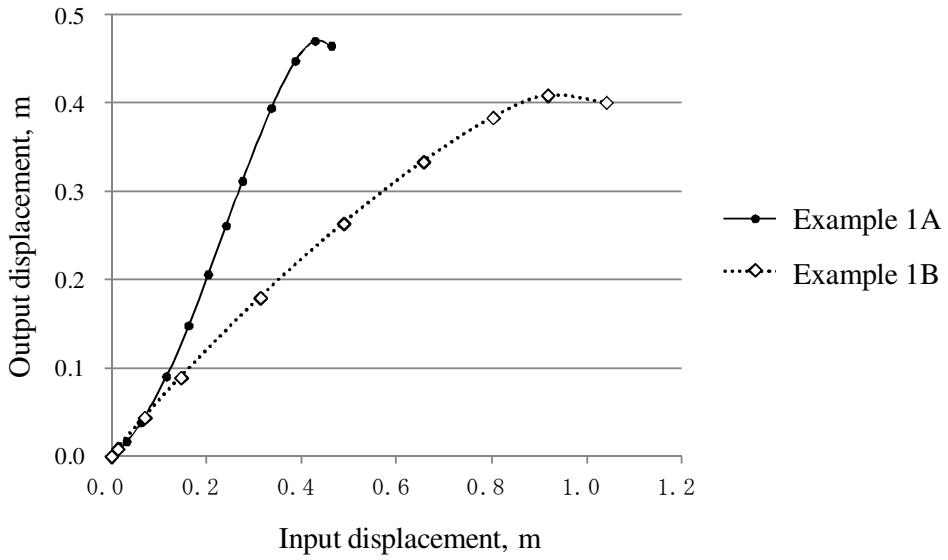

Figure 5.10: Input and output displacement plots of Example 1

5.4.2 Compliant mechanism design 2

The design domain of numerical Example 2 is a 1.00m $\times$ 1.00m square. The top right and bottom left segments of the design domain are fixed (Fig.5.11) and the aim is

to maximize the displacement of the output port in the direction of $\boldsymbol{t}_{\text{out}}$ as shown when a traction $\boldsymbol{t}_{\text{in}}$ is imposed. In the same manner as for Example 1, springs $\boldsymbol{k}_{\text{in}}$ and

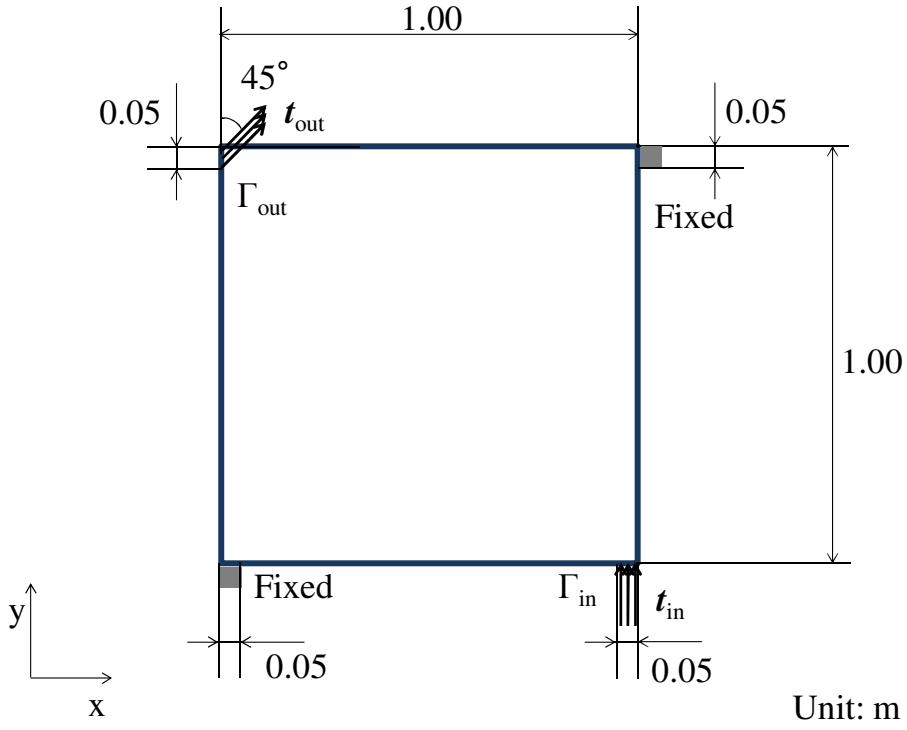

Figure 5.11: Design domain and boundary conditions of Example 2

$\boldsymbol{k}_{\text{out}}$ are set at the locations where $\boldsymbol{t}_{\text{in}}$ and $\boldsymbol{t}_{\text{out}}$ are applied, respectively, to ensure the stiffness of the structure against the action and reaction forces. A Dirichlet boundary condition is imposed at the fixed boundaries and at the boundaries where tractions are imposed, and the other boundaries have a Neumann boundary condition imposed. The material is assumed to be a soft silicone rubber and the material properties are same as those for Example 1. The element size of the FEM mesh and the particle size for the MPS method are 1.0×10^{-2}m, the same as for Example 1. A volume constraint of 40% is used.

A load of 1.0×10^{4}N is applied at $\boldsymbol{t}_{\text{in}}$ (Example 2A). For comparison, the same model is optimized using linear FEM analysis (Example 2B) and an optimization

Table 5.2: Analysis methods, traction forces, spring constants, and regularization coefficients of Example 2

	Example 2A	Example 2B	Example 2C
Analysis method	MPS method	FEM	MPS method
$\boldsymbol{t}_{\text{in}}$ [N]	1.0×10^4	1.0×10^4	1.0×10^0
$\boldsymbol{t}_{\text{out}}$ [N]	1.0×10^4	1.0×10^4	1.0×10^0
$\boldsymbol{k}_{\text{in}}$ [N]	2.0×10^7	2.0×10^7	2.0×10^7
$\boldsymbol{k}_{\text{out}}$ [N]	2.0×10^7	2.0×10^7	2.0×10^7
τ	1.0×10^{-4}	1.0×10^{-4}	1.0×10^{-4}

problem in which the applied load is small is also carried out (Example 2C). The regularization parameter τ, which affects the degree of geometric complexity, is set to 1.0×10^{-4} in all examples. The above conditions are listed in Table 5.2.

The optimization results are shown in Fig.5.12. The optimal configurations ob-

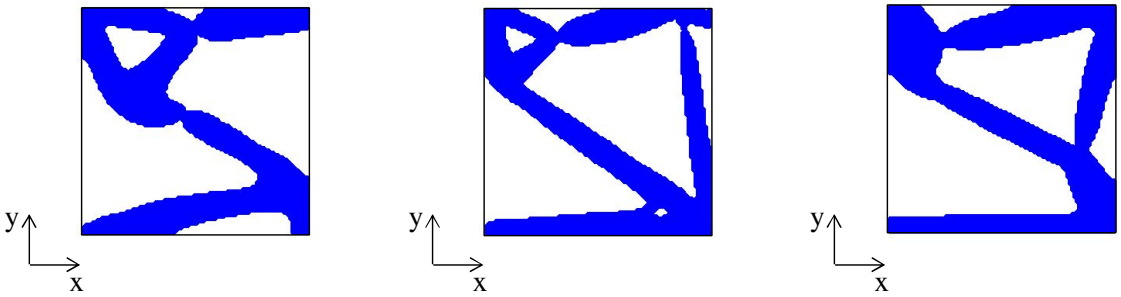

(a) Example 2A (b) Example 2B (c) Example 2C

Figure 5.12: Optimal configurations of Example 2

tained by the geometrically nonlinear MPS analysis method (Example 2A) and the linear FEM analysis (Example 2B) are markedly different. In Example 2B, the input port (Γ_{in}) and the top right fixed boundary are connected by a structure that is not present in Example 2A. The optimal configuration obtained by the MPS method under small loading (Example 2C) has a strut similar to that in Example 2B, which connects the input port at the lower right corner and the fixed boundary at the upper right corner. The deformations of the optimal configurations for Examples 2A and 2B are shown in Figs.5.13 and 5.14, respectively. The displacement at the output

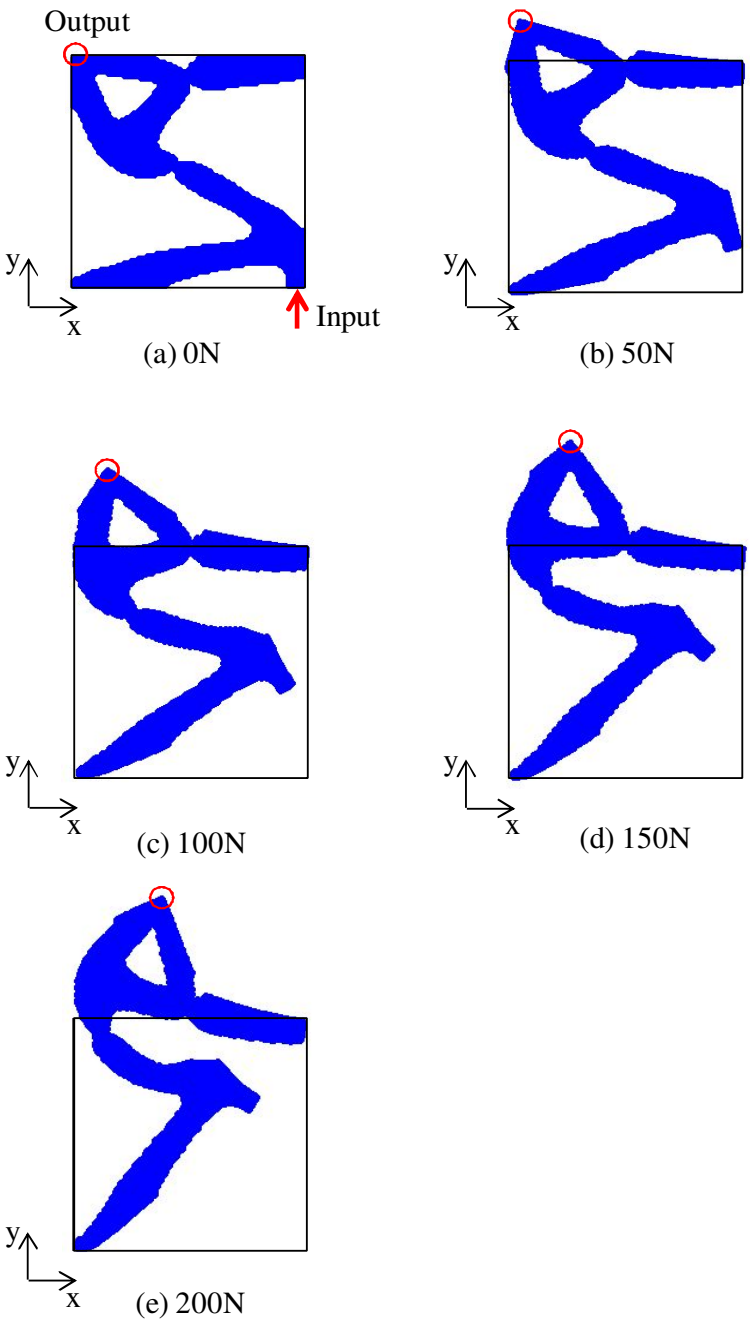

Figure 5.13: Deformations of Example 2A

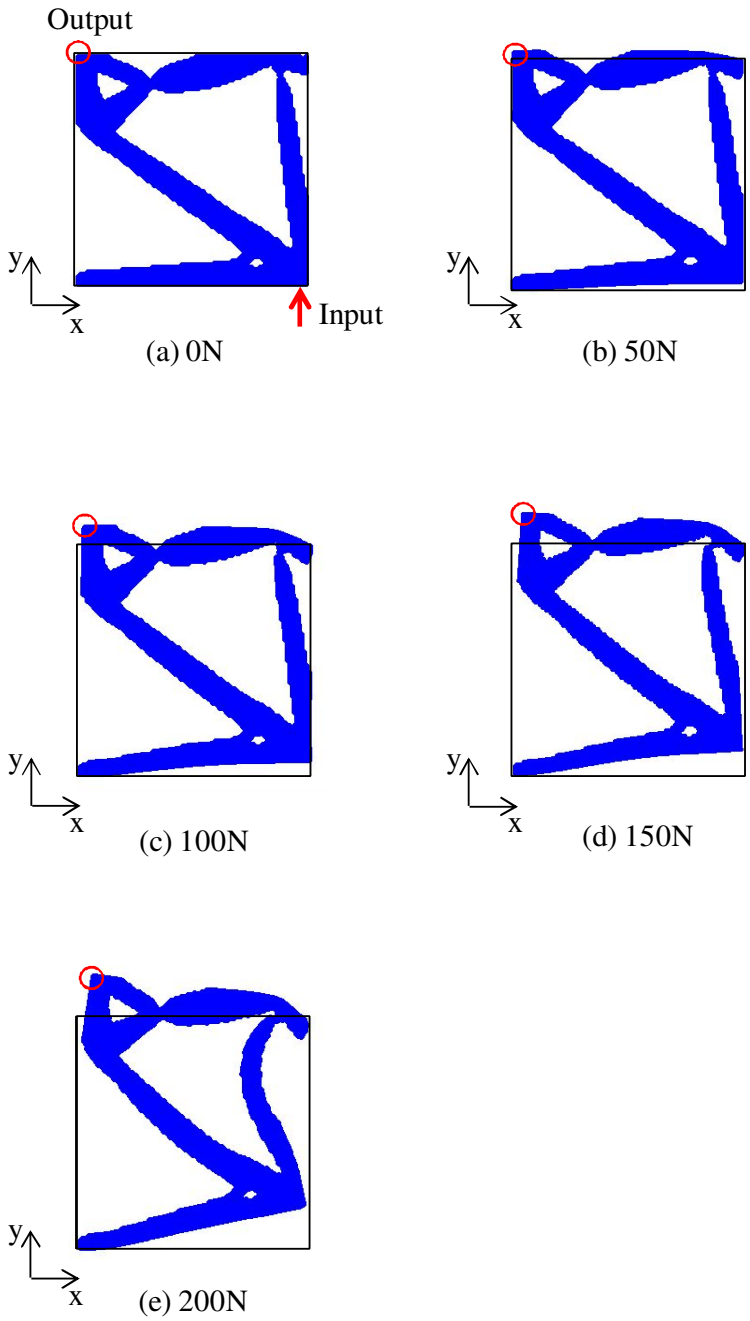

Figure 5.14: Deformations of Example 2B

port (Γ_{out}) in Example 2A is much larger than that in Example 2B, given the same input port loading. The connecting strut in the optimal configuration between the input port and the fixed boundary is beneficial for the desired performance when the deformation is small, but it restricts displacement at the output port when the deformation is large (Fig.5.14). On the other hand, in Example 2A, displacements at the output port are achieved as the entire structure deforms, whereas in Example 2B, the presence of the connecting strut constrains this deformation. Figure 5.15 shows plots of input versus output displacement for Examples 2A and 2B. The displacements achieved by the optimal configuration in Example 2A, obtained using the MPS method, are larger than those in Example 2B, for which the FEM was used, but displacements in Example 2B are larger than those in Example 2A for small deformations.

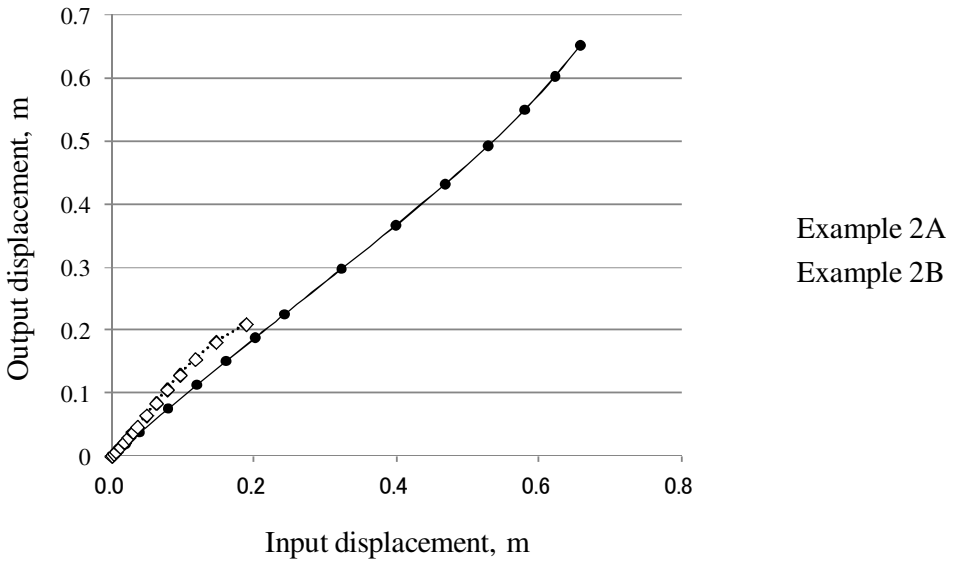

Figure 5.15: Input and output displacement plots of Example 2

The results of Examples 1 and 2 demonstrate that the proposed method, which incorporates geometrically nonlinear analysis, is suitable for the optimization of compliant mechanisms that undergo large deformations.

5.5 Conclusion

A topology optimization method for structures that undergo large deformations was developed and the following results were obtained:

(1) A level set-based optimization method for compliant mechanisms that undergo large deformations was developed by analyzing the state and adjoint state equations using an MPS method that enables geometrically nonlinear analysis.

(2) The utility of the proposed method was verified through numerical examples of compliant mechanisms. The optimal configurations obtained by the proposed topology optimization method using the MPS method were compared with those obtained by a topology optimization method using linear FEM-based analysis. These two methods obtained dramatically different optimal configurations of the compliant mechanisms.

It is concluded that the proposed level set-based topology optimization method that uses an MPS method to enable geometrically nonlinear analysis to solve the equilibrium equations is useful for optimization problems of structures that undergo large deformations.

Chapter 6

Thesis Conclusions

This thesis proposed level set-based structural optimization methods that consider electrostatic-structural coupling effects and geometric nonlinearity. Based on the proposed method, design optimization methods for electrostatic actuators, mechanical resonators, and compliant mechanisms are constructed.

In Chapter 2, a level set-based structural optimization method was proposed for dealing with the electrostatic and structural coupling effects. The design requirements for electrostatic actuators in which elastic deformations are caused by electrostatic forces were clarified. An optimization problem was formulated and the sensitivity was derived using the adjoint variable method. Accurate calculation of the electrostatic forces that occur on structural boundaries was realized by making the FEM nodes close to the structural boundaries congruent with those of the structural boundaries expressed by the level set function, using a mesh adaptation scheme based on the level set method and Laplacian smoothing. The electrostatic forces were obtained by calculating Maxwell's stress tensors on these matched boundaries. The optimization results in the presented numerical examples satisfied the design requirements and had clear boundaries, demonstrating that the proposed method is useful at an engineering level.

In Chapter 3, a level set-based structural optimization method was proposed for

electrostatic actuator designs that achieve a prescribed driving force profile. The multi-objective functional was formulated so that target driving forces could be defined for several positions of the movable electrode. The same mesh adaptation scheme as that presented in Chapter 2 was used to ensure accurate calculation of electrostatic forces on the structural boundaries. The results of the numerical examples demonstrated that the proposed method provides optimal structures that achieve a prescribed driving force profile, and the obtained designs had clear structural boundaries.

In Chapter 4, a level set-based topology optimization method was presented for design problems of mechanical resonators that proactively utilize the dynamic instability of the structure. The design requirements for these mechanical resonators were clarified and an objective functional was derived based on the concept of kinetic energy maximization. An optimization problem was formulated and the sensitivity was derived using the adjoint variable method. The proposed method provided optimal structures for mechanical resonators that satisfy the design requirements and have clear boundaries. The proposed topology optimization method can therefore effectively deal with structural design problems for mechanical resonators.

In Chapter 5, a level set-based topology optimization method was developed for structures that undergo large deformations. The MPS method, a particle method, enabled consideration of large deformations through geometrically nonlinear analysis. The proposed method achieved optimized designs of compliant mechanisms that undergo large deformations, and the obtained optimal structures were shown to be different from those obtained with an optimization method using FEM-based linear analysis. The results obtained by the proposed method demonstrated its utility for considering large deformations in its optimization.

The optimization methods discussed in this thesis focused on structural optimizations considering the electrostatic-structural coupling effects and geometric nonlinearity. I hope that the results of this doctoral research will facilitate the implementation of structural optimizations based on mathematical and physical grounds, and lead to

improved designs of devices that solve real-world problems.

Appendix

Sensitivity analysis for structural optimization of electrostatic actuators considering driving force profiles

The details of the derivation of sensitivity for structural optimization of electro-static actuators considering driving force profiles are now provided. The optimization problem is formulated as follows.

$$
\begin{aligned}
\min_{\phi(\boldsymbol{x})} \quad & J[\,\boldsymbol{\nabla} V, \phi] = \ln \left\{ \sum_{j=1}^{m} \exp\Big(w^j \, F[\,\boldsymbol{\nabla} V^j, \phi] \Big) \right\} \\
\text{subject to} \quad & \boldsymbol{\nabla} \cdot (\epsilon(\phi)\, \boldsymbol{\nabla} V^j) = 0 && \text{in} \quad D \\
& V^j = \overline{V} && \text{on} \quad \Gamma_V \\
& q^j = -(\epsilon(\phi)\, \boldsymbol{\nabla} V^j) \cdot \boldsymbol{n}_D = 0 && \text{on} \quad \Gamma_q \\
& j = 1, ..., m
\end{aligned}
$$

where $F[\,\boldsymbol{\nabla} V^j]$ represents the square of the difference between the j-th actual driving force $\boldsymbol{T}(\,\boldsymbol{\nabla} V^j, \phi)$ and the j-th target driving force $\boldsymbol{T}^{j*}$, as follows:

$$
F[\,\boldsymbol{\nabla} V^j, \phi] = \big\{ \boldsymbol{T}(\,\boldsymbol{\nabla} V^j, \phi) - \boldsymbol{T}^{j*} \big\}^2 .
$$

The actual driving force $\boldsymbol{T}(\,\boldsymbol{\nabla} V^j)$ is represented based on Maxwell's stress tensor:

$$
\boldsymbol{T}(\,\boldsymbol{\nabla} V^j, \phi) = \int_s \boldsymbol{t}(\,\boldsymbol{\nabla} V^j) \cdot \boldsymbol{n}_s(\phi) \; \mathrm{d}\Gamma,
$$

where s is the boundary of an electrode in a comb drive electrostatic actuator, $\boldsymbol{n}_s$ is a unit normal vector on boundary s, and

$$\begin{aligned}\boldsymbol{t}(\boldsymbol{\nabla} V^j) &= \boldsymbol{t}(\boldsymbol{E}^j) \\ &:= -\epsilon_0 \left\{ \boldsymbol{E}^j \otimes \boldsymbol{E}^j - \frac{1}{2}(\boldsymbol{E}^j \cdot \boldsymbol{E}^j)\boldsymbol{I} \right\}.\end{aligned}$$

Furthermore, boundary s and unit normal vector $\boldsymbol{n}_s$ are dependent on the level set function ϕ, and the boundary integral can be represented as a domain integral by using level set function ϕ as follows:

$$\boldsymbol{T}(\boldsymbol{\nabla} V^j, \phi) = \int_D \boldsymbol{t}(\boldsymbol{\nabla} V^j) \bar{\boldsymbol{\delta}}(\phi) \, \mathrm{d}D,$$

where $\bar{\boldsymbol{\delta}}(\phi)$ is defined using an approximated Heaviside function $H_a(\phi)$ as follows:

$$\bar{\boldsymbol{\delta}}(\phi) := \frac{\boldsymbol{\nabla}\phi}{|\boldsymbol{\nabla}\phi|} \frac{\mathrm{d}H_a(\phi)}{\mathrm{d}\ \phi}.$$

Now, let us consider the Lagrangian $\overline{J}$ as follows:

$$\begin{aligned}\overline{J}[\boldsymbol{\nabla} V, \phi] &= \ln \left[\sum_{j=1}^{m} \exp \left\{ w^j \left(\int_D \boldsymbol{t}(\boldsymbol{\nabla} V^j) \bar{\boldsymbol{\delta}}(\phi) \, \mathrm{d}D - \boldsymbol{T}^{j*} \right)^2 \right\} \right] + \sum_{j=1}^{m} \left[\int_D \hat{V}^j \boldsymbol{\nabla} \cdot (\epsilon(\phi) \boldsymbol{\nabla} V^j) \, \mathrm{d}D \right] \\ &= \ln \left[\sum_{j=1}^{m} \exp \left\{ w^j \left(\int_D \boldsymbol{t}(\boldsymbol{\nabla} V^j) \bar{\boldsymbol{\delta}}(\phi) \, \mathrm{d}D - \boldsymbol{T}^{j*} \right)^2 \right\} \right] \\ &\quad + \sum_{j=1}^{m} \left[- \int_D (\boldsymbol{\nabla} \hat{V}^j) \cdot \{\epsilon(\phi) \boldsymbol{\nabla} V^j\} \, \mathrm{d}D + \int_D \boldsymbol{\nabla} \cdot \{\hat{V}^j \epsilon(\phi) \boldsymbol{\nabla} V^j\} \, \mathrm{d}D \right] \\ &= \ln \left[\sum_{j=1}^{m} \exp \left\{ w^j \left(\int_D \boldsymbol{t}(\boldsymbol{\nabla} V^j) \bar{\boldsymbol{\delta}}(\phi) \, \mathrm{d}D - \boldsymbol{T}^{j*} \right)^2 \right\} \right] \\ &\quad + \sum_{j=1}^{m} \left[- \int_D (\boldsymbol{\nabla} \hat{V}^j) \cdot \{\epsilon(\phi) \boldsymbol{\nabla} V^j\} \, \mathrm{d}D + \int_\Gamma \hat{V}^j q^j \, \mathrm{d}\Gamma \right]\end{aligned}$$

Lagrangian $\overline{J}$ changes when the design variable ϕ slightly changes, so we have

$$\begin{aligned}\overline{J} + \delta\overline{J} = \ln &\left[\sum_{j=1}^{m} \exp \left\{ w^j \left(\int_D \left(\boldsymbol{t}(\boldsymbol{\nabla} V^j) + \frac{\partial \boldsymbol{t}(\boldsymbol{\nabla} V^j)}{\partial (\boldsymbol{\nabla} V^j)} \delta(\boldsymbol{\nabla} V^j) \right) \left(\bar{\boldsymbol{\delta}}(\phi) + \frac{\partial \bar{\boldsymbol{\delta}}(\phi)}{\partial \phi} \delta\phi \right) \, \mathrm{d}D - \boldsymbol{T}^{j*} \right)^2 \right\} \right] \\ &+ \sum_{j=1}^{m} \left[- \int_D (\boldsymbol{\nabla} \hat{V}^j) \cdot \left\{ \left(\epsilon(\phi) + \frac{\partial \epsilon(\phi)}{\partial \phi} \delta\phi \right) \left(\boldsymbol{\nabla} V^j + \delta(\boldsymbol{\nabla} V^j) \right) \right\} \, \mathrm{d}D + \int_\Gamma \hat{V}^j (q^j + \delta q^j) \, \mathrm{d}\Gamma \right]\end{aligned}$$

Therefore, we have

$$\delta\overline{J} = \ln\left[\sum_{j=1}^{m}\exp\left\{w^j\ \left(\int_D\left(\boldsymbol{t}(\ \boldsymbol{\nabla}V^j) + \frac{\partial\boldsymbol{t}(\ \boldsymbol{\nabla}V^j)}{\partial(\ \boldsymbol{\nabla}V^j)}\delta(\boldsymbol{\nabla}V^j)\right)\bar{\boldsymbol{\delta}}(\phi)\ \mathrm{d}D + \int_D\left(\boldsymbol{t}(\ \boldsymbol{\nabla}V^j)\frac{\partial\bar{\boldsymbol{\delta}}(\phi)}{\partial\phi}\delta\phi\right)\ \mathrm{d}D - \boldsymbol{T}^{j*}\right)^2\right\}\right]$$
$$- \ln\left[\sum_{j=1}^{m}\exp\left\{w^j\ \left(\int_D\boldsymbol{t}(\ \boldsymbol{\nabla}V^j)\bar{\boldsymbol{\delta}}(\phi)\ \mathrm{d}D - \boldsymbol{T}^{j*}\right)^2\right\}\right]$$
$$+\sum_{j=1}^{m}\left[-\int_D(\ \boldsymbol{\nabla}\hat{V}^j)\cdot\left\{\epsilon(\phi)\delta(\boldsymbol{\nabla}V^j) + \frac{\partial\epsilon(\phi)}{\partial\phi}\delta\phi\,\boldsymbol{\nabla}V^j\right\}\ \mathrm{d}D + \int_\Gamma\hat{V}^j\delta q^j\ \mathrm{d}\Gamma\right],$$

where the second order variations are neglected in the third term.

Now, the first and second term are evaluated. That is, we consider the variation of the objective functional δJ. First, the notations are defined as follows:

$$\boldsymbol{T}^j := \int_D\boldsymbol{t}(\ \boldsymbol{\nabla}V^j)\cdot\bar{\boldsymbol{\delta}}(\phi)\ \mathrm{d}D$$
$$\delta\boldsymbol{T}^j := \int_D\left(\frac{\partial\boldsymbol{t}(\ \boldsymbol{\nabla}V^j)}{\partial(\ \boldsymbol{\nabla}V^j)}\delta(\boldsymbol{\nabla}V^j)\right)\bar{\boldsymbol{\delta}}(\phi)\ \mathrm{d}D + \int_D\left(\boldsymbol{t}(\ \boldsymbol{\nabla}V^j)\frac{\partial\bar{\boldsymbol{\delta}}(\phi)}{\partial\phi}\delta\phi\right)\ \mathrm{d}D.$$

Then, δJ is written as

$$\delta J = \ln\left[\sum_{j=1}^{m}\exp\left\{w^j\ \left(\boldsymbol{T}^j + \delta\boldsymbol{T}^j - \boldsymbol{T}^{j*}\right)^2\right\}\right] - \ln\left[\sum_{j=1}^{m}\exp\left\{w^j\ \left(\boldsymbol{T}^j - \boldsymbol{T}^{j*}\right)^2\right\}\right]$$
$$= \ln\left[\frac{\displaystyle\sum_{j=1}^{m}\exp\left\{w^j\ \left(\boldsymbol{T}^j + \delta\boldsymbol{T}^j - \boldsymbol{T}^{j*}\right)^2\right\}}{\displaystyle\sum_{j=1}^{m}\exp\left\{w^j\ \left(\boldsymbol{T}^j - \boldsymbol{T}^{j*}\right)^2\right\}}\right]$$
$$= \ln\left[\frac{\displaystyle\sum_{j=1}^{m}\exp\left\{w^j\ \left({\boldsymbol{T}^j}^2 + 2\boldsymbol{T}^j\cdot\delta\boldsymbol{T}^j - 2\boldsymbol{T}^j\cdot\boldsymbol{T}^{j*} - 2\boldsymbol{T}^{j*}\cdot\delta\boldsymbol{T}^j + {\boldsymbol{T}^{j*}}^2\right)\right\}}{\displaystyle\sum_{j=1}^{m}\exp\left\{w^j\ \left(\boldsymbol{T}^j - \boldsymbol{T}^{j*}\right)^2\right\}}\right],$$

where second order variations are neglected. Rewriting the above, we have

$$\delta J = \ln\left[\frac{\displaystyle\sum_{j=1}^{m}\left\{\exp(w^j{\boldsymbol{T}^j}^2)\ \exp(2w^j\boldsymbol{T}^j\cdot\delta\boldsymbol{T}^j)\ \exp(-2w^j\boldsymbol{T}^j\cdot\boldsymbol{T}^{j*})\ \exp(-2w^j\boldsymbol{T}^{j*}\cdot\delta\boldsymbol{T}^j)\ \exp(w^j{\boldsymbol{T}^{j*}}^2)\right\}}{\displaystyle\sum_{j=1}^{m}\exp\left\{w^j\ \left(\boldsymbol{T}^j - \boldsymbol{T}^{j*}\right)^2\right\}}\right].$$

Here, let us recall the Maclaurin expansion with respect to $\exp(x)$:

$$\exp(x) = \sum_{n=0}^{\infty}\frac{x^n}{n!}$$

Therefore, we have

$$\delta J = \ln \left[\frac{\sum_{j=1}^{m} \left\{ \exp(w^j {\boldsymbol{T}^j}^2) \left(1 + 2w^j \boldsymbol{T}^j \cdot \delta \boldsymbol{T}^j\right) \exp(-2w^j \boldsymbol{T}^j \cdot \boldsymbol{T}^{j*}) \left(1 - 2w^j \boldsymbol{T}^{j*} \cdot \delta \boldsymbol{T}^j\right) \exp(w^j {\boldsymbol{T}^{j*}}^2) \right\}}{\sum_{j=1}^{m} \exp\left\{ w^j \left(\boldsymbol{T}^j - \boldsymbol{T}^{j*}\right)^2 \right\}} \right]$$

$$= \ln \left[\frac{\sum_{j=1}^{m} \left\{ \exp(w^j {\boldsymbol{T}^j}^2) \exp(-2w^j \boldsymbol{T}^j \cdot \boldsymbol{T}^{j*}) \exp(w^j {\boldsymbol{T}^{j*}}^2) (1 + 2w^j \boldsymbol{T}^j \cdot \delta \boldsymbol{T}^j - 2w^j \boldsymbol{T}^{j*} \cdot \delta \boldsymbol{T}^j) \right\}}{\sum_{j=1}^{m} \exp\left\{ w^j \left(\boldsymbol{T}^j - \boldsymbol{T}^{j*}\right)^2 \right\}} \right],$$

where second order variations are neglected. Rewriting the above, we have

$$\delta J = \ln \left[\frac{\sum_{j=1}^{m} \left\{ \exp\left(w^j \left(\boldsymbol{T}^j - \boldsymbol{T}^{j*}\right)^2 \right) \left(1 + 2w^j \boldsymbol{T}^j \cdot \delta \boldsymbol{T}^j - 2w^j \boldsymbol{T}^{j*} \cdot \delta \boldsymbol{T}^j\right) \right\}}{\sum_{j=1}^{m} \exp\left\{ w^j \left(\boldsymbol{T}^j - \boldsymbol{T}^{j*}\right)^2 \right\}} \right]$$

$$= \ln \left[1 + \frac{\sum_{j=1}^{m} 2w^j \left\{ \exp\left(w^j \left(\boldsymbol{T}^j - \boldsymbol{T}^{j*}\right)^2 \right) \left(\boldsymbol{T}^j - \boldsymbol{T}^{j*}\right) \cdot \delta \boldsymbol{T}^j \right\}}{\sum_{j=1}^{m} \exp\left\{ w^j \left(\boldsymbol{T}^j - \boldsymbol{T}^{j*}\right)^2 \right\}} \right].$$

Now, the following notation, W^j, is introduced.

$$W^j := \exp\left(w^j \left(\boldsymbol{T}^j - \boldsymbol{T}^{j*}\right)^2 \right).$$

Then, we have

$$\delta J = \ln \left[1 + \frac{2\sum_{j=1}^{m} w^j W^j (\boldsymbol{T}^j - \boldsymbol{T}^{j*}) \cdot \delta \boldsymbol{T}^j}{\sum_{j=1}^{m} W^j} \right]$$

$$= \left(\frac{2\sum_{j=1}^{m} w^j W^j (\boldsymbol{T}^j - \boldsymbol{T}^{j*}) \cdot \delta \boldsymbol{T}^j}{\sum_{j=1}^{m} W^j} \right) \ln \left[1 + \frac{2\sum_{j=1}^{m} w^j W^j (\boldsymbol{T}^j - \boldsymbol{T}^{j*}) \cdot \delta \boldsymbol{T}^j}{\sum_{j=1}^{m} W^j} \right] \left(\frac{\sum_{j=1}^{m} W^j}{2\sum_{j=1}^{m} w^j W^j (\boldsymbol{T}^j - \boldsymbol{T}^{j*}) \cdot \delta \boldsymbol{T}^j} \right)$$

Now, let us recall the definition of Napier's number e and its relationship, as follows:

$$\begin{aligned} e :&= \lim_{x\to\infty}\left(1+\frac{1}{x}\right)^{x} = \lim_{x\to-\infty}\left(1+\frac{1}{x}\right)^{x} \\ &= \lim_{x\to 0}\left(1+x\right)^{\frac{1}{x}}. \end{aligned}$$

Therefore, we have

$$\begin{aligned} \delta J &= \left(\frac{2}{\sum W^j}\right)\sum_{j=1}^{m} w^j W^j (\boldsymbol{T}^j - \boldsymbol{T}^{j*})\cdot \delta \boldsymbol{T}^j \\ &= \left(\frac{2}{\sum W^j}\right)\sum_{j=1}^{m} w^j W^j (\boldsymbol{T}^j - \boldsymbol{T}^{j*})\cdot \left[\int_D \left(\frac{\partial \boldsymbol{t}(\boldsymbol{\nabla} V^j)}{\partial(\boldsymbol{\nabla} V^j)}\delta(\boldsymbol{\nabla} V^j)\right)\bar{\boldsymbol{\delta}}(\phi)\ \mathrm{d}D + \int_D \left(\boldsymbol{t}(\boldsymbol{\nabla} V^j)\frac{\partial \bar{\boldsymbol{\delta}}(\phi)}{\partial \phi}\delta\phi\right)\ \mathrm{d}D\right] \end{aligned}$$

Based on the above derivation for δJ, we re-consider the variation of Lagrangian $\delta\overline{J}$, as follows:

$$\begin{aligned} \delta\overline{J} = &\left(\frac{2}{\sum W^j}\right)\sum_{j=1}^{m} w^j W^j (\boldsymbol{T}^j - \boldsymbol{T}^{j*})\cdot \left[\int_D \left(\frac{\partial \boldsymbol{t}(\boldsymbol{\nabla} V^j)}{\partial(\boldsymbol{\nabla} V^j)}\delta(\boldsymbol{\nabla} V^j)\right)\bar{\boldsymbol{\delta}}(\phi)\ \mathrm{d}D + \int_D \left(\boldsymbol{t}(\boldsymbol{\nabla} V^j)\frac{\partial \bar{\boldsymbol{\delta}}(\phi)}{\partial \phi}\delta\phi\right)\ \mathrm{d}D\right] \\ &+\sum_{j=1}^{m}\left[-\int_D (\boldsymbol{\nabla}\hat{V}^j)\cdot\left\{\epsilon(\phi)\delta(\boldsymbol{\nabla} V^j) + \frac{\partial \epsilon(\phi)}{\partial \phi}\delta\phi\,\boldsymbol{\nabla} V^j\right\}\ \mathrm{d}D + \int_\Gamma \hat{V}^j \delta q^j\ \mathrm{d}\Gamma\right]. \end{aligned}$$

Given the boundary condition on Γ_q, we have the following relationship:

$$\delta q^j = 0 \qquad \text{on} \quad \Gamma_q.$$

Thus, we have

$$\begin{aligned} \delta\overline{J} = &\left(\frac{2}{\sum W^j}\right)\sum_{j=1}^{m} w^j W^j (\boldsymbol{T}^j - \boldsymbol{T}^{j*})\cdot \left[\int_D \left(\frac{\partial \boldsymbol{t}(\boldsymbol{\nabla} V^j)}{\partial(\boldsymbol{\nabla} V^j)}\delta(\boldsymbol{\nabla} V^j)\right)\bar{\boldsymbol{\delta}}(\phi)\ \mathrm{d}D + \int_D \left(\boldsymbol{t}(\boldsymbol{\nabla} V^j)\frac{\partial \bar{\boldsymbol{\delta}}(\phi)}{\partial \phi}\delta\phi\right)\ \mathrm{d}D\right] \\ &+\sum_{j=1}^{m}\left[-\int_D (\boldsymbol{\nabla}\hat{V}^j)\cdot\left\{\epsilon(\phi)\delta(\boldsymbol{\nabla} V^j) + \frac{\partial \epsilon(\phi)}{\partial \phi}\delta\phi\,\boldsymbol{\nabla} V^j\right\}\ \mathrm{d}D + \int_{\Gamma_V} \hat{V}^j \delta q^j\ \mathrm{d}\Gamma\right]. \end{aligned}$$

Now, the term of the variation with respect to Maxwell's stress tensor is evaluated as follows:

$$\begin{aligned}
&\left(\frac{2}{\sum W^j}\right)\sum_{j=1}^{m} w^j W^j (\boldsymbol{T}^j - \boldsymbol{T}^{j*}) \cdot \int_D \left(\frac{\partial \boldsymbol{t}(\,\boldsymbol{\nabla} V^j)}{\partial(\,\boldsymbol{\nabla} V^j)} \delta(\boldsymbol{\nabla} V^j)\right) \bar{\boldsymbol{\delta}}(\phi)\ \mathrm{d}D \\
&\qquad = \sum_{j=1}^{m} \boldsymbol{a}_T^j \cdot \int_D \left(\frac{\partial \boldsymbol{t}(\,\boldsymbol{\nabla} V^j)}{\partial(\,\boldsymbol{\nabla} V^j)} \delta(\boldsymbol{\nabla} V^j)\right) \bar{\boldsymbol{\delta}}(\phi)\ \mathrm{d}D \\
&\qquad = \sum_{j=1}^{m} \boldsymbol{a}_T^j \cdot \int_D \left\{\boldsymbol{t}(\,\boldsymbol{\nabla} V^j + \delta(\boldsymbol{\nabla} V^j)) - \boldsymbol{t}(\,\boldsymbol{\nabla} V^j)\right\} \bar{\boldsymbol{\delta}}(\phi)\ \mathrm{d}D,
\end{aligned}$$

where coefficient vector $\boldsymbol{a}_T$ is defined as

$$\boldsymbol{a}_T^j := \left(\frac{2}{\sum W^j}\right) w^j W^j (\boldsymbol{T}^j - \boldsymbol{T}^{j*})\,,$$

and the derivation of the variation with respect to Maxwell's stress tensor, $\boldsymbol{t}$, is evaluated as below.

$$\begin{aligned}
&\boldsymbol{t}(\,\boldsymbol{\nabla} V^j + \delta(\boldsymbol{\nabla} V^j)) - \boldsymbol{t}(\,\boldsymbol{\nabla} V^j) \\
&\quad = -\epsilon_0 \left[(\,\boldsymbol{\nabla} V^j + \delta(\boldsymbol{\nabla} V^j)) \otimes (\,\boldsymbol{\nabla} V^j + \delta(\boldsymbol{\nabla} V^j)) - \frac{1}{2}\Big\{(\,\boldsymbol{\nabla} V^j + \delta(\boldsymbol{\nabla} V^j)) \cdot (\,\boldsymbol{\nabla} V^j + \delta(\boldsymbol{\nabla} V^j))\Big\}\boldsymbol{I}\right] \\
&\qquad\quad + \epsilon_0 \left\{(\,\boldsymbol{\nabla} V^j) \otimes (\,\boldsymbol{\nabla} V^j) - \frac{1}{2}(\,\boldsymbol{\nabla} V^j \cdot\, \boldsymbol{\nabla} V^j)\boldsymbol{I}\right\} \\
&\quad = -2\epsilon_0 \left[(\,\boldsymbol{\nabla} V) \otimes (\delta(\boldsymbol{\nabla} V^j)) - \frac{1}{2}(\,\boldsymbol{\nabla} V^j) \cdot (\delta(\boldsymbol{\nabla} V^j))\boldsymbol{I}\right],
\end{aligned}$$

where second order variations are neglected. Therefore, we have

$$\begin{aligned}
&\left(\frac{2}{\sum W^j}\right)\sum_{j=1}^{m} w^j W^j (\boldsymbol{T}^j - \boldsymbol{T}^{j*}) \cdot \int_D \left(\frac{\partial \boldsymbol{t}(\,\boldsymbol{\nabla} V^j)}{\partial(\,\boldsymbol{\nabla} V^j)} \delta(\boldsymbol{\nabla} V^j)\right) \bar{\boldsymbol{\delta}}(\phi)\ \mathrm{d}D \\
&\quad = \sum_{j=1}^{m} \boldsymbol{a}_T^j \cdot \int_D \left[-2\epsilon_0 \left\{(\,\boldsymbol{\nabla} V^j) \otimes \delta(\boldsymbol{\nabla} V^j) - \frac{1}{2}(\,\boldsymbol{\nabla} V^j) \cdot (\delta(\boldsymbol{\nabla} V^j))\boldsymbol{I}\right\}\right] \bar{\boldsymbol{\delta}}(\phi)\ \mathrm{d}D \\
&\quad = -2\epsilon_0 \sum_{j=1}^{m} \boldsymbol{a}_T^j \cdot \left[\int_D \left\{(\,\boldsymbol{\nabla} V^j) \otimes \delta(\boldsymbol{\nabla} V^j)\right\} \bar{\boldsymbol{\delta}}(\phi)\ \mathrm{d}D\right] + \epsilon_0 \sum_{j=1}^{m} \boldsymbol{a}_T^j \cdot \left[\int_D \left[\left\{(\,\boldsymbol{\nabla} V^j) \cdot \delta(\boldsymbol{\nabla} V^j)\right\} \boldsymbol{I}\right] \bar{\boldsymbol{\delta}}(\phi)\ \mathrm{d}D\right] \\
&\quad = -2\epsilon_0 \sum_{j=1}^{m} \boldsymbol{a}_T^j \cdot \left[\int_D \left\{(\,\boldsymbol{\nabla} V^j) \otimes \bar{\boldsymbol{\delta}}(\phi)\right\} \delta(\boldsymbol{\nabla} V^j)\ \mathrm{d}D\right] + \epsilon_0 \sum_{j=1}^{m} \boldsymbol{a}_T^j \cdot \left[\int_D \left\{\boldsymbol{I}\bar{\boldsymbol{\delta}}(\phi)\right\} \left\{(\,\boldsymbol{\nabla} V^j) \cdot \delta(\boldsymbol{\nabla} V^j)\right\}\ \mathrm{d}D\right] \\
&\quad = -2\epsilon_0 \sum_{j=1}^{m} \int_D \left[\left\{(\,\boldsymbol{\nabla} V^j) \otimes \bar{\boldsymbol{\delta}}(\phi)\right\}^T \boldsymbol{a}_T^j\right] \cdot \delta(\boldsymbol{\nabla} V^j)\ \mathrm{d}D + \epsilon_0 \sum_{j=1}^{m} \int_D \left[\boldsymbol{a}_T^j \cdot \left\{\boldsymbol{I}\bar{\boldsymbol{\delta}}(\phi)\right\} (\,\boldsymbol{\nabla} V^j)\right] \cdot \delta(\boldsymbol{\nabla} V^j)\ \mathrm{d}D \\
&\quad = \epsilon_0 \sum_{j=1}^{m} \int_D \left(-2\left[\left\{(\,\boldsymbol{\nabla} V^j) \otimes \bar{\boldsymbol{\delta}}(\phi)\right\}^T \boldsymbol{a}_T^j\right] + \left[\boldsymbol{a}_T^j \cdot \left\{\boldsymbol{I}\bar{\boldsymbol{\delta}}(\phi)\right\} (\,\boldsymbol{\nabla} V^j)\right]\right) \cdot \delta(\boldsymbol{\nabla} V^j)\ \mathrm{d}D.
\end{aligned}$$

Based on the above evaluation, we have

$$\begin{aligned}\delta\overline{J} = &\sum_{j=1}^{m}\left[\int_D\left[-2\epsilon_0\left\{\{(\boldsymbol{\nabla}V^j)\otimes\bar{\boldsymbol{\delta}}(\phi)\}^T\boldsymbol{a}_T^j\right\}+\epsilon_0\left\{\boldsymbol{a}_T^j\cdot\{\boldsymbol{I}\bar{\boldsymbol{\delta}}(\phi)\}(\boldsymbol{\nabla}V^j)\right\}-\epsilon(\phi)\boldsymbol{\nabla}\hat{V}^j\right]\cdot\delta(\boldsymbol{\nabla}V^j)\ \mathrm{d}D\right]\\ &+\sum_{j=1}^{m}\left[\int_D\left\{\left(\frac{2w^jW^j(\boldsymbol{T}^j-\boldsymbol{T}^{j*})}{\sum W^j}\right)\cdot\left(\boldsymbol{t}(\boldsymbol{\nabla}V^j)\frac{\partial\bar{\boldsymbol{\delta}}(\phi)}{\partial\phi}\right)-(\boldsymbol{\nabla}\hat{V}^j)\cdot\left(\frac{\partial\epsilon(\phi)}{\partial\phi}\boldsymbol{\nabla}V^j\right)\right\}\delta\phi\ \mathrm{d}D\right]\\ &+\sum_{j=1}^{m}\left[\int_{\Gamma_V}\hat{V}^j\delta q^j\ \mathrm{d}\Gamma\right].\end{aligned}$$

To make the terms pertaining to $\delta(\boldsymbol{\nabla}V^j)$ and δq^j equivalent to zero, we define the adjoint system as follows:

$$\boldsymbol{\nabla}\hat{V}^j=-2\frac{\epsilon_0}{\epsilon(\phi)}\left[\{(\boldsymbol{\nabla}V^j)\otimes\bar{\boldsymbol{\delta}}(\phi)\}^T\boldsymbol{a}_T^j\right]+\frac{\epsilon_0}{\epsilon(\phi)}\left[\boldsymbol{a}_T^j\cdot\{\boldsymbol{I}\bar{\boldsymbol{\delta}}(\phi)\}(\boldsymbol{\nabla}V^j)\right]\qquad\text{in}\quad D$$

$$\hat{V}^j=0\qquad\text{on}\quad\Gamma_V$$

Then, $\delta\overline{J}$ can be expressed as

$$\delta\overline{J}=\sum_{j=1}^{m}\left[\int_D\left\{\left(\frac{2w^jW^j(\boldsymbol{T}^j-\boldsymbol{T}^{j*})}{\sum W^j}\right)\cdot\left(\boldsymbol{t}(\boldsymbol{\nabla}V^j)\frac{\partial\bar{\boldsymbol{\delta}}(\phi)}{\partial\phi}\right)-(\boldsymbol{\nabla}\hat{V}^j)\cdot\left(\frac{\partial\epsilon(\phi)}{\partial\phi}\boldsymbol{\nabla}V^j\right)\right\}\delta\phi\ \mathrm{d}D\right].$$

We note that the first and second terms respectively represent the effects of geometrical changes and the effects of changes in Maxwell's stress tensor. Therefore, the first term can be neglected when changes in the shape are insignificant.

List of Tables

List of Figures

References

[1] M. P. Bendsøe, N. Kikuchi, Generating optimal topologies in structural design using a homogenization method, Computer Methods in Applied Mechanics and Engineering 71 (2) (1988) 197–224.

[2] K. Suzuki, N. Kikuchi, A homogenization method for shape and topology optimization, Computer Methods in Applied Mechanics and Engineering 121 (1991) 291–318.

[3] A. R. Diaz, N. Kikuchi, Solutions to shape and topology eigenvalue optimization problems using a homogenization method, International Journal for Numerical Methods in Engineering 35 (1992) 1487–1502.

[4] Q. Li, G. P. Steven, O. M. Querin, Y. Xie, Shape and topology design for heat conduction by evolutionary structural optimization, International Journal of Heat and Mass Transfer 42 (17) (1999) 3361–3371.

[5] J. Haslinger, A. Hillebrand, T. Kärkkäinen, M. Miettinen, Optimization of conducting structures by using the homogenization method, Structural and multidisciplinary optimization 24 (2) (2002) 125–140.

[6] A. Iga, S. Nishiwaki, K. Izui, M. Yoshimura, Topology optimization for thermal conductors with heat cpnvection and conduction including design-dependent effects, Int J Heat and Mass Transf 52 (2009) 2721–2732.

[7] T. Borrvall, J. Petersson, Topology optimization of fluids in stokes flow, International Journal for Numerical Methods in Fluids 41 (1) (2003) 77–107.

[8] L. H. Olesen, F. Okkels, H. Bruus, A high-level programming-language implementation of topology optimization applied to steady-state navier–stokes flow, International Journal for Numerical Methods in Engineering 65 (7) (2006) 975–1001.

[9] T. Kondoh, T. Matsumori, A. Kawamoto, Drag minimization and lift maximization in laminar flows via topology optimization employing simple objective function expressions based on body force integration, Structural and Multidisciplinary Optimization 45 (5) (2012) 693–701.

[10] R. Legtenberg, A. Groeneveld, M. Elwenspoek, Comb-drive actuators for large displacements, Journal of Micromechanics and Microengineering 6 (3) (1996) 320–329.

[11] W. Ye, S. Mukherjee, N. MacDonald, Optimal shape design of an electrostatic comb drive in microelectromechanical systems, Journal of Microelectromechanical Systems 7 (1) (1998) 16–26.

[12] W. Ye, S. Mukherjee, Optimal shape design of three-dimensional mems with applications to electrostatic comb drives, International Journal for Numerical Methods in Engineering 45 (2) (1999) 175–194.

[13] J. Grade, H. Jerman, T. Kenny, Design of large deflection electrostatic actuators, Journal of Microelectromechanical Systems 12 (3) (2003) 335–343.

[14] J. Kim, V. Varadan, V. Varadan, X. Bao, Finite-element modeling of a smart cantilever plate and comparison with experiments, Smart Materials and Structures 5 (2) (1996) 165–170.

[15] K. Ou, K. Chen, T. Yang, S. Lee, A novel semianalytical approach for finding pull-in voltages of micro cantilever beams subjected to electrostatic loads and residual stress gradients, Journal of Microelectromechanical Systems 20 (2) (2011) 527–537.

[16] Y. Nemirovsky, O. Bochobza-Degani, A methodology and model for the pull-in parameters of electrostatic actuators, Journal of Microelectromechanical Systems 10 (4) (2001) 601–615.

[17] J. Seeger, B. Boser, Charge control of parallel-plate, electrostatic actuators and the tip-in instability, Journal of Microelectromechanical Systems 12 (5) (2003) 656–671.

[18] M. Raulli, K. Maute, Topology optimization of electrostatically actuated microsystems, Structural and Multidisciplinary Optimization 30 (5) (2005) 342–359.

[19] A. Alwan, G. Ananthasuresh, Coupled electrostatic-elastic analysis for topology optimization using material interpolation, International MEMS Conference 2006, Journal of Physics Conference Series 34 (1) (2006) 264–270.

[20] A. Alwan, G. Ananthasuresh, Topology optimization of electrostatically actuated micromechanical structures with accurate electrostatic modeling of the interpolated material model, Proceedings of the ASME International Design Engineering Technical Conferences and Computers and Information in Engineering Conferences-2006.

[21] G. Yoon, O. Sigmund, A monolithic approach for topology optimization of electrostatically actuated devices, Computer Methods in Applied Mechanics and Engineering 197 (45–48) (2008) 4062–4075.

[22] M. Bendsøe, Optimal shape design as a material distribution problem, Structural and Multidisciplinary Optimization 1 (4) (1989) 193–202.

[23] R. J. Yang, C. H. Chuang, Optimal topology design using linear programming, Computers & Structures 52 (2) (1994) 265–275.

[24] M. Bendsøe, O. Sigmund, Material interpolation schemes in topology optimization, Archive of Applied Mechanics 69 (9) (1999) 635–654.

[25] A. Diaz, O. Sigmund, Checkerboard patterns in layout optimization, Structural Optimization 10 (1) (1995) 40–45.

[26] R. Haber, C. Jog, M. P. Bendsøe, A new approach to variable-topology shape design using a constraint on perimeter, Structural Optimization 11 (1-2) (1996) 1–12.

[27] O. Sigmund, On the design of compliant mechanisms using topology optimization, Journal of Structural Mechanics 25 (4) (1997) 493–524.

[28] O. Sigmund, J. Petersson, Numerical instabilities in topology optimization: a survey on procedures dealing with checkerboards, mesh-dependencies and local minima, Structural Optimization 16 (1) (1998) 68–75.

[29] X. Qian, O. Sigmund, Topological design of electromechanical actuators with robustness toward over-and under-etching, Computer Methods in Applied Mechanics and Engineering 253 (2013) 237–251.

[30] J. Sethian, A. Wiegmann, Structural boundary design via level set and immersed interface methods, Journal of Computational Physics 163 (2) (2000) 489–528.

[31] M. Y. Wang, X. Wang, D. Guo, A level set method for structural topology optimization, Computer Methods in Applied Mechanics and Engineering 192 (1–2) (2003) 227–246.

[32] G. Allaire, F. Jouve, A. Toader, Structural optimization using sensitivity analysis and a level-set method, Journal of Computational Physics 194 (1) (2004) 363–393.

[33] T. Yamada, K. Izui, S. Nishiwaki, A. Takezawa, A topology optimization method based on the level set method incorporating a fictitious interface energy, Computer Methods in Applied Mechanics and Engineering 199 (45) (2010) 2876–2891.

[34] T. Yamada, K. Izui, S. Nishiwaki, A level set-based topology optimization method for maximizing thermal diffusivity in problems including design-dependent effects, Journal of Mechanical Design 133 (2011) 031011.

[35] C. Zhuang, Z. Xiong, H. Ding, A level set method for topology optimization of heat conduction problem under multiple load cases, Computer Methods in Applied Mechanics and Engineering 196 (4) (2007) 1074–1084.

[36] M.-G. Kim, S.-H. Ha, S. Cho, Level set-based topological shape optimization of nonlinear heat conduction problems using topological derivatives, Mechanics Based Design of Structures and Machines 37 (4) (2009) 550–582.

[37] A. Huerta, W. Liu, Viscous flow with large free surface motion, Computer Methods in Applied Mechanics and Engineering 69 (3) (1988) 277–324.

[38] C. Hirt, A. Amsden, J. Cook, An arbitrary Lagrangian–Eulerian computing method for all flow speeds, Journal of Computational Physics 135 (2) (1997) 203–216.

[39] T. Belytschko, T. Black, Elastic crack growth in finite elements with minimal remeshing, International Journal for Numerical Methods in Engineering 45 (5) (1999) 601–620.

[40] J. Dolbow, T. Belytschko, A finite element method for crack growth without remeshing, International Journal for Numerical Methods in Engineering 46 (1) (1999) 131–150.

[41] N. Sukumar, D. Chopp, N. Moës, T. Belytschko, Modeling holes and inclusions by level sets in the extended finite-element method, Computer Methods in Applied Mechanics and Engineering 190 (46) (2001) 6183–6200.

[42] S. Yamasaki, T. Nomura, A. Kawamoto, K. Sato, S. Nishiwaki, A level set-based topology optimization method targeting metallic waveguide design problems, International Journal for Numerical Methods in Engineering 87 (9) (2011) 844–868.

[43] D. Ma, N. Kikuchi, Topological design for vibrating structures, Computer Methods in Applied Mechanics and Engineering 121 (1995) 259–280.

[44] Z.-D. Ma, N. Kikuchi, I. Hagiwara, Structural topology and shape optimization for a frequency response problem, Computational Mechanics 13 (3) (1993) 157–174.

[45] S. Min, N. Kikuchi, Y. Park, S. Kim, S. Chang, Optimal topology design of structures under dynamic loads, Structural Optimization 17 (2-3) (1999) 208–218.

[46] B. E. Boser, R. T. Howe, Surface micromachined accelerometers, IEEE Journal of Solid-State Circuits 31 (3) (1996) 366–375.

[47] K. Jose, W. Suh, P. Xavier, V. Varadan, V. Varadan, Surface acoustic wave mems gyroscope, Wave Motion 36 (4) (2002) 367–381.

[48] C. Jog, Topology design of structures subjected to periodic loading, Journal of Sound and Vibration 253 (3) (2002) 687–709.

[49] S. Nishiwaki, K. Saitou, S. Min, N. Kikuchi, Topological design considering flexibility under periodic loads, Structural and Multidisciplinary Optimization 19 (1) (2000) 4–16.

[50] D. Tcherniak, Topology optimization of resonating structures using simp method, International Journal for Numerical Methods in Engineering 54 (11) (2002) 1605–1622.

[51] Y. Maeda, S. Nishiwaki, K. Izui, M. Yoshimura, K. Matsui, K. Terada, Structural topology optimization of vibrating structures with specified eigenfrequencies and eigenmode shapes, International Journal for Numerical Methods in Engineering 67 (5) (2006) 597–628.

[52] L. Shu, M. Y. Wang, Z. Fang, Z. Ma, P. Wei, Level set based structural topology optimization for minimizing frequency response, Journal of Sound and Vibration 330 (24) (2011) 5820–5834.

[53] T. Yamada, T. Matsumoto, S. Nishiwaki, Design of mechanical structures considering harmonic loads using level set-based topology optimization, Proceedings of the ASME 2012 International Design Engineering Technical Conferences and Computers and Information in Engineering Conference.

[54] T. Buhl, C. B. Pedersen, O. Sigmund, Stiffness design of geometrically nonlinear structures using topology optimization, Structural and Multidisciplinary Optimization 19 (2) (2000) 93–104.

[55] T. E. Bruns, D. A. Tortorelli, Topology optimization of non-linear elastic structures and compliant mechanisms, Computer Methods in Applied Mechanics and Engineering 190 (26) (2001) 3443–3459.

[56] H. C. Gea, J. Luo, Topology optimization of structures with geometrical nonlinearities, Computers & Structures 79 (20) (2001) 1977–1985.

[57] D. Jung, H. C. Gea, Topology optimization of nonlinear structures, Finite Elements in Analysis and Design 40 (11) (2004) 1417–1427.

[58] T. Bruns, O. Sigmund, D. A. Tortorelli, Numerical methods for the topology optimization of structures that exhibit snap-through, International Journal for Numerical Methods in Engineering 55 (10) (2002) 1215–1237.

[59] T. Bruns, O. Sigmund, Toward the topology design of mechanisms that exhibit snap-through behavior, Computer Methods in Applied Mechanics and Engineering 193 (36) (2004) 3973–4000.

[60] C. B. Pedersen, T. Buhl, O. Sigmund, Topology synthesis of large-displacement compliant mechanisms, International Journal for Numerical Methods in Engineering 50 (12) (2001) 2683–2705.

[61] T. Bruns, D. Tortorelli, An element removal and reintroduction strategy for the topology optimization of structures and compliant mechanisms, International Journal for Numerical Methods in Engineering 57 (10) (2003) 1413–1430.

[62] G. H. Yoon, Y. Y. Kim, Element connectivity parameterization for topology optimization of geometrically nonlinear structures, International Journal of Solids and Structures 42 (7) (2005) 1983–2009.

[63] G. H. Yoon, Y. S. Joung, Y. Y. Kim, Optimal layout design of three-dimensional geometrically non-linear structures using the element connectivity parameterization method, International Journal for Numerical Methods in Engineering 69 (6) (2007) 1278–1304.

[64] T. Belytschko, Y. Y. Lu, L. Gu, Element-free galerkin methods, International Journal for Numerical Methods in Engineering 37 (2) (1994) 229–256.

[65] W. K. Liu, S. Jun, Y. F. Zhang, Reproducing kernel particle methods, International Journal for Numerical Methods in Fluids 20 (8-9) (1995) 1081–1106.

[66] W. K. Liu, S. Jun, S. Li, J. Adee, T. Belytschko, Reproducing kernel particle methods for structural dynamics, International Journal for Numerical Methods in Engineering 38 (10) (1995) 1655–1679.

[67] J. J. Monaghan, An introduction to sph, Computer Physics Communications 48 (1) (1988) 89–96.

[68] S. Koshizuka, Y. Oka, Moving-particle semi-implicit method for fragmentation of incompressible fluid, Nuclear Science and Engineering 123 (3) (1996) 421–434.

[69] S. Cho, J. Kwak, Topology design optimization of geometrically non-linear structures using meshfree method, Computer methods in applied mechanics and engineering 195 (44) (2006) 5909–5925.

[70] J. Zhou, W. Zou, Meshless approximation combined with implicit topology description for optimization of continua, Structural and Multidisciplinary Optimization 36 (4) (2008) 347–353.

[71] R. A. Gingold, J. J. Monaghan, Smoothed particle hydrodynamics-theory and application to non-spherical stars, Monthly notices of the royal astronomical society 181 (1977) 375–389.

[72] S. J. Cummins, M. Rudman, An sph projection method, Journal of computational physics 152 (2) (1999) 584–607.

[73] S. Shao, E. Y. Lo, Incompressible sph method for simulating newtonian and non-newtonian flows with a free surface, Advances in Water Resources 26 (7) (2003) 787–800.

[74] S. Li, W. K. Liu, Meshfree particle methods, Vol. 11, Springer, 2004.

[75] Y. Chikazawa, S. Koshizuka, Y. Oka, A particle method for elastic and visco-plastic structures and fluid-structure interactions, Computational Mechanics 27 (2) (2001) 97–106.

[76] M. Song, S. Koshizuka, Y. Oka, A particle method for dynamic simulation of elastic solids, Proceedings of the 6th WCCM in Conjunction with APCOM.

[77] M. Manabe, T. Yamada, K. Izui, S. Nishiwaki, Topology optimization incorporating level set boundary expressions using a particle method, Transactions of the Japan Society of Mechanical Engineers, Series A 77 (784) (2011) 2054–2066.

[78] J. J. Monaghan, Smoothed particle hydrodynamics, Annual review of astronomy and astrophysics 30 (1992) 543–574.

[79] J. J. Monaghan, Simulating free surface flows with sph, Journal of computational physics 110 (2) (1994) 399–406.

[80] J. J. Monaghan, Sph without a tensile instability, Journal of Computational Physics 159 (2) (2000) 290–311.

[81] R. Vignjevic, J. Campbell, L. Libersky, A treatment of zero-energy modes in the smoothed particle hydrodynamics method, Computer methods in Applied mechanics and Engineering 184 (1) (2000) 67–85.

[82] M. Sussman, P. Smereka, S. Osher, A level set approach for computing solutions to incompressible two-phase flow, Journal of Computational physics 114 (1) (1994) 146–159.

[83] J. Sethian, Level set methods and fast marching methods: evolving interfaces in computational geometry, fluid mechanics, computer vision, and materials science, Vol. 3, Cambridge university press, 1999.

[84] S. Yamasaki, S. Nishiwaki, T. Yamada, K. Izui, M. Yoshimura, A structural optimization method based on the level set method using a new geometry-based re-initialization scheme, International Journal for Numerical Methods in Engineering 83 (12) (2010) 1580–1624.

[85] S. Osher, R. Fedkiw, Level Set Methods and Dynamic Implicit Surfaces, Springer-Verlag, 2003.

[86] W. R. Buell, B. A. Bush, Mesh generation - a survey, Journal of Engineering for Industry 95 (1) (1973) 332–338.

[87] D. A. Field, Laplacian smoothing and delaunay triangulations, Communications in Applied Numerical Methods 4 (6) (1988) 709–712.

[88] R. E. Bank, J. Xu, An algorithm for coarsening unstructured meshes, Numerische Mathematik 73 (1) (1996) 1–36.

[89] R. E. Bank, R. K. Smith, Mesh smoothing using a posteriori error estimates, SIAM Journal on Numerical Analysis 34 (3) (1997) 979–997.

[90] G. Allaire, Shape optimization by the homogenization method, Springer-Verlag, 2002.

[91] B. B. Guzina, M. Bonnet, Topological derivative for the inverse scattering of elastic waves, The Quarterly Journal of Mechanics and Applied Mathematics 57 (2) (2004) 161–179.

[92] M. Bonnet, B. B. Guzina, Sounding of finite solid bodies by way of topological derivative, International Journal for Numerical Methods in Engineering 61 (13) (2004) 2344–2373.

[93] T. Yamada, S. Yamasaki, S. Nishiwaki, K. Izui, M. Yoshimura, Design of compliant thermal actuators using structural optimization based on the level set method, Journal of Computing and Information Science in Engineering 11 (1).

[94] S. Nishiwaki, M. I. Frecker, S. Min, N. Kikuchi, Topology optimization of compliant mechanisms using the homogenization method, International Journal for Numerical Methods in Engineering 42 (3) (1998) 535–559.

[95] S. Nishiwaki, S. Min, J. Yoo, N. Kikuchi, Optimal structural design considering flexibility, Computer Methods in Applied Mechanics and Engineering 190 (34) (2001) 4457–4504.

[96] A. Saxena, Synthesis of compliant mechanisms for path generation using genetic algorithm, Journal of Mechanical Design 127 (2005) 745–752.

[97] A. Saxena, Topology design of large displacement compliant mechanisms with multiple materials and multiple output ports, Structural and Multidisciplinary Optimization 30 (6) (2005) 477–490.

[98] S. Wang, K. Tai, M. Y. Wang, An enhanced genetic algorithm for structural topology optimization, International Journal for Numerical Methods in Engineering 65 (1) (2006) 18–44.

[99] G. Allaire, F. De Gournay, F. Jouve, A. Toader, Structural optimization using topological and shape sensitivity via a level set method, Control and Cybernetics 34 (1) (2005) 59–80.

[100] J. Sokolowski, A. Zochowski, On the topological derivative in shape optimization, SIAM Journal on Control and Optimization 37 (4) (1999) 1251–1272.

[101] M. Burger, B. Hackl, W. Ring, Incorporating topological derivatives into level set methods, Journal of Computational Physics 194 (1) (2004) 344–362.

[102] L. He, C.-Y. Kao, S. Osher, Incorporating topological derivatives into shape derivatives based level set methods, Journal of Computational Physics 225 (1) (2007) 891–909.

List of Publications

International Journal Papers

[1] Takayo Kotani, Takayuki Yamada, Shintaro Yamasaki, Makoto Ohkado, Kazuhiro Izui and Nishiwaki Shinji, Driving force profile design in comb drive electrostatic actuators using a level set-based shape optimization method, *Structural and Multidisciplinary Optimization, accepted.*

Domestic Journal Papers (in Japanese)

[1] 小谷高代，山　慎太郎，山田崇恭，大門真，泉井一浩，西脇眞二, レベルセット法に基づく静電アクチュエータの構造最適化, 日本機械学会論文集（C 編），79 巻 805 号 (2013)，pp.3234-3247.

[2] 小谷高代，山田崇恭，泉井一浩，西脇眞二, レベルセット法に基づくトポロジー最適化を用いた機械式レゾネーターの最適設計法, 計算数理工学論文集，13 巻 (2013), pp.115-120.

Refereed International Proceedings

[1] Takayo Kotani, Takayuki Yamada, Kazuhiro Izui, and Shinji Nishiwaki, Optimum design of compliant actuators using level set-based topology optimization method, *Proceedings of 6th China-Japan-Korea Joint Symposium on Optimization of Structural and Mechanical Systems (CJK-OSM6)* June 22-25, 2010, Kyoto, Japan, J-93.

[2] Takayo Kotani, Takayuki Yamada, Masatoshi Manabe, Kazuhiro Izui, and Shinji Nishi-

waki, Level set-based topology optimization of large displacement compliant mechanisms, *Proceedings of 9th World Congress on Structural and Multidisciplinary Optimization (WCSMO-9)* June 13-17, 2011, Shizuoka, Japan, No.038.

Non refereed International Proceedings

[1] Takayo Kotani，Takayuki Yamada, Masatoshi Manabe, Kazuhiro Izui, and Shinji Nishiwaki, Level set-based topology optimization of compliant mechanisms considering large displacement effects, *11th US National Congress on Computational Mechanics (USNCCM11)*, July 25-28, 2011, Minneapolis, Minnesota, USA, CD-ROM.

Domestic Conferences (in Japanese)

[1] 小谷高代，真鍋匡利，山田崇恭，泉井一浩，西脇眞二，レベルセット法に基づくトポロジー最適化と粒子法の組み合わせによるコンプライアントメカニズムの構造最適化，第17回計算工学講演会，日本計算工学会，2012年5月29日- 31日，京都，pp.395-396.

[2] 小谷高代，山田崇恭，泉井一浩，西脇眞二，レベルセット法に基づくトポロジー最適化を用いた機械式レゾネーターの最適設計法，計算数理工学シンポジウム2013，日本計算数理工学会，2013年11月29日- 30日，北海道，No.24-11129.